Monthly Notices
of the
ROYAL ASTRONOMICAL SOCIETY

MNRAS **481,** 59–97 (2018)
Advance Access publication 2018 August 6

doi:10.1093/mnras/sty2082

Far-infrared *Herschel* SPIRE spectroscopy of lensed starbursts reveals physical conditions of ionized gas

Zhi-Yu Zhang,[1,2]★ R. J. Ivison,[2,1]★ R. D. George,[1] Yinghe Zhao,[3,4,5] L. Dunne,[1,6] R. Herrera-Camus,[7] A. J. R. Lewis,[1] Daizhong Liu,[8,9] D. Naylor,[10] Iván Oteo,[1,2] D. A. Riechers,[11] Ian Smail,[12] Chentao Yang,[13,9,14] Stephen Eales,[6] Ros Hopwood,[15] Steve Maddox,[1,6] Alain Omont[14] and Paul van der Werf[16]

[1]*Institute for Astronomy, University of Edinburgh, Blackford Hill, Edinburgh EH9 3HJ, UK*
[2]*European Southern Observatory, Karl-Schwarzschild-Strasse 2, D-85748 Garching, Germany*
[3]*Yunnan Observatories, Chinese Academy of Sciences, Kunming 650011, P.R. China*
[4]*Key Laboratory for the Structure and Evolution of Celestial Objects, Chinese Academy of Sciences, Kunming 650011, P.R. China*
[5]*Centre for Astronomical Mega-Science, CAS, 20A Datun Road, Chaoyang District, Beijing 100012, P.R. China*
[6]*School of Physics and Astronomy, Cardiff University, The Parade, Cardiff CF24 3AA, UK*
[7]*Max-Planck-Institut für Extraterrestrische Physik (MPE), Giessenbachstr, D-85748 Garching, Germany*
[8]*MPIA, Koenigstuhl 17, D-69117 Heidelberg, Germany*
[9]*Purple Mountain Observatory, 2 West Beijing Road, Nanjing 230000, P.R. China*
[10]*Department of Physics, University of Lethbridge, Lethbridge, Alberta T1K 3M4, Canada*
[11]*Department of Astronomy, Cornell University, Space Sciences Building, Ithaca, NY 14853, USA*
[12]*Department of Physics, Centre for Extragalactic Astronomy, Durham University, South Road, Durham DH1 3LE, UK*
[13]*European Southern Observatory, Alonso de Córdova 3107, Casilla 19001, Vitacura, Santiago, Chile*
[14]*Institut d'Astrophysique de Paris, Sorbonne Université, CNRS,UMR 7095, 98 bis bd Arago, F-75014 Paris, France*
[15]*Department of Physics, Imperial College London, Prince Consort Road, London SW7 2AZ, UK*
[16]*Sterrewacht Leiden, Leiden University, PO Box 9513, NL-2300 RA Leiden, the Netherlands*

Accepted 2018 July 18. Received 2018 July 18; in original form 2017 August 2

ABSTRACT

The most intensively star-forming galaxies are extremely luminous at far-infrared (FIR) wavelengths, highly obscured at optical and ultraviolet wavelengths, and lie at $z \geq 1$–3. We present a programme of FIR spectroscopic observations with the SPIRE FTS, as well as photometric observations with PACS, both on board *Herschel*, towards a sample of 45 gravitationally lensed, dusty starbursts across $z \sim 1$–3.6. In total, we detected 27 individual lines down to $3\,\sigma$, including nine [C II] 158 μm lines with confirmed spectroscopic redshifts, five possible [C II] lines consistent with their FIR photometric redshifts, and in some individual sources a few [O III] 88 μm, [O III] 52 μm, [O I] 145 μm, [O I] 63 μm, [N II] 122 μm and OH 119 μm (in absorption) lines. To derive the typical physical properties of the gas in the sample, we stack all spectra weighted by their intrinsic luminosity and by their 500μm flux densities, with the spectra scaled to a common redshift. In the stacked spectra, we detect emission lines of [CII] 158 μm, [N II] 122 μm, [O III] 88 μm, [O III] 52 μm, [O I] 63 μm and the absorption doublet of OH at 119 μm, at high fidelity. We find that the average electron densities traced by the [N II] and [O III] lines are higher than the average values in local star-forming galaxies and ULIRGs, using the same tracers. From the [N II]/[C II] and [O I]/[C II] ratios, we find that the [C II] emission is likely dominated by the photodominated regions (PDR), instead of by ionized gas or large-scale shocks.

Key words: galaxies: active – galaxies: high-redshift – galaxies: starburst – infrared: galaxies – submillimetre: galaxies.

1 INTRODUCTION

The mean star formation rate (SFR) density in the Universe was much higher in the past, peaking around 10 billion years ago, at

★ E-mail: pmozhang@gmail.com (ZYZ); Rob.Ivison@eso.org (RJI)

$z \approx 2$ (e.g. Hopkins & Beacom 2006; Madau & Dickinson 2014), at which time the SFR per unit co-moving volume peaked at levels 10–30× higher than the current rate. Most of the stars created at this time were located within low-mass ($M_* < 10^{10.5}\,M_\odot$) galaxies with moderate SFRs (SFR$\leq 100\,M_\odot\,yr^{-1}$) (e.g. Daddi et al. 2007; Hopkins et al. 2010; Sparre et al. 2015).

Surveys at far-infrared (FIR) and sub-millimetre (submm) wavelengths revealed a population of so-called submm galaxies or dusty star-forming galaxies (SMGs or DSFGs, e.g. Smail, Ivison & Blain 1997; Eales et al. 2010), mostly at $z = 1$–3 (e.g. Chapman et al. 2005; Simpson et al. 2014; Danielson et al. 2017), but with a smattering at $z > 4$ (e.g. Asboth et al. 2016; Ivison et al. 2016), which can account for much of the submm background. These galaxies were forming stars at tremendous rates, $\geq 300\,M_\odot\,yr^{-1}$ (e.g. Blain et al. 2002) – intense star formation events that are thought to have been powered primarily by major mergers (e.g. Ivison et al. 2007; Engel et al. 2010; Ivison et al. 2011; Oteo et al. 2016), although some fractions are likely isolated, fragmenting gas discs (e.g. Hodge et al. 2012). The subsequent rapid period of physical evolution likely passes through a quasar stage into a compact passive galaxy, which grows via dry minor mergers into a massive elliptical galaxies at the present day (e.g. Côté et al. 2007; Naab, Johansson & Ostriker 2009).

Determining the physical conditions of the ionized gas, powered directly by star formation, is one of the most important objectives that remain in our study of DSFGs. The interstellar medium (ISM) is central to many galaxy-wide physical processes, and is therefore critical to our understanding of the gas-star-black hole interplay and evolution of galaxies (e.g. Kormendy & Ho 2013). However, the large quantities of dust within these starbursts obscure the most common ISM tracers: rest-frame optical spectral lines from the recombination of hydrogen, and those from the most abundant metal species, C, N, O.

Atomic fine-structure forbidden transitions in the FIR, such as [C II] 158 μm, [N II] 122 μm, [O I] 63 μm, and [O III] 88 μm are important coolants of the ISM, providing critical diagnostics of physical conditions across all redshifts (e.g. Stacey et al. 1991; Lord et al. 1996; Herrera-Camus et al. 2016; Zhao et al. 2016a; Wardlow et al. 2017; Herrera-Camus et al. 2018a,b). Among these lines, [C II] 158 μm is probably the most important, and the best studied, since it is the brightest FIR line in most galaxies and often accounts for 0.1–1 per cent of the total FIR luminosity (e.g. Stacey et al. 1991; Díaz-Santos et al. 2013). However, neutral carbon (C) has an ionization energy of 11.3 eV, meaning that it co-exists in both photodissociation regions (PDRs) and HII regions (e.g. Stacey et al. 2010). [C II] can be excited by three independent collisions excitation mechanisms, electrons, neutral hydrogen (H I), and molecular hydrogen (H_2). These mechanisms make the [C II] emission arising from nearly all ISM phases difficult to discriminate from each other.

The [N II] 205μm transition provides complementary information on the origin of the [CII] 158 μm emission (e.g. Oberst et al. 2006; Walter et al. 2009b; Stacey et al. 2010; Decarli et al. 2014; Pavesi et al. 2016). The line ratio of [C II] 158 μm/[N II] 205μm only depends on the abundances of N^+ and C^+ in the H II region, and the relative contributions of the neutral and ionized ISM phases, making the observed [CII]/[N II] line ratio an excellent probe of the fraction of [C II] from the ionized gas phase (e.g. Oberst et al. 2011, 2006).

Unfortunately these lines are typically unobservable from the ground at low redshifts due to poor atmospheric transmission. The Spectral and Photometric Imaging REceiver (SPIRE) (Griffin et al. 2010) instrument aboard the *Herschel Space Observatory* (Pilbratt et al. 2010) incorporated a Fourier Transform Spectrometer (FTS), covering many of the brightest FIR lines. However, with its 3.5 m aperture, the few × 10 mJy flux densities exhibited by [CII] 158 μm in typical high-redshift DSFGs were well below the capabilities of *Herschel*'s SPIRE FTS, requiring prohibitively long integration times.

An alternative solution, exploited since the earliest SCUBA observations (Smail et al. 1997), is to use the flux boost provided by gravitational lensing due to foreground galaxies, or clusters of galaxies. Most occurrences grant a factor of a few increase in brightness, but the most strongly lensed systems enable very detailed study of the background object (e.g. Fu et al. 2012; Bussmann et al. 2012, 2013; Messias et al. 2014; Dye et al. 2015; Spilker et al. 2016), as epitomized by SMM J2135−0102 – the Cosmic Eyelash – serendipitously discovered in the neighbourhood of a massive cluster, and possessing a high average amplification (37.5 ± 4.5, Swinbank et al. 2010, 2011). Such strongly lensed DSFGs are rare ($\sim 0.26\,deg^{-2}$; Bussmann et al. 2013), necessitating surveys covering large areas in order to assemble a statistically significant sample. This population can be selected efficiently at FIR/submm wavelengths, where the number density of unlensed sources at high flux densities drops quickly (after removal of local spiral galaxies, and blazars), with $S_{500\,\mu m} > 100$ mJy sources being strongly lensed DSFGs (Negrello et al. 2010; Wardlow et al. 2013), with just a smattering of hyperluminous IR galaxies (e.g. Ivison et al. 2013; Fu et al. 2013). Such FIR surveys have recently been undertaken (e.g. Eales et al. 2010; Vieira et al. 2010; Oliver et al. 2012), using the *Herschel Space Observatory* and the South Pole Telescope (SPT; Carlstrom et al. 2011), which has resulted in hundreds to thousands of strongly lensed DSFGs candidates (e.g. González-Nuevo et al. 2012; Mocanu et al. 2013; Negrello et al. 2017). Many of them have been confirmed as such by follow-up observations (e.g. Negrello et al. 2014; Spilker et al. 2016).

In this paper, we present the results of two *Herschel* Open Time programmes, both comprising FIR spectroscopic and photometric observations of a total of 45 gravitationally lensed DSFGs using the SPIRE FTS and PACS aboard *Herschel*. This paper is organized as follows: Section 2 provides an overview of the sample selection and the overall properties of the data; Section 3 details the observations and data reduction for *Herschel* SPIRE FTS spectroscopy and PACS photometry; Section 4 presents the observed spectra and fitted dust spectral energy distributions (SEDs); Section 6 presents the stacked spectra and associated analysis. We discuss caveats in statistical biases, stacking methods, absorption contaminations, and abundances in Section 8. We summarize our results and draw conclusions in Section 9. Throughout, we adopt a standard Λ-CDM cosmology with $\Omega_m = 0.3$, $\Omega_\Lambda = 0.7$, and $H_0 = 70\,km\,s^{-1}\,Mpc^{-1}$.

2 SAMPLE

In Table 1, we present basic information for our sample of 45 DSFGs, observed in OT1_RIVISON_1 and OT2_RIVISON_1. The majority of the targets were selected from the *Herschel* Astrophysical Terahertz Large Area Survey (*H*-ATLAS; Eales et al. 2010) and *Herschel* Multi-Tiered Extragalactic Survey (*Her*MES; Oliver et al. 2012) Large Mode Survey (HeLMS). *Herschel* SPIRE 250, 350, and 500μm images were used to identify strongly lensed DSFG candidates, from which we selected those satisfying $S_{350} \gtrsim 200$ mJy, with no indication that they could be a blazar or a $z \lesssim 0.1$ spiral, and with a colour cut attempting to remove the highest redshift objects such that the [C II] 158 μm line would remain within the FTS spectral range. The SPIRE images show point sources, or only

Table 1. Summary of the Galaxy sample.

IAU name	Short name	RA	Dec.	Redshift	Notes
HATLAS J090740.0−004200	SDP.9	09h07m40.032s	−00d41m59.64s	1.577	
HATLAS J091043.0−000322	SDP.11	09h10m43.056s	−00d03m22.68s	1.784	
HATLAS J090302.9−014127	SDP.17	09h03m03.024s	−01d41m27.24s	2.3050	
HATLAS J090311.6+003906	SDP.81	09h03m09.408s	+00d39m06.48s	3.0425	
HATLAS J091305.0−005343	SDP.130	09h13m05.112s	−00d53m43.44s	2.6256	
HATLAS J085358.9+015537	G09-v1.40	08h53m58.872s	+01d55m37.56s	2.0923	
HATLAS J083051.0+013224	G09-v1.97	08h30m51.168s	+01d32m24.36s	3.634	
HATLAS J084933.4+021443	G09-v1.124	08h49m33.336s	+02d14m44.52s	2.4101	
HATLAS J091840.8+023047	G09-v1.326	09h18m40.92s	+02d30m46.08s	2.5812	
HATLAS J114638.0−001132	G12-v2.30	11h46m37.992s	−00d11m31.92s	3.2588	
HATLAS J113526.3−014606	G12-v2.43	11h35m26.28s	−01d46m06.6s	3.1275	
HATLAS J115820.1−013753	G12-v2.257	11h58m20.04s	−01d37m51.6s	2.1909	
HATLAS J142935.3−002836	G15-v2.19	14h29m35.232s	−00d28m36.12s	1.026	
HATLAS J141351.9−000026	G15-v2.235	14h13m52.08s	−00d00m24.48s	2.4778	
HATLAS J134429.4+303036	NA.v1.56	13h44m29.52s	+30d30m34.2s	2.3010	
HATLAS J133649.9 + 291801	NA.v1.144	13h36m49.992s	+29d17m59.64s	2.2024	
HATLAS J132859.3+292317	NA.v1.177	13h28m59.256s	+29d23m26.16s	2.778	
HATLAS J132504.4+311537	NA.v1.186	13h25m04.512s	+31d15m36s	1.8358	
HATLAS J132427.0+284452	NB.v1.43	13h24m27.216s	+28d44m49.2s	1.676	
HATLAS J133008.4+245900	NB.v1.78	13h30m08.52s	+24d58m59.16s	3.1112	
HATLAS J125632.7+233625	NC.v1.143	12h56m32.544s	+23d36m27.72s	3.565	
HATLAS J223829.0−304148	*SA.v1.44*	22h38m29.472s	−30d41m49.2s	1.33 ± 0.11^a	
HATLAS J222536.3−295646	*SA.v1.53*	22h25m36.48s	−29d56m49.56s	1.64 ± 0.16^a	
HATLAS J232531.4−302234	*SB.v1.143*	23h25m31.608s	−30d22m35.76s	2.67 ± 0.13^a	
HATLAS J232623.0−342640	*SB.v1.202*	23h26m23.064s	−34d26m43.8s	2.17 ± 0.11^a	
HATLAS J232419.8−323924	*SC.v1.128*	23h24m19.944s	−32d39m28.08s	2.51 ± 0.15^a	
HATLAS J000912.6−300809	*SD.v1.70*	00h09m12.864s	−30d08m09.24s	1.19 ± 0.10^a	
HATLAS J000722.3−352014	*SD.v1.133*	00h07m22.272s	−35d20m15s	1.38 ± 0.11^a	
HATLAS J002625.1−341737	*SD.v1.328*	00h26m25.176s	−34d17m38.4s	2.70 ± 0.16^a	
HATLAS J004736.0−272953	*SE.v1.165*	00h47m36.072s	−27d29m53.16s	2.03 ± 0.15^a	
HATLAS J010250.7−311721	*SF.v1.88*	01h02m50.88s	−31d17m23.64s	1.57 ± 0.13^a	
HATLAS J012407.3−281435	*SF.v1.100*	01h24m07.536s	−28d14m35.16s	2.00 ± 0.13^a	
HATLAS J014834.7−303532	*SG.v1.77*	01h48m34.704s	−30d35m32.64s	1.53 ± 0.13^a	
HERMES J004714.1+032453	HeLMS08	00h47m14.136s	+03d24m55.44s	1.19^b	No FTS spectra
HERMES J001626.0+042613	HeLMS22	00h16m26.064s	+04d26m12.48s	2.5093^b	No FTS spectra
HERMES J005159.4+062240	HeLMS18	00h51m59.448s	+06d22m41.52s	2.392^b	No FTS spectra
HERMES J233255.5−031134	HeLMS2	23h32m55.584s	−03d11m36.24s	2.6899^b	
HERMES J234051.3−041937	HeLMS7	23h24m39.576s	−04d39m34.2s	2.473^b	
HERMES J004723.3+015749	HeLMS9	00h47m23.352s	+01d57m50.76s	1.441^b	No FTS spectra
HERMES J001615.8+032433	HeLMS13	00h16m15.864s	+03d24m36.72s	2.765^b	No FTS spectra
HERMES J233255.7−053424	HeLMS15	23h32m55.824s	−05d34m26.76s	2.4024^b	No FTS spectra
HERMES J234051.3−041937	HeLMS5	23h40m51.528s	−04d19m40.8s	3.50^b	No FTS spectra
1HerMES S250 J142823.9+352619	HBoötes03	14h28m24.072s	+35d26m19.32s	1.325	
1HerMES S250 J021830.5−053124	HXMM02	02h18m30.672s	−05d31m31.44s	3.39	
SMM J213511.6−010252	Eyelash	21h35m11.64s	−01d02m52.44s	2.32591	

[a]Redshift estimated from photometric data, using the SED of average ALESS galaxies as the template (Ivison et al. 2016). For galaxy without spec-z information we label their names with italic fonts. The order of the table is organized by different survey fields and then by the right ascensions of the galaxies.
[b]Spectroscopic redshifts adopted from Nayyeri et al. (2016).

show marginally resolved features. The sample was supplemented with several objects for which substantial ancillary data existed, including SMM J2135−0102. About half of the sources have been confirmed to be lensed targets from submm continuum observations (e.g. Bussmann et al. 2013).

3 OBSERVATIONS AND DATA REDUCTION

3.1 PACS observations and flux density measurements

The original *H*-ATLAS parallel PACS imaging data at 100 and 160 μm have noise levels of ∼25–50 mJy (almost 10 times higher than our new targeted observations; see Ibar et al. 2010a; Eales et al. 2010). They were insufficiently deep to detect many of our sample, and the targets outside *H*-ATLAS had no coverage at these wavelengths. To complement the SPIRE photometric measurements across the flux density peak of their SEDs and to provide stronger constraints on their rest-frame mid-infrared (MIR) emission, we obtained deep imaging observations at 100 and 160 μm with *Herschel* PACS.

For each galaxy we obtained two cross-linked mini-scans with PACS, recording data at 100 and 160 μm simultaneously. Each mini-scan covers an area of ∼10 arcmin × 3 arcmin, with two orientations of 70° and 110°, resulted to 3 min on-source and a total of 791 s observing time including overhead. On average, we reach 1σ depths of ∼3 and 7 mJy at 100 and 160μm, respectively. Archival mini-

scan imaging data covering SMM J2135−0102 was combined with our two scans to produce a deeper image, which is particularly useful as this field has a large number of FIR sources visible in the region around the target lensed galaxy. Information about the *Herschel* PACS observations is listed in Table A1 in Appendix A.

We adopted the *Herschel* Interactive Processing Environment (HIPE v12; Ott 2010) to process and combine the mini-scan data using the standard pipeline scripts. To remove the 1/*f* noise, a high-pass filter was applied, after masking visible sources (e.g. Popesso et al. 2012). Corrections were adopted to the measured flux densities to compensate for the losses due to this filter. We also applied a colour correction to take into account the spectral index within the bandpass of the PACS spectrometer.[1]

To measure the flux density, we first removed all visible background sources, masking with 8–10 arcsec diameter circles, then fitted the global background and subtracted it from the masked image. The global background level was of the order of 10^{-6} Jy pixel^{-1}, making a negligible contribution to the final flux density measurements. We performed aperture photometry to remove the local background. Most targets displayed compact 100 μm emission within an aperture 5–7 arcsec in radius. Therefore, we adopted aperture corrections according to the encircled energy fraction (EEF) curves in the *Herschel* PACS manual,[2] assuming point-like sources. A few targets displayed extended 100 μm emission that was clearly resolved by the PACS beam. For these sources, we used an aperture of ∼25–30 arcsec (FWHM) to ensure all the emission was included. Around a third of the targets were resolved by PACS into two components in our 100 and 160μm maps, with separations ranging from 5 to 15 arcsec, too close to be resolved by SPIRE. For these, we first identify the peak of individual emitting structure by fitting 2D Gaussian distribution and performed aperture photometry on the two components separately and summed their flux densities within the SPIRE beam size. Among the sample, around half have been confirmed as lensed galaxies in previous studies (e.g. Bussmann et al. 2013, 2015). A few targets had components which displayed different S_{100}/S_{160} or S_{70}/S_{100} colours, perhaps indicative that they are not two segments from the same background lensed galaxy, but rather different galaxies along the line of sight. In Appendix B, we show postage-stamp images of the PACS observations of all of our targets.

The calibration uncertainties for the 100 and 160μm images were ∼3 per cent and ∼4 per cent,[3] respectively. We tested different high-pass filters, photometric aperture radii and mask radii, finding that these choices in total contribute uncertainties of $\lesssim$10 per cent. In the end, we combine all these into our final estimate of the flux uncertainty. Typical noise levels are ∼0.1 and ∼0.15 mJy pix^{-1} for the 100 and 160μm images, which are around 20–30times deeper than the PACS maps of the *H*-ATLAS survey (Ibar et al. 2010b; Smith et al. 2017a). For the common sources in Wardlow et al. (2017), we have re-measured fluxes at 100 and 160μm, and found consistent results differing by <5 per cent. Measured flux densities are shown in Table 2, along with their SPIRE 250, 350, and 500μm and Submillimeter Array (SMA) 880 μm flux density measurements, taken from Bussmann et al. (2013).

[1] http://herschel.esac.esa.int/twiki/bin/view/Public/PacsCalibrationWeb
[2] http://herschel.esac.esa.int/twiki/bin/view/Public/PacsCalibrationWeb
[3] According to the PACS Photometer – Point-Source Flux Calibration document 2011. http://herschel.esac.esa.int/twiki/pub/Public/PacsCalibrationWeb/pacs_bolo_fluxcal_report_v1.pdf

3.2 SPIRE FTS observations and data reduction

The SPIRE FTS instrument (i.e. Griffin et al. 2010) is comprised of two bolometer arrays (SSW and SLW), covering the wavelength ranges λ_{obs} = 191–318 and 295–671 μm, which corresponds to [C II] redshift ranges of 0.2–1.0 and 0.85–3.2, respectively. The observations were performed in the high-resolution mode, in which each mirror scan takes 66.6 s, producing a maximum optical path difference of 12.56 cm, resulting a uniform spectral resolution of ∼1.2 GHz. Observing dates and integration time are listed in Table A1 of Appendix A.

The profile of the SPIRE FTS beam varies with observing frequency in a complex manner (Makiwa et al. 2013). The effective angular resolution varies from ∼17 arcsec at the highest SSW frequency to a maximum of ∼42 arcsec at the lowest SLW frequency (Swinyard et al. 2010; Makiwa et al. 2013). The pointing accuracy was within 2 arcsec (Pilbratt et al. 2010). Our target sizes are mostly less than 2–3 arcsec, as revealed by high-resolution submm and radio imaging (e.g. Bussmann et al. 2013), except for G09.124 which consists of multiple galaxies at z = 2.4 with separations of up to 10.5 arcsec (e.g. Ivison et al. 2013).

We obtained spectra of 38 sources, including five repeat observations of SMM J2135−0102 (see George et al. 2014). Each observation consisted of 100 repetitions (100 forward and 100 reverse scans of the SMEC mirror), corresponding to 13320 s of on-source integration time. The SLW detectors are separated by 51 arcsec, and the SSW detectors by 33 arcsec, sufficiently far to avoid sidelobe contamination by emission from the targets. The central detectors of the arrays were centred on the target in each case.

We reprocessed the data from each observing epoch using the *Herschel* data processing pipeline (Fulton et al. 2010) within HIPE (Ott 2010) v14.2. The version of the calibration data is SPIRE_CAL_14_3. Due to the weakness of the emission from the sample, in most galaxies we could not obtain a good detection of the continuum level using the pipeline (e.g. Hopwood et al. 2014, 2015; Fulton et al. 2016), so their SLW and SSW spectra could not be matched to each other. This likely generates systematic continuum offsets as a function of frequency (e.g. Hopwood et al. 2015), which adds uncertainties to the spectra. The continuum levels detected with SPIRE/FTS have a good agreement with the SPIRE photometry, in general (Makiwa et al. 2016; Valtchanov et al. 2018). For rare cases ($\lesssim$ 30 per cent) where the baselines between SLW and SSW match each other, the continuum levels estimated from the FTS spectra at ∼250 μm are consistent with those measured from SPIRE photometric fluxes within ∼30 per cent.

For SLW and SSW, especially at the high-frequency end of the SLW spectra, about half of the spectra show a high level of fringing at the band edges (at the levels of ≥0.5 Jy), in particular at the high-frequency end of SLW spectra. Lower amplitude fringing is observed in all spectra. The fringing can be traced to resonant cavities that exist within the spectrometer (e.g. the air-gaps between the different band defining filters and/or field lenses) and their effect on continuum calibration. The imperfect subtraction of the warm background generated by the *Herschel* telescope has its root in the derived relative spectral response function (RSRF, e.g. *Herschel* workshop[4] 2014, Fulton et al. 2014; Swinyard et al. 2014). These fringes represent correlated pink (1/*f*) noise, which is the dominant noise contribution to our spectra and to the overall shape of the continuum. Moreover, the ripples not only vary with time, which

[4] https://nhscsci.ipac.caltech.edu/sc/index.php/Workshops/Fall2014Talks

Table 2. FIR continuum flux densities of the sample. 250, 350, and 500 μm data from *H*-ATLAS and *Her*MES, uncertainties include a 7 per cent calibration uncertainty (Swinyard et al. 2010; Bendo et al. 2013). Most of the 70 μm fluxes are from Wardlow et al. (2017), except for SDP.81 and SDP.130, which are measured with our PACS observations. 100 and 160 μm uncertainties include 2.75 per cent and 4.15 per cent calibration uncertainties respectively, following the PACS Photometer – Point-Source Flux Calibration document. The 850 μm data are from the SCUBA2 observations (Bakx et al. 2018). The 880 μm data is from Bussmann et al. (2013) and Swinyard et al. (2010). We notice that the SCUBA2 850 μm fluxes are higher than the SMA 880 μm fluxes, likely due to the interferometric filtering issue. Where not otherwise noted, amplification values are taken from Bussmann et al. (2013). We also notice that for HXMM02, the new ALMA flux density is 63.33 ± 0.58 (i.e. Bussmann et al. 2015), consistent with the SMA value.

Source	z	Amplification	$S_{70\,\mu m}$ (mJy)	$S_{100\,\mu m}$ (mJy)	$S_{160\,\mu m}$ (mJy)	$S_{250\,\mu m}$ (mJy)	$S_{350\,\mu m}$ (mJy)	$S_{500\,\mu m}$ (mJy)	$S_{850\,\mu m}$ (mJy)	$S_{880\,\mu m}$ (mJy)
SDP.9	1.574	8.8 ± 2.2	–	307 ± 15	546 ± 20	478 ± 34	328 ± 24	171 ± 14	–	24.8 ± 3.3
SDP.11	1.786	10.9 ± 1.3	–	161 ± 10	363 ± 20	421 ± 30	371 ± 26	221 ± 17	52 ± 1	30.6 ± 2.4
SDP.17	2.305	4.9 ± 0.7	–	66 ± 7	244 ± 19	354 ± 25	339 ± 24	220 ± 17	–	54.7 ± 3.1
SDP.81	3.040	15.9 ± 0.7[a]	< 9	–	58 ± 10	133 ± 11	186 ± 14	165 ± 14	108 ± 10	78.4 ± 8.2
SDP.130	2.6256	2.1 ± 0.3	< 9	–	66 ± 10	118 ± 9	137 ± 11	104 ± 9	67 ± 9	36.7 ± 3.9
G09-v1.40	2.093	15.3 ± 3.5	–	70 ± 4	280 ± 13	396 ± 28	368 ± 26	228 ± 17	–	61.4 ± 2.9
G09-v1.97	3.634	6.9 ± 0.6	–	53 ± 3	198 ± 10	249 ± 18	305 ± 22	269 ± 20	121 ± 8	85.5 ± 4.0
G09-v1.124	2.410	1.1 ± 0.1	16 ± 4	57 ± 4	169 ± 15	217 ± 16	249 ± 18	209 ± 16	62 ± 10	50.0 ± 3.5
G09-v1.326	2.5812	5.0 ± 1.0[b]	–	41 ± 4	106 ± 10	126 ± 10	151 ± 12	128 ± 11	61 ± 9	18.8 ± 1.6
G12-v2.30	3.259	9.5 ± 0.6	30 ± 4	62 ± 4	235 ± 15	317 ± 23	358 ± 25	291 ± 21	142 ± 8	86.0 ± 4.9
G12-v2.43	3.127	17.0 ± 11.0[b]	16 ± 3	81 ± 5	196 ± 11	279 ± 20	284 ± 21	205 ± 16	116 ± 9	48.6 ± 2.3
G12-v2.257	2.191	13.0 ± 7.0[b]	15 ± 4	43 ± 5	143 ± 11	119 ± 9	124 ± 10	101 ± 9	40 ± 9	–
G15-v2.19	1.027	9.7 ± 0.7[c]	316 ± 16	850 ± 10	1190 ± 53	802 ± 56	438 ± 31	200 ± 15	–	–
G15-v2.235	2.479	1.8 ± 0.3	–	48 ± 5	87 ± 6	189 ± 14	217 ± 16	176 ± 14	104 ± 11	33.3 ± 2.6
NA.v1.56	2.301	11.7 ± 0.9	14 ± 3	86 ± 4	308 ± 19	462 ± 33	466 ± 33	343 ± 25	142 ± 8	73.1 ± 2.4
NA.v1.144	2.202	4.4 ± 0.8	11 ± 3	47 ± 4	193 ± 10	294 ± 21	286 ± 21	194 ± 15	–	36.8 ± 2.9
NA.v1.177	2.778	–	–	40 ± 3	155 ± 14	268 ± 19	296 ± 21	249 ± 18	149 ± 11	50.1 ± 2.1
NA.v1.186	1.839	–	–	60 ± 6	163 ± 9	241 ± 18	227 ± 17	165 ± 13	39 ± 8	–
NB.v1.43	1.680	2.8 ± 0.4	–	52 ± 4	170 ± 24	342 ± 25	371 ± 27	251 ± 19	71 ± 10	30.2 ± 2.2
NB.v1.78	3.111	13.0 ± 1.5	40 ± 3	87 ± 4	212 ± 16	271 ± 20	278 ± 20	203 ± 16	108 ± 11	59.2 ± 4.3
NC.v1.143	3.565	11.3 ± 1.7	–	25 ± 3	97 ± 8	209 ± 16	289 ± 21	264 ± 20	160 ± 10	97.2 ± 6.5
SA.v1.44	1.33 ± 0.11[d]	–	–	93 ± 5	225 ± 14	252 ± 18	207 ± 15	100 ± 9	–	–
SA.v1.53	1.654[e]	–	–	57 ± 3	163 ± 23	194 ± 16	200 ± 17	119 ± 14	–	–
SB.v1.143	2.42[e]	–	–	35 ± 5	102 ± 15	176 ± 13	227 ± 17	176 ± 14	100 ± 9	–
SB.v1.202	2.055[e]	–	–	42 ± 4	130 ± 17	154 ± 12	178 ± 13	123 ± 11	57 ± 11	–
SC.v1.128	2.574[e]	–	–	35 ± 5	123 ± 13	213 ± 16	244 ± 18	169 ± 13	73 ± 10	–
SD.v1.70	1.19 ± 0.10[d]	–	–	156 ± 5	365 ± 23	353 ± 25	273 ± 20	156 ± 13	–	–
SD.v1.133	1.60[e]	–	–	142 ± 5	267 ± 20	237 ± 17	193 ± 15	108 ± 10	–	–
SD.v1.328	2.70 ± 0.16[d]	–	–	<10	70 ± 9	138 ± 11	186 ± 14	149 ± 12	92 ± 13	–
SE.v1.165	2.03 ± 0.15[d]	–	–	27 ± 3	108 ± 9	171 ± 13	197 ± 15	146 ± 12	–	–
SF.v1.88	1.57 ± 0.13[d]	–	–	73 ± 4	168 ± 9	268 ± 19	253 ± 19	168 ± 14	–	–
SF.v1.100	2.00 ± 0.13[d]	–	–	50 ± 4	135 ± 9	258 ± 19	271 ± 20	204 ± 16	94 ± 10	–
SG.v1.77	1.53 ± 0.13[d]	–	–	148 ± 9	344 ± 15	238 ± 18	220 ± 17	127 ± 13	–	–
HeLMS08	1.52 ± 0.11[d]	–	–	87 ± 10	227 ± 15	300 ± 22	246 ± 18	170 ± 15	–	–
HeLMS22	2.46 ± 0.18[d]	–	–	13 ± 3	65 ± 10	130 ± 15	180 ± 18	130 ± 15	–	–
HeLMS18	2.07 ± 0.13[d]	–	–	31 ± 3	91 ± 15	163 ± 13	202 ± 15	142 ± 12	–	–
HeLMS2	2.41 ± 0.19[d]	–	–	25 ± 4	146 ± 14	250 ± 18	324 ± 23	247 ± 19	–	–
HeLMS7	1.97 ± 0.14[d]	–	–	33 ± 4	129 ± 7	219 ± 16	227 ± 17	166 ± 13	–	–
HeLMS9	1.18 ± 0.11[d]	–	–	132 ± 4	340 ± 20	367 ± 25	293 ± 21	170 ± 14	–	–
HeLMS13	2.05 ± 0.16[d]	–	–	39 ± 3	168 ± 15	176 ± 13	210 ± 15	134 ± 11	–	–
HeLMS15	2.66 ± 0.17[d]	–	–	14 ± 3	44 ± 8	153 ± 12	186 ± 14	152 ± 13	–	–
HeLMS5	2.73 ± 0.21[d]	–	–	7 ± 3	68 ± 7	149 ± 12	197 ± 15	188 ± 15	–	–
HBoötes03	1.325	3.0 ± 1.5	–	104 ± 5	279 ± 16	323 ± 23	244 ± 18	140 ± 34	–	18.4 ± 2.5
HXMM02	3.395	4.4 ± 1.0	–	29 ± 3	93 ± 15	92 ± 10	122 ± 12	113 ± 11	–	66.0 ± 5.4
Eyelash	2.32591	37.5 ± 4.5[f]	–	25 ± 3	147 ± 7	366 ± 55	429 ± 64	325 ± 49	115 ± 13	106.0 ± 12.0

[a] Dye et al. (2015).

[b] Estimate from CO line luminosity and FWHM from Harris et al. (2012).

[c] Messias et al. (2014).

[d] Redshift estimate from photometric data, using the SED of Eyelash as the template.

[e] Redshift is estimated from both photometric data and a possible (low significance) spectral feature.

[f] Swinbank et al. (2011).

can be seen in the six separate scans of SMM J2135−0102, but they also vary between adjacent scans of different targets. It is not possible to fit polynomial baselines to subtract these ripples.

We tried baseline subtraction to remove the fringes, by subtracting spectra obtained on dark sky on the same observational days (OD) or subtracting an average spectra from off-centre pixels.

Table 3. Far-IR line fluxes of individual galaxies, measured by fitting Sinc-Gaussian profiles to each line. The uncertainties are from the propagation of the fitting error and from bootstrapping in the neighbouring $\pm 5000\,\mathrm{km\,s^{-1}}$ velocity range around the targeted lines, to get the 'local' noise level.

Source	[C II] 158 μm 10^{-18} W m^{-2}	[N II] 122 μm 10^{-18} W m^{-2}	[N II] 205 μm 10^{-18} W m^{-2}	[O III] 88 μm 10^{-18} W m^{-2}	[O III] 52 μm 10^{-18} W m^{-2}	[O I] 63 μm 10^{-18} W m^{-2}	[O I] 145 μm 10^{-18} W m^{-2}	OH 119 μm 10^{-18} W m^{-2}
SDP.9	3.5 ± 0.6	<2.8	<2.5	4.8 ± 1.5	–	–	<1.5	<4.6
SDP.11	6.1 ± 0.4	<1.5	<2.1	4.9 ± 1.0	–	–	<1.4	−2.0 ± 0.7
SDP.17	<2.1	<1.0	–	<2.88	–	<3.6	2.1 ± 0.5	<1.4
SDP.81	2.9 ± 0.6	<2.6	–	2.9 ± 0.5	<3.7	2.1 ± 0.7	<2.7	<2.3
SDP.130	<1.3	<2.6	–	<1.6	–	<3.9	<1.7	<1.4
G09-v1.40	2.5 ± 0.9	<1.4	<2.1	<2.0	–	<6.7	<1.0	<1.3
G09-v1.97	–	<1.7	–	<1.1	3.5 ± 0.6	<2.7	–	<2.2
G09-v1.124	3.0 ± 1.0	<1.3	–	<3.0	–	2.1 ± 0.7	<1.5	<1.1
G09-v1.326	<1.7	<1.2	–	<2.0	–	<4.3	<1.9	<0.8
G12-v2.30	–	<1.5	–	<1.1	<2.6	<2.3	<1.4	<1.7
G12-v2.43	<2.9	<2.1	–	<1.1	<4.3	<4.3	<2.8	<2.3
G12-v2.257	3.4 ± 0.6	<1.1	–	<2.6	–	<4.0	<1.5	<1.1
G15-v2.19	7.9 ± 1.0	<5.2	<1.8	–	–	–	<6.6	<8.0
G15-v2.235	<2.2	<1.5	–	<4.1	–	–	3.5 ± 1.2	<1.4
NA.v1.56	<1.5	<0.7	–	2.3 ± 0.6	–	<3.9	3.0 ± 0.6	<0.9
NA.v1.144	<1.8	<1.2	–	<2.6	–	<3.1	<1.4	<1.4
NA.v1.177	<1.2	<0.8	–	<1.5	<5.1	<3.3	<1.5	<0.8
NA.v1.186	4.2 ± 0.4	<1.7	<1.5	<2.0	–	–	<1.0	<1.7
NB.v1.43	8.8 ± 0.5	<2.6	<2.6	<3.4	–	–	<1.2	<3.3
NB.v1.78	<2.5	<2.6	–	<1.6	<3.9	<3.1	<2.5	<2.2
NC.v1.143	–	<1.7	–	<1.3	<2.2	<1.7	–	<5.5
SA.v1.44	<2.0	<3.0	<1.8	<5.3	–	–	<2.0	<4.0
SA.v1.53	3.7 ± 0.4	<2.8	<2.7	<5.1	–	–	<1.6	<2.8
SB.v1.143	3.9 ± 1.0	<0.8	–	<4.4	–	<2.8	<1.6	<0.9
SB.v1.202	3.1 ± 0.6	<1.0	<2.1	–	–	<9.2	<0.9	<0.8
SC.v1.128	1.5 ± 0.5	<1.2	–	<3.2	–	<3.3	<2.5	<1.2
SD.v1.70	<2.5	<2.4	<1.8	<2.2	–	–	<0.9	<1.2
SD.v1.133	4.1 ± 0.6	<2.7	<2.1	<4.6	–	–	<1.6	−3.4 ± 1.1
SD.v1.328	<1.2	<1.6	–	<1.6	–	<2.7	<1.4	<1.3
SE.v1.165	–	<1.7	–	<1.1	<3.6	<2.0	<1.3	<1.3
SF.v1.88	<1.4	<1.4	<2.4	<3.1	–	–	<1.0	<1.3
SF.v1.100	<2.1	<0.9	–	<2.0	<5.1	<2.9	<2.0	<0.9
SG.v1.77	<1.3	<1.5	–	<2.1	–	<3.8	<1.5	<1.3
HeLMS2	<2.2	<0.6	–	<2.2	–	<2.3	<1.5	<0.9
HeLMS7	<1.3	<1.0	–	<2.3	–	<4.2	<1.8	<0.9
HBootes03	3.1 ± 1.4	<4.0	<3.3	3.1 ± 1.6	–	–	–	<3.8
HXMM02	–	<1.6	–	<0.7	–	<2.0	<2.6	<1.8
Eyelash	5.0 ± 0.7	1.8 ± 0.2	–	–	–	–	<1.5	−2.8 ± 0.4

However, due to small differences in the thermal environment of the telescope, spectrometer fringes remain the dominant source of spectral noise. This is not only because the weak level of the continuum response is not well calibrated, for the science target, for the dark sky, and for the spectra observed with the off-centre pixels, but also because subtracting another spectrum – with a different continuum and telescope model calibration error – adds noise.

Fortunately, these fringes appear as relatively low spatial frequencies which do not seriously impede extraction of parameters from narrow spectral lines. Real line emission displays a relatively narrow width (FWHM) of ∼2–3 GHz, which is the convolution of a typical linewidth of $\sim 500\,\mathrm{km\,s^{-1}}$ and the 1.2 GHz Sinc width at the lowest observing frequency, ∼500 GHz).

We therefore performed baseline fitting designed to subtract the low-frequency features of the spectra. To this end, we masked 2 GHz frequency ranges (corresponding to $\sim 500\,\mathrm{km\,s^{-1}}$ at $z = 2$ for [C II] 158 μm) around the few strong lines ([C II] 158 μm, [O III] 88 μm, and OH 119 μm), then we convolved the masked spectra with a Gaussian profile with 15 GHz FWHM in order to derive an overall local baseline profile which fits the fringes very well and does not contaminate the narrow line features. We then subtracted the baseline profiles from the original spectra to obtain the final spectra for each target. We tested this method by inserting artificial spectral signals into the raw data, subtracting the baseline, then fitting the signal, in order to determine whether we can recover the line flux. The tests demonstrated that a robust flux measurement can be recovered after the baseline subtraction. We present the detailed tested results in Appendix C and show the final spectra of our targets in Appendix D.

The default spectral response of *Herschel* FTS is a Sinc function with a uniform width of ∼1.2 GHz. We present the raw spectra at the original spectral resolution. Measurements of the [C II] spectral line flux densities were made by fitting a Sinc+Gaussian function – considering the large line width of a typical high-redshift DSFG – (e.g. Frayer et al. 1998; Bothwell et al. 2013; Yang et al. 2017) – to each spectra, and a Gaussian function to the stacked spectra. Several FTS spectra from this data set have been published previously (e.g. Valtchanov et al. 2011; George et al. 2013, 2014). Here, we include

re-reductions of those data with the latest pipeline (HIPE v14.2). The line fluxes and uncertainties are shown in Table 3 and cut-out spectral regions around the [C II] 158 μm line are shown in Fig. 3.

3.3 APEX observations and data reduction

To check the [C II] flux and to resolve the line profiles of galaxies detected in our *Herschel* observations, we obtained ground-based observations of SDP.11 and NA.v1.186 with the 12-m Atacama Pathfinder EXperiment (APEX) telescope on the Chajnantor Plateau in Chile, in good (pwv < 0.6 mm) weather conditions. We conducted the observations during the science verification phase of the band-9 Swedish ESO PI receiver for APEX (i.e. SEPIA B9; Belitsky et al. 2018) during 2016 August and September. The project number is E-097.F-9808A-2016.

All observations were performed in a wobbler-switching mode. Beam throws were 2 arcmin, offset in azimuth. The focus was determined using Mars. Pointing was corrected every 30 min using nearby carbon stars, resulting in a typical uncertainty of 2 arcsec (rms). Typical system temperatures were 600–1000 K. The Fast Fourier Transform Spectrometer backend provided a bandwidth of 4 GHz. The beam size was ∼8 arcsec at 670 GHz. All data were reduced with the CLASS package in GILDAS.[5]

We first combine the spectral data of each sub-scan obtained in two different spectrometers, which have 2.5 GHz bandwidth each, and an overlap of 1 GHz. The data from two spectrometers cannot be simply added since sometimes they have different continuum levels (even after the wobbler-switch). The source spectra are centralized in the overlapped region, so the spectrum obtained in each spectrometer only covers one side of the line-free channels (baseline). If the baseline is fitted (and subtracted) to the spectrum from each spectrometer individually, the slope of the order-1 polynomial baseline is little constrained.

To combine the data from the two spectrometer for each individual sub-scan, we fit the spectra in the overlapped frequency range and combine the two spectra with a uniform weighting. We also removed ∼50 MHz at both spectral edges, to avoid poor responses there. Then, we checked the line profiles of the CO transitions in the literature (see Oteo et al. 2017, for SDP.11) and establish the velocity range over which a linear baseline fit will be applied. For NA.v1.186, we set the velocity range to ± 400 km s^{-1}for its emission. Linear baselines were subtracted after inspecting each individual combined spectrum. An automatic quality control is made to get rid of the spectra whose noise is much higher than the theoretical one (Zhang et al. in preparation, details are described in the James Clerk Maxwell Telescope MALATANG survey[6]). Only <5 per cent of the data are thrown away for poor baseline qualities. We converted the antenna temperatures ($T_A^\star$) to flux density using the telescope efficiency of 150 ± 30 Jy K^{-1}, which was determined using Callisto and Mars during the science verification tests. The flux uncertainty is estimated to be ∼25 per cent.

4 RESULTS AND ANALYSIS

4.1 *Herschel* photometry

Fig. 1 presents a colour–colour plot of the *Herschel* SPIRE flux

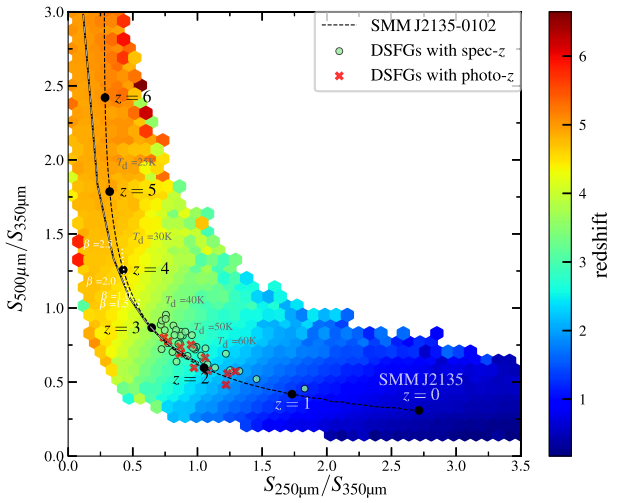

Figure 1. *Herschel* SPIRE flux density ratios for the sample. Sources with known redshifts are displayed as green circles, those without as red crosses. Underlaid are a dashed line displaying the expected flux density ratios of SMM J2135−0102 with changing redshift, determined from the SED presented in Ivison et al. (2010c), and shading displaying the predicted colours of 10^6 modified blackbody sources with a range of redshifts, dust temperatures, dust spectral emissivity indices and a flux density measurement uncertainty of 10 per cent, based on fig. 1 of Amblard et al. (2010). White dotted line indicates the colour track of various β at T_d = 30 K. Grey dash–dotted line indicates the colour track of various T_d, with β = 1.8.

densities of the sample. Following Amblard et al. (2010), we generate >2 × 10^6 SEDs of single-temperature modified blackbodies (MBB) and fill their colours as the background. The MBBs are generated with a flux density F_ν:

$$F_\nu = \varepsilon_\nu B_\nu \propto \frac{\nu^{3+\beta}}{\exp(\frac{h\nu}{kT_d}) - 1}, \quad (1)$$

where ε_ν is the frequency-dependent emissivity, $\varepsilon_\nu \propto \nu^\beta$, T_d is the dust temperature, and β is the dust emissivity index.

To generate these models, we randomly sample a uniform range of T_d from 15 to 60 K, of redshift from 0.1 to 7.0, of β from 1.0 to 2.5. We limit the plots with extreme colour limits of $S_{500}/S_{350} > 3$ and $S_{250}/S_{350} > 3.5$. For computing the colours, we also randomly add an extra noise to each modelled data point with a Gaussian standard deviation of 10 per cent of its flux. Then we bin the modelled data points with a hexagonal binning method and plot the average colours in a hexagonal box. The SPIRE colours of the sample are well within the limits defined by the models we have considered. We adopt the SED template of SMM J2135−0102, shift it to different redshifts and measure the 'observed' S_{500}/S_{350} and S_{250}/S_{350} colours. Then we plot the simulated colours as a dashed line, with their redshifts marked, to compare with the observed values. As displayed, the sample appears relatively similar to the track of SMM J2135−0102 in the observed frame, although the average colours of S_{250}/S_{350} and S_{350}/S_{500} are a little higher than those of SMM J2135−0102. This is expected due to the very high magnification factor experienced by SMM J2135−0102, which allows a less-extreme galaxy with a relatively lower SFR surface density, and therefore a likely lower dust temperature, to reach flux densities comparable to the others in our sample. The distribution and the trend also seem to be consistent with those shown by Yuan et al. (2015), who use different templates to model the SPIRE colour–colour plots in high-redshift DSFGs and show that higher T_d and/or smaller β could produce the observed

[5] http://www.iram.fr/IRAMFR/GILDAS
[6] https://github.com/malatang-jcmt-survey/auto_qualification

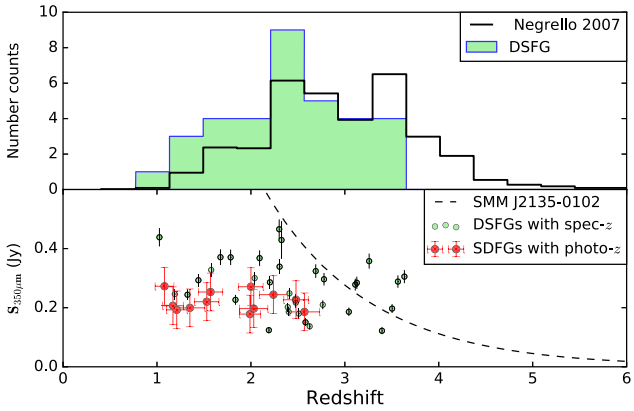

Figure 2. *Upper:* Redshift distribution of sources in the sample. The shaded histogram displays the number of sources within our sample in redshift bins of $\Delta z = 0.36$, and the area under the solid line displays the predicted redshift distribution of strongly lensed DSFGs with $\{S_{250}, S_{350}, S_{500}\} > 100$ mJy from Negrello et al. (2007), scaled to the same number of sources. *Lower: Herschel* SPIRE 350 μm flux densities as a function of the redshift distribution. Vertical lines show the uncertainties in flux density. Horizontal lines show uncertainties in photometric redshifts. The dashed line represents the 350 μm flux density expected to be observed from an SMM J2135−0102-like galaxy at different redshifts.

colours. We also present two tracks to demonstrate the physical parameters that drive the spread of values in Fig. 1. The white dotted line presents the colour track for $T_d = 30$ K, with β varying from 1.0 to 2.5. The grey dash–dotted line presents the track for $\beta = 1.8$, with T_d ranges from 20 to 60 K. The degeneracy between T_d and β is clearly seen from the similarity of the two tracks, whilst the temperature seems to be more sensitive in shifts along the redshift axis.

Fig. 2 shows the spectroscopic redshift distribution of the sample. The redshift distribution of strongly lensed DSFGs predicted by Negrello et al. (2007) has a higher mean value than observed in our sample. This is due partly to the different flux density cuts employed, with our primarily $S_{350} > 200$ mJy subsample of the lens candidates preferentially selecting lower redshift objects than the $S_{500} > 100$ mJy used by Negrello et al. (2007). This is compounded by the methods and instruments used to determine spectroscopic redshifts for our galaxy sample. Further details of specific galaxies are given in Appendix E.

Galaxies at $z > 3$ show higher flux densities than that scaled from Eyelash, indicating that the $z > 3$ galaxies in our sample are on average not only brighter after lensing but much more intrinsically luminous than SMM J2135−0102, which has the highest lensing amplification 37.5 ± 4.5 in the known sample.

4.2 Dust SED modelling

As a first step towards understanding the physical properties of these galaxies, we start by fitting their SEDs using broad-band continuum flux densities from our multiwavelength imaging observations. The SEDs are constructed by combining our recently obtained PACS photometric data with the 250, 350, and 500μm photometric measurements obtained with SPIRE, the 850 μm flux densities measured with the Submillimetre Common-User Bolometer Array 2 onboard JCMT (Holland et al. 2013; Bakx et al. 2018), the 880 μm flux densities measured with SMA (Bussmann et al. 2013), the 1.2 and 2 mm data measured with the Institut de Radioastronomie Millimétrique's NOrthern Extended Millimeter Array (NOEMA; Yang et al. 2016) and the 1.4 GHz radio continuum data from the literature (Becker, White & Helfand 1995). We list the measured FIR flux densities at *Herschel* wavelengths in Table 2.

We first used a single-temperature MBB model to fit the observed dust SEDs. However, more than half of the sources could not be fitted adequately with a single MBB, indicating that either multiple excitation components are needed, or the assumption of a single-MBB dust emission does not hold. Also, the dust emission is assumed to be optically thin, which may not be valid for our extreme targets. The MBB fitting is also biased by the data in the Wien regime, meaning that the luminosities are systematically underestimated. On the other hand, there are not enough data points at the longer wavelengths to fit two independent MBB models for most of the sources.

Instead, we estimate the dust properties with a power-law temperature distribution method introduced by Kovács et al. (2010). We model the FIR SEDs with dust emission following a thermally motivated power-law distribution of dust masses, M_d, with temperature components T: $\frac{dM_d}{dT} \propto T^{-\gamma}$, and a low-temperature cutoff. This model does not assume optically thin dust emission everywhere and this simple prescription can reproduce both the Wien and Rayleigh–Jeans sides of the FIR peak. For consistency, all sources are modelled using this method, regardless of previous independent determinations of their SEDs.

For the SED modelling for the high-redshift DSFGs, we fit the blackbody model and a power-law synchrotron emission component simultaneously. Thermal free–free emission is unlikely to contaminate strongly in our fitting wavelengths (e.g. Aravena et al. 2013), so we excluded it from the fitting. The power-law index, γ, of the dust is fixed to be 7.2, the best-fitting value found in local starbursts (see Kovács et al. 2010); the dust spectral emissivity index, β, is fixed at 1.8, the true value of which likely varies inversely with temperature (Knapp, Sandell & Robson 1993; Mennella et al. 1998; Dunne et al. 2000); the characteristic photon cross-section to mass ratio of particles κ_0 is assumed to be $\kappa_{850\,\mu m} = 0.15\,m^2\,kg^{-1}$ (see Kovács et al. 2010); the conversion from L_{IR} to SFR follows Kennicutt & Evans (2012) with a Kroupa initial mass function (IMF) (Kroupa & Weidner 2003); the synchrotron spectral index, α, is fixed as −0.75 for objects with less than two photometric measurements at $\lambda_{rest} > 4$ mm (e.g. Ibar et al. 2010b).

Total infrared luminosities and dust masses are comparable to those estimated for these galaxies via other methods, such as MAGPHYS (Negrello et al. 2014), or a single grey-body component (Bussmann et al. 2013). However, the fitted SFRs are higher than those suggested by MAGPHYS, which is likely due to the different adopted calibrations. To compare the total IR luminosity ($S_{IR}^{8-1000\,\mu m}$) with the radio continuum observations, we also calculate q_{IR}, following Ivison et al. (2010a,b), as $q_{IR} = \log_{10}[(S_{IR}/3.75 \times 10^{12}\,W\,m^{-2})/(S_{1.4GHz}/W\,m^{-2}Hz^{-1})]$, where $S_{1.4\,GHz}$ is K-corrected assuming $S_\nu \propto \nu^\alpha$, again with $\alpha = -0.75$. Finally, we list the derived properties, such as L_{IR}, SFR, M_{dust} and T_d^{cutoff} in Table 4.

In Fig. 4, we plot correlations and distributions for a few of the parameters we have fitted. It is not surprising that the gravitational amplification factor, μ, is weakly anticorrelated with the intrinsic infrared luminosity, L_{IR}, after correcting the lensing magnification. This is because correspondingly higher μL_{IR} is required for higher redshift sources to reach our $S_{350\mu m} > 200$ mJy flux density threshold.

We find a tentative trend of decreasing q_{IR} with increasing redshift, indicating a potential variation of the IR-radio correlation with redshift. This is consistent with the decreasing trend found recently

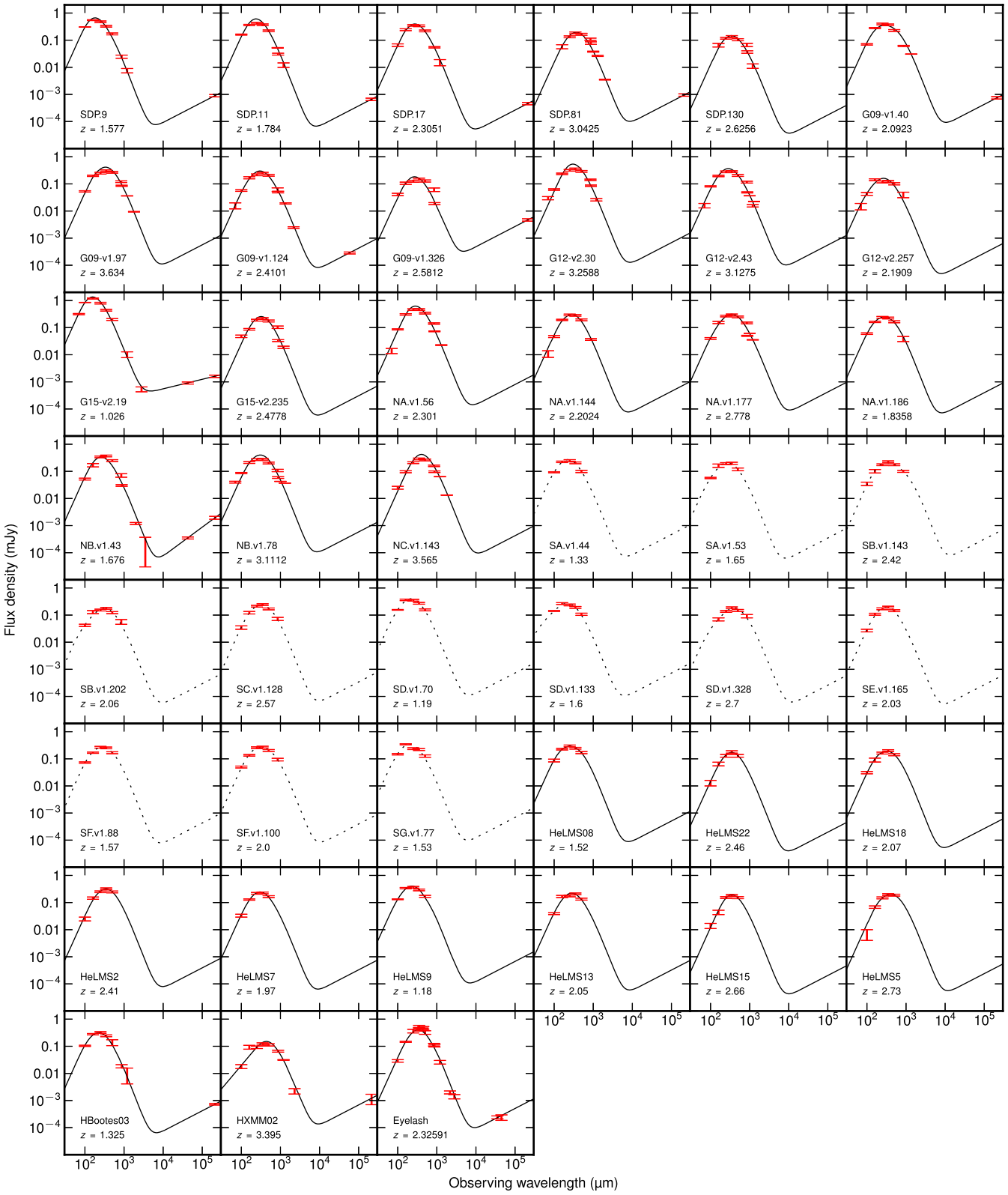

Figure 3. SED fits to available FIR–radio photometry for objects in the sample, using the power-law dust temperature distribution model of Kovács et al. (2010). Sources selected from the *H*-ATLAS SGP field do not have secure redshifts, and fits for these sources are performed assuming a best-fitting photometric redshift and are shown as a dotted line.

Table 4. Properties from the SED fits described in Section 4.2. In addition, H_2 masses from CO measurements are shown, taken from Iono et al. (2006, 2012), Frayer et al. (2011), Fu et al. (2012), Harris et al. (2012), Lupu et al. (2012), Danielson et al. (2013), Ivison et al. (2013), Messias et al. (2014). These were converted to $L'_{\rm CO\,1-0}$ where necessary by the brightness temperature ratios given in Bothwell et al. (2013), and then to a molecular gas mass via an $\alpha_{\rm CO}$ conversion factor of $0.8\,{\rm M}_\odot\ \left({\rm K\,km\,s^{-1}\,pc^2}\right)^{-1}$.

Source	Amplification	$\mu M_{\rm H_2}$ $10^{11}\,{\rm M}_\odot$	$\mu L_{\rm IR}$ $10^{12}\,{\rm L}_\odot$	$L_{\rm IR}$ $10^{12}\,{\rm L}_\odot$	SFR ${\rm M}_\odot\,{\rm yr}^{-1}$	$M_{\rm d}^{\rm tot}$ $10^{8}\,{\rm M}_\odot$	$T_{\rm d}^{\rm cutoff}$ K	$q_{\rm IR}$
SDP.9	8.8 ± 2.2	1.9 ± 0.5	71.5 ± 2.4	8.1 ± 1.9	1200 ± 300	2.2 ± 1.0	36.1 ± 3.4	2.78 ± 0.10
SDP.11	10.9 ± 1.3	2.4 ± 0.3	68.9 ± 2.3	6.3 ± 0.7	900 ± 100	3.8 ± 0.9	34.9 ± 1.6	2.78 ± 0.10
SDP.17	4.9 ± 0.7	4.3 ± 0.6	76.7 ± 3.1	15.7 ± 2.2	2300 ± 300	13.5 ± 4.2	27.8 ± 1.7	2.73 ± 0.12
SDP.81	15.9 ± 0.7	3.8 ± 0.2	58.0 ± 4.0	3.7 ± 0.3	550 ± 50	2.6 ± 0.5	38.9 ± 3.8	2.02 ± 0.13
SDP.130	2.1 ± 0.3	1.7 ± 0.2	31.8 ± 2.8	15.1 ± 2.5	2300 ± 400	29.6 ± 6.6	24.1 ± 1.4	–
G09-v1.40	15.3 ± 3.5	3.3 ± 0.8	65.1 ± 2.1	4.3 ± 0.9	600 ± 130	7.4 ± 1.0	43.5 ± 2.9	2.54 ± 0.11
G09-v1.97	6.9 ± 0.6	5.0 ± 0.4	212.0 ± 6.0	30.8 ± 2.0	4600 ± 300	5.3 ± 1.9	50.7 ± 1.6	–
G09-v1.124	1.1 ± 0.1	2.2 ± 0.2	64.5 ± 4.9	58.6 ± 5.9	8800 ± 900	82.0 ± 12.6	24.4 ± 1.6	2.40 ± 0.22
G09-v1.326	5.0 ± 1.0[a]	2.7 ± 0.5	47.2 ± 1.9	9.4 ± 1.5	1400 ± 200	4.5 ± 1.7	30.8 ± 4.4	1.40 ± 0.12
G12-v2.30	9.5 ± 0.6	7.1 ± 0.5	202.0 ± 7.0	21.3 ± 1.2	3200 ± 170	5.6 ± 1.8	37.3 ± 1.2	–
G12-v2.43	17.0 ± 11.0[a]	1.3 ± 0.8	150.0 ± 3.8	8.8 ± 4.8	1300 ± 700	2.8 ± 1.6	31.7 ± 3.0	–
G12-v2.257	13.0 ± 7.0[a]	1.4 ± 0.8	34.0 ± 1.2	2.6 ± 0.9	400 ± 100	2.7 ± 3.7	24.8 ± 2.3	–
G15-v2.19	9.0 ± 1.0	2.9 ± 0.3	58.1 ± 2.0	6.0 ± 0.5	900 ± 100	2.4 ± 0.8	35.2 ± 1.9	3.0. ± 0.07
G15-v2.235	1.8 ± 0.3	3.5 ± 0.6	49.8 ± 1.8	27.7 ± 4.2	4100 ± 600	23.3 ± 6.0	35.3 ± 1.8	–
NA.v1.56	11.7 ± 0.9	5.8 ± 0.4	109.0 ± 4.4	9.3 ± 0.8	1400 ± 110	7.3 ± 1.8	31.1 ± 1.7	–
NA.v1.144	4.4 ± 0.8	1.8 ± 0.3	54.8 ± 2.1	12.5 ± 2.4	1900 ± 300	6.9 ± 2.2	40.1 ± 3.7	–
NA.v1.177	–	4.2	94.1 ± 3.0	18.8 ± 2.8	2800 ± 600	1.6 ± 0.4	34.7 ± 3.2	–
NA.v1.186	–	3.6	32.7 ± 1.3	6.5 ± 1.4	1000 ± 200	7.4 ± 2.1	28.8 ± 2.2	–
NB.v1.43	2.8 ± 0.4	3.6 ± 0.5	31.2 ± 1.3	11.1 ± 1.6	1700 ± 400	24.7 ± 4.9	23.8 ± 1.2	1.67 ± 0.09
NB.v1.78	13.0 ± 1.5	4.6 ± 0.5	156.0 ± 7.2	12.0 ± 1.4	1800 ± 400	2.5 ± 0.5	49.7 ± 4.4	–
NC.v1.143	11.3 ± 1.7	6.2 ± 0.9	153.0 ± 6.1	13.5 ± 1.9	2000 ± 300	9.6 ± 2.3	35.2 ± 3.7	–
SA.v1.44	–	–	18.2 ± 0.9	3.6 ± 0.8	540 ± 120	5.5 ± 1.7	26.1 ± 2.1	–
SA.v1.53	–	–	22.9 ± 0.8	4.6 ± 0.8	680 ± 90	5.7 ± 1.2	27.3 ± 1.9	–
SB.v1.143	–	–	55.5 ± 3.2	11.1 ± 1.5	1700 ± 250	14.6 ± 4.3	30.9 ± 3.7	–
SB.v1.202	–	–	35.1 ± 3.1	7.0 ± 2.5	1000 ± 200	5.5 ± 2.1	29.9 ± 4.5	–
SC.v1.128	–	–	54.4 ± 2.4	10.9 ± 1.3	1600 ± 230	9.1 ± 2.3	31.7 ± 3.2	–
SD.v1.70	–	–	23.5 ± 2.8	4.7 ± 1.1	700 ± 200	6.7 ± 1.1	27.0 ± 2.6	–
SD.v1.133	–	–	25.3 ± 3.9	5.1 ± 0.4	760 ± 200	3.8 ± 0.7	28.9 ± 2.0	–
SD.v1.328	–	–	42.4 ± 2.7	8.5 ± 1.3	1300 ± 240	13.1 ± 1.5	29.3 ± 3.4	–
SE.v1.165	–	–	37.2 ± 3.3	7.4 ± 1.7	1100 ± 300	7.3 ± 0.9	29.6 ± 2.9	–
SF.v1.88	–	–	34.8 ± 1.4	7.0 ± 1.3	1000 ± 300	7.0 ± 1.3	29.3 ± 2.3	–
SF.v1.100	–	–	51.2 ± 2.8	10.2 ± 2.4	1500 ± 400	12.4 ± 2.6	30.6 ± 2.8	–
SG.v1.77	–	–	49.4 ± 1.7	9.9 ± 1.3	1500 ± 400	3.3 ± 0.8	33.6 ± 2.4	–
HeLMS08	–	–	14.1 ± 0.6	2.8 ± 0.3	420 ± 100	10.7 ± 2.4	23.3 ± 1.9	–
HeLMS22	–	–	32.6 ± 2.2	6.5 ± 1.1	970 ± 180	9.1 ± 1.8	28.3 ± 3.8	–
HeLMS18	–	–	40.9 ± 1.8	8.2 ± 1.2	1200 ± 200	6.5 ± 1.4	30.5 ± 3.0	–
HeLMS2	–	–	75.3 ± 4.4	15.1 ± 2.0	2300 ± 300	11.5 ± 1.9	33.5 ± 3.0	–
HeLMS7	–	–	53.9 ± 1.9	10.8 ± 2.5	1600 ± 340	6.8 ± 1.3	32.3 ± 2.8	–
HeLMS9	–	–	33.1 ± 1.0	6.6 ± 1.1	1000 ± 290	6.8 ± 1.3	29.1 ± 2.0	–
HeLMS13	–	–	70.7 ± 2.6	14.1 ± 2.1	2100 ± 300	3.8 ± 1.0	27.2 ± 2.9	–
HeLMS15	–	–	30.1 ± 1.6	6.0 ± 9.6	900 ± 140	13.0 ± 3.4	35.1 ± 4.1	–
HeLMS5	–	–	82.3 ± 7.5	16.5 ± 3.3	2500 ± 500	7.5 ± 2.0	37.9 ± 3.3	–
HBoötes03	3.0 ± 1.5	1.0 ± 0.5	20.8 ± 0.9	6.9 ± 1.4	1000 ± 200	6.9 ± 1.9	23.8 ± 6.2	2.51 ± 0.09
HXMM02	5.33 ± 0.19[b]	3.4 ± 0.8	66.2 ± 6.5	15.1 ± 3.3	2300 ± 500	24.1 ± 7.0	23.0 ± 2.3	1.87 ± 0.22
Eyelash	37.5 ± 4.5	5.6 ± 0.7	62.3 ± 2.9	1.7 ± 0.2	250 ± 30	2.4 ± 0.6	33.3 ± 3.4	2.15 ± 0.26

[a] Amplification estimate from CO line luminosity and FWHM from Harris et al. (2012).
[b] Amplification estimate from ALMA 870 μm data (Bussmann et al. 2015).

in the 3 GHz survey in the COSMOS field (Delhaize et al. 2017). However, our results indicate much shallower slope index, whose significance is very limited by the current sample size.

The total infrared luminosity $L_{\rm IR}$ shows an good increasing correlation with fitted dust mass, $M_{\rm d}$, over two orders of magnitude, which is also expected since all targets in the sample show similar dust temperatures and far-IR colours. The correlation shown in the targets with lensing correction seems consistent with that shown in targets without lensing corrections.

The median redshift (including both photo-z and spec-z) for the whole sample is 2.5 ± 0.6, with a redshift range spanning z = 1.0–3.6. The intrinsic $L_{\rm IR}$ spans from 10^{12} to $10^{13.5}$ ${\rm L}_\odot$, with a median of $\sim 10^{13}$ ${\rm L}_\odot$, indicating their starburst natures.

In the end, we find that the redshift does not show significant correlation with the intrinsic $L_{\rm IR}$, indicating that our sample is not potentially biased to more luminous targets at higher redshifts, although they are selected with flux cutoffs.

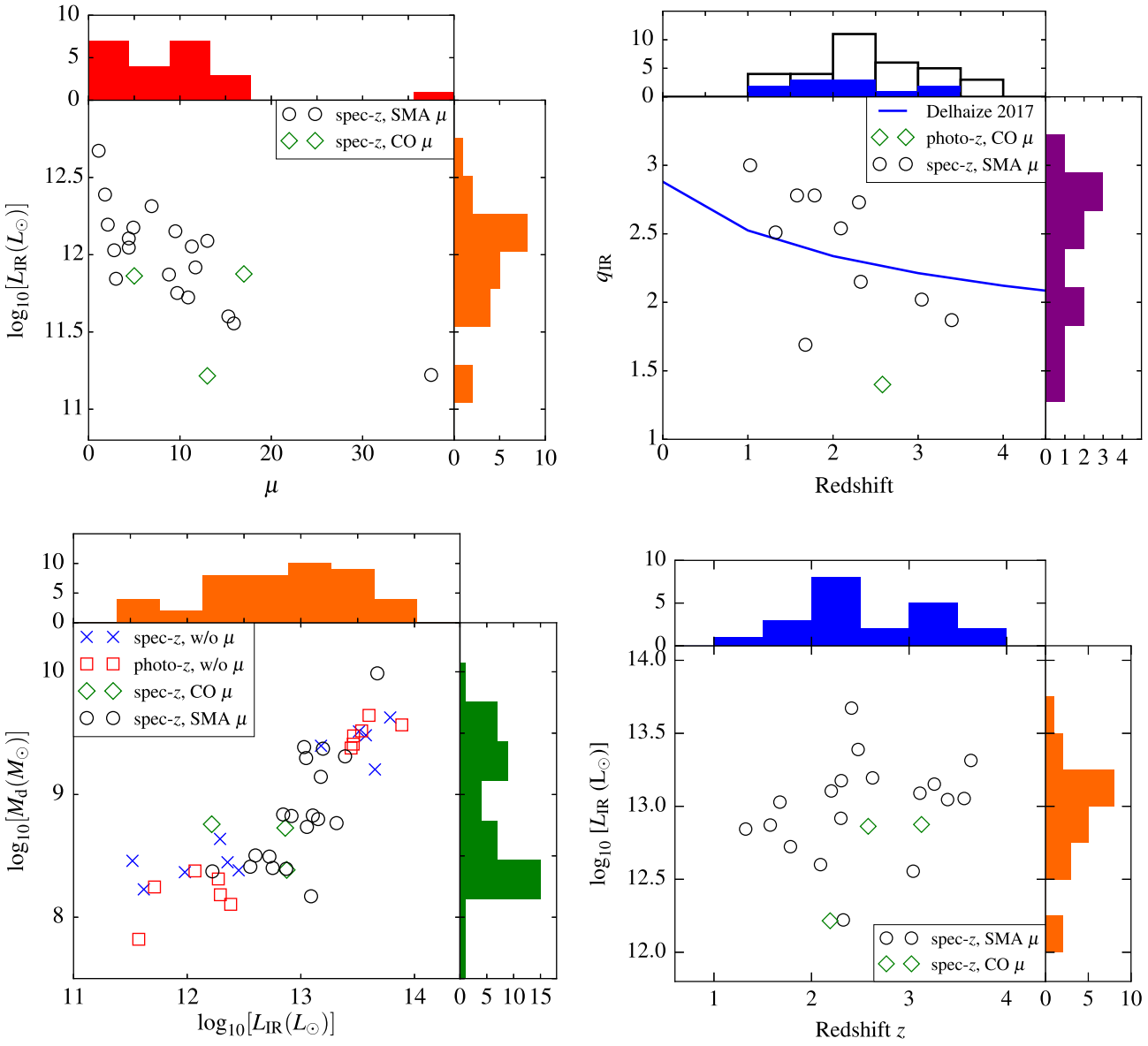

Figure 4. Distributions and correlations of SED fit parameters. *Upper left:* The distributions of gravitational amplification factor μ and the total infrared luminosity, $L_{\rm IR}$ (8–1000 μm). *Upper right:* The distribution of redshift and the total infrared to radio correlation factor $q_{\rm IR}$. The blue line shows the infrared-radio correlation fitted in star-forming galaxies in the COSMOS field (i.e. Delhaize et al. 2017): $q_{\rm TIR}(z) = (2.88 \pm 0.03)(1+z)^{-0.19 \pm 0.01}$. The open histogram (black) shows the redshift distribution of the whole sample. *Lower left:* The distributions of total infrared luminosity and the fitted dust mass $M_{\rm d}$, after lensing amplification corrections. For targets without amplification factors (blue cross and red squares), we have divided by a factor of 5 for both axes, in order to compare with the de-lensed results. *Lower right:* The distributions of redshift and the total infrared luminosity after lensing correction. Filled histograms (in colour) show the distribution of the sample. Open circles represent systems with known redshifts and lens models, primarily from Bussmann et al. (2013). Green diamonds represent targets with known redshifts, but with estimates of gravitational amplification factors only from their CO line characteristics (Harris et al. 2012). Blue crosses represent sources with known redshifts, with no existing lens model. Red squares represent sources with photometric redshifts, as shown in Table 2.

4.3 Magnification factors

Gravitational amplification values are primarily taken from Bussmann et al. (2013) that are derived from SMA data in preference to values derived from Near-IR imaging (e.g. Calanog et al. 2014; Dye et al. 2014), due to the likelihood of a physical separation (and hence amplification difference) of the starburst and existing stellar population (Fu et al. 2012; Dye et al. 2015; Hodge et al. 2016; Oteo et al. 2017). Most galaxies in the sample are strongly lensed, with a median amplification of around 10×, distributed between 1 and 15×. SMM J2135−0102 is an outlier with its very high amplification factor.

When fitting dust SED and measuring lines ratios, we neglect the possibility of differential lensing at different wavelengths, which may bring in extra uncertainties (e.g. Hezaveh, Marrone & Holder 2012; Serjeant 2012; Yang et al. 2017). The lensed status of this sample could complicate the modelling of their SEDs, particularly the low-temperature dust components which may not be co-spatial with hotter dust near the starburst. This similar ef-

fect could also be important for optical and near-IR flux density measurements and modelling (e.g. Negrello et al. 2014; Ma et al. 2015).

The different origins of the fine-structure ionized lines make differential lensing more severe. Resolved observations have shown that the [N II] emission is more extended than the [O III] emission in local galaxies (e.g. Hughes et al. 2015). Besides, [C II] originates from multiple gas phases, making it more extended than the [N II] emission, which has been seen in the Milky Way galaxy, local galaxies and galaxies at high redshift (e.g. Goldsmith et al. 2015; Pavesi et al. 2016; Lapham, Young & Crocker 2017). However, the line ratios of the same species at the same energy level, e.g. the two [NII] lines and the two [O III] lines, are expected to be not as severe as those of species from different origins. Detailed studies on the differential lensing effect need very high-quality high-resolution images at all studies wavelengths, and are highly dependent on the model interpretation, which is beyond the scope of our study.

5 SPECTROSCOPY RESULTS

Herschel spectra of all our targets are presented in Appendix D. In galaxies with known spectroscopic redshifts, we report individual detections of nine [C II] 158 μm emission lines, four [O III] 88 μm lines, three [O I] 145 μm lines, two [O I] 63μm lines, one [O III] 52μm line, one [N II] 122μm line, and one OH 119 μm line in absorption. For galaxies without spectroscopic redshifts, we estimate their photometric redshift based on the FIR-based photometric redshifts fitting method (for details, see Ivison et al. 2016), which fits FIR templates of different high-z galaxies. We adopt the best fits using the ALESS template and add the difference between different templates to the final error. We then search for lines within a range of $z_{\rm phot} \pm 0.5$ ($\sim 3\sigma$), and find five possible [C II] emission lines at $z_{\rm phot} \pm 0.5$ (one of these, SD.v1.133, with a possible OH 119 μm absorption feature), thus yielding five plausible new spectroscopic redshifts. These redshifts need to be confirmed with follow-up observations before they are considered robust.

We also compare the [C II] spectra of SDP.11 and NA.v1.186 obtained with *Herschel* and those observed with APEX, which are shown in Fig. 5. For SDP.11, the velocity-integrated [C II] flux obtained with APEX is $265 \pm 65\,{\rm Jy\,km\,s^{-1}}$, fully consistent with our *Herschel* detection, $269 \pm 30\,{\rm Jy\,km\,s^{-1}}$. This is also close to the [C II] flux measured with the second-generation z(Redshift) and Early Universe Spectrometer (ZEUS-2) on APEX (Ferkinhoff et al. 2014). We note that the [C II] line profile of SDP.11 is resolved into two velocity components, separated by $\sim 300\,{\rm km\,s^{-1}}$, which were not resolved by either the *Herschel* or ZEUS-2 observations. We also overlay the CO J = 4 → 3 spectrum with the [C II] lines, and find that the twin-peaked profile of the APEX [C II] line is consistent with CO (also for HCN) detections in Oteo et al. (2017), likely indicative of a merger. For NA.v1.186, our APEX observations give a [C II] flux of $310 \pm 90\,{\rm Jy\,km\,s^{-1}}$, around 60 per cent higher than that obtained from *Herschel* ($190 \pm 40\,{\rm Jy\,km\,s^{-1}}$), but in agreement within the uncertainties.

5.1 [C II] 158 μm as a diagnostic of ISM properties

The 158 μm [C II] fine-structure transition is often the brightest observed FIR emission line. With the Atacama Large Millimeter/submillimeter Array (ALMA) now operational, interest in the interpretation of [C II] 158 μm emission from high-redshift galaxies has increased in recent years.

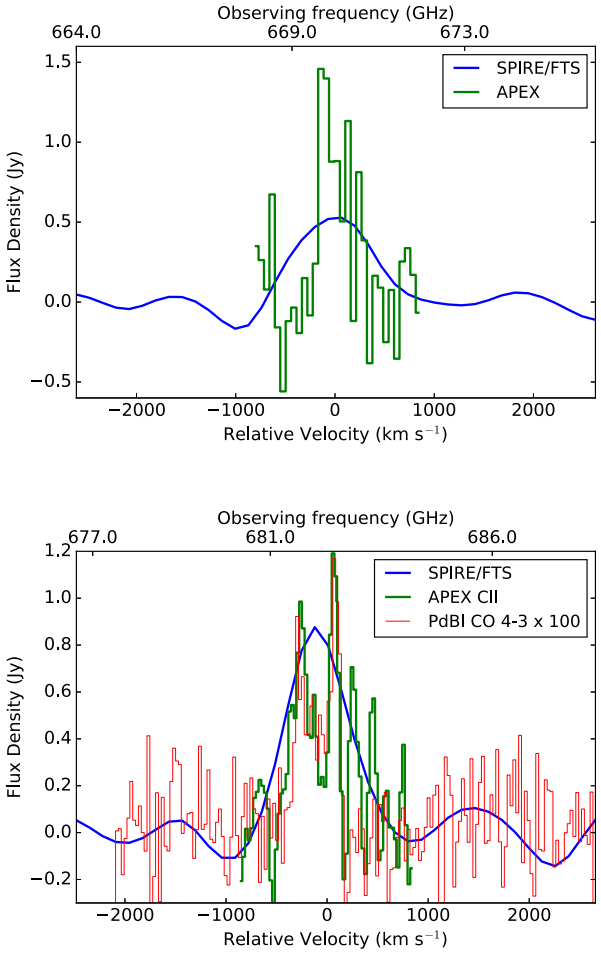

Figure 5. *Upper:* [C II] spectra of NA.v1.186. The blue line shows the un-apodized *Herschel* FTS spectrum, and the green line shows the APEX spectrum. *Lower:* [C II] and CO J = 4–3 spectra of SDP.11. The blue line shows the un-apodized *Herschel* FTS spectrum, the green line shows the APEX spectrum, and the thin red line shows the CO J = 4–3 spectrum (multiplied by 100×) obtained with the PdBI (Oteo et al. 2016).

[C II] has been reported to have an apparent relative decrease in the gas cooling efficiency with increasing radiation field intensity, dust temperature, and/or SFR (e.g. Abel et al. 2009; Stacey et al. 2010; Díaz-Santos et al. 2013, 2014; Herrera-Camus et al. 2018a,b). The fraction of energy transmitted via this line is not constant, however, exhibiting a well-known decrease in the $L_{\rm line}/L_{\rm FIR}$ ratio with increasing $L_{\rm FIR}$ in the local Universe (Luhman et al. 2003). This results in the brightest (ultra-)luminous infrared galaxies (ULIRGs) exhibit the highest deficits. Compared with nearby normal quiescent star-forming spirals, the luminosity ratio between [C II] and the FIR continuum emission decreases by more than an order of magnitude in extreme star-forming systems (e.g. LIRGs and ULIRGs; Díaz-Santos et al. 2013, 2014). The relationship also hold in spatially resolved measurements on scales of a few hundreds pc, e.g. surveys of KINGFISH (Smith et al. 2017b), Great Observatories All-sky LIRG Survey (GOALS; Díaz-Santos et al. 2014), SHINING (Herrera-Camus et al. 2018a), with lower values found in the nuclei of galaxies than in the extended discs, and the trend may be even more pronounced with $L_{\rm FIR}/M_{\rm H_2}$ (e.g. Graciá-Carpio et al. 2011).

Several theories have been proposed to explain this deficit. The ionization parameter, U, and hence dust temperature and SFR surface density, appear to be strongly correlated with the line-to-continuum ratio (Díaz-Santos et al. 2013), with the most extreme values of all three parameters found in the dense merging nuclei of low-redshift ULIRGs. Resolved observations and detailed modelling (Herrera-Camus et al. 2018a,b) show that not only the high ionization parameter, but also the reduction in the photoelectric heating efficiency make the [CII] line not able to trace the FUV radiation field. Dust grain charging in higher radiation fields, leading to a lower photoelectric gas-heating efficiency, may additionally play a role (Malhotra et al. 1997). Column density will also have an effect as [C II] 158 μm is primarily produced in PDRs, with a small contribution from H II regions for local galaxies (e.g. Abel 2006); the column density at which the [C II] becomes luminous is then governed by the ionization parameter and dust extinction. FIR continuum radiation, however, can also be produced by non-PDR sources. Lines of sight through high optical depth molecular material to a PDR and starburst will contain a substantial continuum contribution from the molecular region, as well as from the HII region close to the ionizing source. This increases the FIR continuum emission and, at very high column densities, the optical depth to the lines may become large enough to reduce their observed flux. Croxall et al. (2012) found that the [C II]/$L_{\rm IR}$ ratio decreases with increasing dust temperature traced by the $F_{70\mu m}/F_{100\mu m}$ colour, while the [N II]/$L_{\rm IR}$ ratio keeps unchanged. The [C II] deficit was also found to have a relationship with the ionization state of small grains, revealed from polycyclic aromatic hydrocarbons (PAH) features (i.e. Croxall et al. 2012).

This effect appears to continue at high redshift, albeit potentially to a lower extent (e.g. Stacey et al. 2010). While the global SFRs in high-redshift DSFGs often equal or exceed those found in local ULIRGs, significant differences may exist in the distribution of gas and star formation within these two populations. In some systems, a larger volume of gas may be illuminated by a lower flux of ionizing photons, producing both a smaller ionization parameter, U, and a lower optical depth. Díaz-Santos et al. (2013) and Gullberg et al. (2015) discuss the deficit and correlations with other parameters in further detail, in particular with emission area and molecular gas mass, for low- and high-redshift galaxies, respectively.

Our $L_{[\rm C\,II]\,158\,\mu m}/L_{\rm FIR}$ measurements are plotted in Fig. 6 along with values from local and high-redshift starburst galaxies. Gravitational lensing has allowed us to push intrinsic luminosities towards or below those of local ULIRGs, and our sources occupy much of the space between the highest redshift ALMA detections (primarily with $L_{\rm FIR} > 10^{13}\,{\rm L}_\odot$) and low-redshift systems (typically with $L_{\rm FIR} < 3 \times 10^{12}\,{\rm L}_\odot$). We see a spread in $L_{[\rm C\,II]\,158\,\mu m}/L_{\rm FIR}$, from $\sim 3 \times 10^{-3}$ to 3×10^{-4}, suggesting that the local relation does not hold at higher redshifts; however, the non-detections may have lower ratios. These values appear to confirm other observations indicating that – for starburst-dominated systems at least – the deficit is lower for high-redshift ULIRGs than for their low-redshift cousins, likely resulting from a lower intensity of ionizing radiation due to their similar total star formation occurring over a larger volume.

The line-to-continuum ratio is expected to correlate more strongly with $L_{\rm FIR}/M_{\rm H_2}$ (Graciá-Carpio et al. 2011) and our measurements – plotted in Fig. 6 using gas masses derived from CO luminosities – agree with this theory. Fig. 6 also shows that the overall scaling relation derived from local star-forming galaxies (Herrera-Camus et al. 2018a) and our data are also fully consistent with the same trend.

In addition to the total IR luminosity, the FIR lines – as coolants of star formation heated gas – may be used to trace the instantaneous SFR. Since it is often the brightest line, [CII] 158 μm is of primary interest. The conversion is non-linear, however, due to the changing efficiency of these lines with increasing SFR. Sargsyan et al. (2014) and Herrera-Camus et al. (2015) discuss the effectiveness of [C II] 158 μm as a tracer of SFR in the local Universe, noting that [C II] 158 μm can provide measurements consistent with other star formation tracers, such as PAH emission and MIR emission lines, but that any calibration may require additional corrections, applicable to more strongly star-forming sources, such that SFRs derived from continuum measurements may be superior.

Literature calibrations from these local samples are presented in the form $\frac{\rm SFR}{\rm M_\odot\,yr^{-1}} = A\left(\frac{L_{[\rm C\,II]\,158\,\mu m}}{\rm L_\odot}\right)^B$, where $A = 1.22 \times 10^{-8}$, $1 \pm 0.2 \times 10^{-7}$, and 1.00×10^{-7}, and $B = 1.034$, 1, and 0.983 from De Looze et al. (2011), Sargsyan et al. (2014) and Herrera-Camus et al. (2015), respectively. For our highest signal-to-noise [C II] 158 μm detection, that of SMM J2135−0102, these suggest SFRs of 40, 165, and 120 $\rm M_\odot\,yr^{-1}$, the range reflecting the inherent dispersion in the observed $L_{[\rm C\,II]\,158\,\mu m}$/SFR ratios. An equivalent calibration derived from high-redshift data has $A = 3.02 \times 10^{-9}$ and $B = 1.18$ (De Looze et al. 2014), with the higher exponent value accounting for the decreasing line-to-continuum ratio in galaxies with the high infrared luminosities discovered at such redshifts. For SMM J2135−0102, this calibration suggests an SFR of 230 $\rm M_\odot\,yr^{-1}$, fully consistent with the 250 $\rm M_\odot\,yr^{-1}$ that we estimate from our photometric $L_{\rm IR}$ fit.

Recently, Herrera-Camus et al. (2018a,b) present new scaling relations based on several physical properties of galaxies and classifications, including separation from the main-sequence of star-forming galaxies, star formation efficiency, and AGN/LINER/pure starburst categories. Using the calibration for galaxies above the main sequence (Herrera-Camus et al. 2018a), the SFR of Eyelash is $\sim$160 $\rm M_\odot\,yr^{-1}$, slightly below our fitted SFR, but consistent with the values obtained in Sargsyan et al. (2014) and Herrera-Camus et al. (2015).

An extension to these $L_{[\rm C\,II]\,158\,\mu m}$–SFR relationships exploits local resolved galaxies to consider surface densities. Díaz-Santos et al. (2013) derive a relationship for the nuclei of a large sample of LIRGs, which appears to hold for high-redshift objects (Díaz-Santos et al. 2014), and which can be re-arranged as

$$\log_{10}\left(\frac{\rm area}{\rm kpc^2}\right) = \log_{10}\left(\frac{L_{\rm IR}}{\rm L_\odot}\right) + \frac{\log_{10}\left(\frac{L_{[\rm C\,II]\,158\,\mu m}}{L_{\rm FIR}}\right) - 1.21 \pm 0.24}{0.35 \pm 0.03}. \quad (2)$$

The resulting surface areas suggested for our sample are typically within a factor of a few of the demagnified areas we have adopted (these can be fairly uncertain), primarily from the lens modelling of Bussmann et al. (2013), and are compatible with the low-redshift scatter. As shown in Fig. 6 (right-hand panel), the $L_{[\rm C\,II]\,158\,\mu m}/L_{\rm IR}$ ratio shows a decreasing trend with surface density of SFR, $\Sigma_{\rm SFR}$, following exactly the same trend found in local starbursts and high-redshift galaxies in the literature (Smith et al. 2017b; Spilker et al. 2016). The compactness of the star formation activities seems to be a very tight correlation with the $L_{[\rm C\,II]\,158\,\mu m}/L_{\rm IR}$ ratio. There seems to have a slight trend with redshift as well, possibly due to the selection biases – only the most intensive, high surface-density starbursts can be selected in the more distant Universe. Highest lensing magnification occurs within a small angular area,

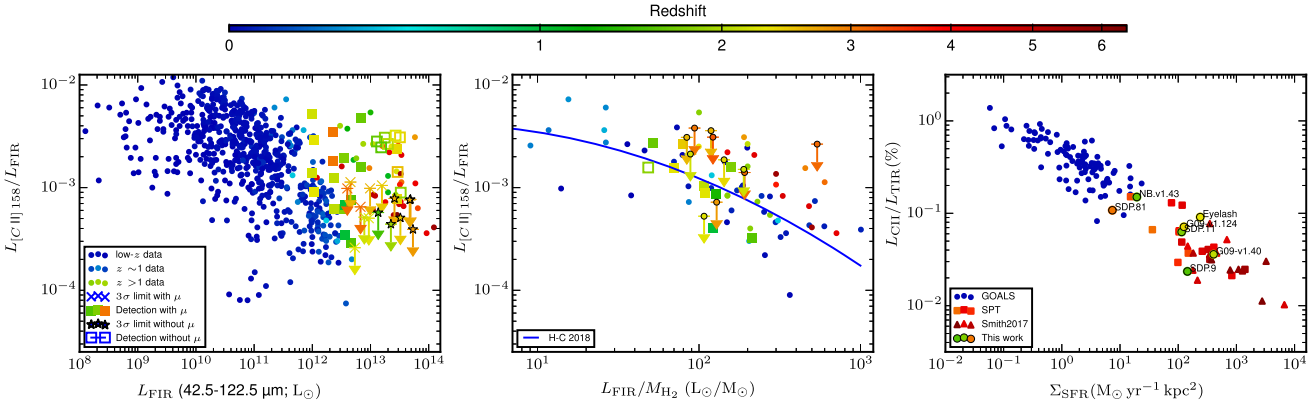

Figure 6. *Left*: The well-known $L_{[\mathrm{C\,II}]\,158\,\mu\mathrm{m}}/L_{\mathrm{FIR}}$ deficit, locally and at high redshift in starburst-dominated galaxies. Data from this work are shown as squares, or downward arrows indicating 3σ upper limits. Filled points have FIR luminosities corrected for magnification, non-filled points use magnification estimates from SED fitting. Low-redshift data are taken from Brauher et al. (2008), Díaz-Santos et al. (2013), Sargsyan et al. (2014), González-Alfonso et al. (2015), Ibar et al. (2015), Rosenberg et al. (2015). Data at $z \sim 1$ are from Stacey et al. (2010), Farrah et al. (2013), Magdis et al. (2014). Higher redshift data are taken from Cox et al. (2011), Swinbank et al. (2012), Wagg et al. (2012), Riechers et al. (2013, 2014), De Breuck et al. (2014), Rawle et al. (2014), Gullberg et al. (2015). Where necessary, luminosities have been scaled from literature measurements by the mean of the values from our SED fits $L_{\mathrm{FIR}}(42.5–122.5\ \mu\mathrm{m}) = 0.60\ L_{\mathrm{IR}}(8–1000\ \mu\mathrm{m})$. *Middle*: The [C II]/$L_{\mathrm{FIR}}$ ratio as a function of $L_{\mathrm{FIR}}/M_{\mathrm{H_2}}$, which should correlate more strongly than the continuum luminosity alone (e.g. Graciá-Carpio et al. 2011). Gas masses are determined from integrated-galaxy CO observations, converted to CO J = 1−0 luminosities where necessary. The blue line shows the scaling relation for [CII]/FIR–FIR/$M_{\mathrm{H_2}}$ found in local star-forming galaxies (Herrera-Camus et al. 2018a). *Right*: The [C II]/L_{TIR} ratio as a function of surface density of SFR, Σ_{SFR}. This expands the KINGFISH-GOALS-High-z compilation of Smith et al. (2017b), with additional data from Spilker et al. (2016). There are six new measurements from this work, which have both [C II] detection and size estimate, labelled with inner-colourized black circles. This plot includes data from the GOALS sample (Díaz-Santos et al.), SPT sample (Gullberg et al. 2015; Spilker et al. 2016), and high-redshift galaxies collected from the literature (Walter et al. 2009a; Carniani et al. 2013; Riechers et al. 2013, 2014; Wang et al. 2013a; De Breuck et al. ; Neri et al. 2014; Yun et al. 2015; Díaz-Santos et al. 2016; Oteo et al. 2016; Smith et al. 2017b).

so compact starbursts allow a higher fraction of the total luminosity to be located within the lensed area.

6 REST-FRAME STACKING

In individual spectra of the sample, only the brightest FIR cooling lines may be detected. Recently Wardlow et al. (2017); Wilson et al. (2017) stacked *Herschel*-PACS and *Herschel*-SPIRE spectra of DSFGs at high redshift and detected ionized fine-structure lines, such as [O IV] 26 μm, [S III] 33 μm, [OIII] 52 μm, and neutral lines, such as CI 158 μm, [OI] 63 μm. Here, we stack our *Herschel*-SPIRE spectra to probe the faint lines.

6.1 Spectral stacking

To search for fainter lines, and to determine the evolution of the average properties of the population as a whole, we stacked the observed spectra in the rest frame. In principle the noise should reduce as $\sqrt{n}$, where n is the number of stacked spectra, when weightings are not considered. Different stacking techniques have been adopted in the literature (e.g. Spilker et al. 2014; Wardlow et al. 2017; Wilson et al. 2017) for various scientific purposes, which give different weightings to the data. In the following sections, we present three different stacking methods to explore the average physical properties in the sample and the potential biases of the stacking techniques.

Before stacking, we applied apodization to convolve the spectral response from a Sinc function to reduce sidelobes and generate a more 'Gaussian-like' profile (i.e. Naylor & Tahic 2007, see also HIPE manual). To stack spectra with different redshifts (see Section 6), the spectra need to be blueshifted to the rest frame, where the widths of the Sinc function for each galaxy increases with redshift by $1 + z$, i.e. from 2.6 GHz at $z = 1.2$ to 5.5 GHz at $z = 3.6$, compared to the 1.2 GHz width of the system response of the *Herschel*-SPIRE. If we simply add/average together the same line from different redshifted galaxies without apodization, the sidelobes of the Sinc functions (of different widths) tend to cancel each other, which biases the stacked signal.

To match the velocity resolution across the sample at the rest frequency, we vary the Gaussian width of the apodization with redshift, where width $=((z - 1.5)/2 + 1.1) \times 1.20671$ GHz, which ensures a roughly uniform velocity resolution at any given rest frequency. For the one galaxy at $z < 1.5$, G15-v2.19, we use a Gaussian width of 1.1 GHz. Converting from the Sinc function to the Gaussian function may raise the flux by 5 per cent (e.g. Hopwood et al. 2015), which we consider as an extra source of error in the final flux estimate. To avoid the noisy edges of the spectra in both SLW and SSW, which are heavily affected by ripples, we do not include the very edge of the spectral ends in the stacking. For SLW, we exclude 30 channels at the low-frequency end and 120 channels at the high-frequency end; for SSW, we exclude 30 channels at both ends of the spectra.

The first method stacks spectra using their intrinsic de-lensed line luminosities. This can only be applied to the sources with both known spectroscopic redshifts and amplification factors. This method focuses on the intrinsic properties of the galaxies and mitigates the influence of the highly non-uniform lensing factors for different targets (and thus frequency coverage, since the targets all lie at different redshifts). However, the sample size is limited by the numbers of galaxies with lensing models (23 out of 38 galaxies with *Herschel*-SPIRE spectra).

We blue shift all apodized spectra to the rest frame, then convert flux densities to luminosity densities (spectral luminosity) with their luminosity distances. To arrive at de-lensed intrinsic properties, we divide the luminosity by their amplification factors (from e.g. Bussmann et al. 2013). Then we create an empty output spec-

trum covering the total frequency range in the rest frame, with a frequency sampling step equivalent to the minimum of all individual spectra (to avoid undersampling the high-redshift end). After re-sampling the rest-frame de-lensed spectra (in luminosity density) into the template output spectrum, we average all of them for each channel using $1/\sigma^2$ weighting, which is controlled by the noise level appropriate for this specific channel. The final output is a spectrum in de-lensed mean line luminosity density. The final noise level is a channel-based function. The spectra resulting from this intrinsic stacking method is displayed in Fig. 7.

The second method uses a similar stacking technique as Spilker et al. (2014), taking advantage of the negative *K*-correction in the submm wavelength regime. We use SMM J2135−0102 as a 'master' template, and blue-shift (or red-shift for galaxies with $z <$ 2.326) all measured spectra to its redshift ($z = 2.32591$). We then scale all spectra by their 500μm continuum flux relative to the value measured for SMM J2135−0102. In this way, the lensing factors for all of our spectra are scaled to a value similar to that of SMM J2135−0102 at 500 m, so the stacked spectrum should have a similar amplification factor as SMM J2135−0102.

The blue-shifted and scaled spectra are then stacked together using $1/\sigma^2$ weighting. This stacking method does not require amplification factors, and thus avoids the associated uncertainties. All spectra with known redshifts can be used, regardless of lensing models, so this method can be applied for a relatively large sample of galaxies. Comparing to the results from the first stacking technique, this approach can reveal any potential bias in the different stacking methods. We present the spectrum obtained using this scaling method in Fig. 8.

The third method is based on median, instead of the mean, to avoid weightings that may bias to the more luminous or higher signal-to-noise spectra. We normalize all spectra with their infrared luminosities, $L_{\rm IR}$, blueshift spectra to their rest frames, and then calculate the median value across all spectra for each channel bin. When calculating the median values, we do not adopt weightings, i.e. equal weighting. Such a stacking method can avoid systematic biases by a few strong targets and is robust to test if the weakly detected lines are common (more than 50 per cent) in the sample. We present the spectrum obtained using the median stacking method in Fig. 9. In principle, an straight (non-weighted) stacking would also be little biased by noise, but such method could only results in a detection of the [C II] line and a marginal detection of the [O III] 88 μm line.

From the line ratios of multiple far-IR lines, calculated between the intrinsic stacked spectrum and the scaling stacked spectrum, the amplification factor of the scaling stacking method is ∼15–30 (depending on the specific line), higher than the mean value of the amplification factors.

This is because the scaling stacking method has a systematic bias. We have scaled all spectra to the 500 μm flux of Eyelash, which actually has the highest flux in the sample. This would actually artificially bias all spectra to a higher amplification factor (compared to the mean value) for the final stacked spectrum. Furthermore, the higher S/N of Eyelash and its very high amplification factor (∼37.5 Swinbank et al. 2011) may further biases the final amplification to high values.

6.2 SED stacking

To probe the average dust properties and the mean IR luminosity, we also stack the IR photometry data and generate a mean intrinsic SED. We combine all the IR photometry data for each target, blue shift the PACS, SPIRE, and 1.4 GHz radio fluxes to their rest frequencies, derive the luminosity for each band, and correct for the lensing magnifications. Then we fit a single MBB with a power-law synchrotron emission. The stacked mean SED and the rest-frequency luminosities of the continuum data are shown in Fig. 10. We fit the SED with a single MBB with a dust emissivity slope index of $\beta = 1.8$, resulting a dust temperature of $\sim 45 \pm 5$ K, close to the SED modelling and dust temperatures measured in DSFGs at similar redshifts (e.g. Swinbank et al. 2014). The average dust mass is $3.7 \pm 0.5 \times 10^8\,{\rm M}_\odot$, which corresponds to an H_2 gas mass of $\sim 3.7 \pm 0.5 \times 10^{10}\,{\rm M}_\odot$, when a typical dust-to-ISM mass ratio of ∼100 is adopted for metal-rich galaxies (e.g. Swinbank et al. 2014; Scoville et al. 2017).

6.3 Molecular absorption features

In the two weighted stacked spectra, we find clear absorption corresponding to the OH 119 μm feature, with robust individual detections seen in the spectra of G09-v2.19 and SMM J2135−0102, the latter presented first by George et al. (2014). If we remove SMM J2135−0102 and G09-v2.19 from the sample then the OH absorption feature remains after re-stacking. In the median stacked spectrum, the OH 119 μm absorption feature is still clearly detected. This indicates that this OH 119μm absorption feature is likely common for the DSFGs in our sample, and is not dominated by a few strong targets.

Blueshifted OH 163 μm line has also been observed in emission towards high-redshift galaxies (Riechers et al. 2014). This feature provides further evidence that out-flowing molecular gas may be common within the high-redshift DSFG population, despite being difficult to observe. However, further analysis of this detection is beyond the scope of this work.

To derive the equivalent width of the OH absorption line, we create another stack designed to include both the line emission and the continuum. We take the SED models derived in Section 3.1, interpolate the SED to the observed frequency of the absorption line, then add the continuum intensity. We then stack the spectra with the added continuum contribution, adopting the same weighting scheme as in Section 6 for consistency. Finally, we fit a second-order polynomial baseline to the continuum and normalize the spectra to unity to derive the equivalent width. These continuum-adjusted, stacked spectra are shown in Fig. 11. The uncertainties on the integrated opacities were estimated as $\Sigma_\tau \sqrt{\delta V \, \Delta V_{1/2}}$ where Σ_τ is the rms uncertainty on the opacity for the velocity resolution δV and $\Delta V_{1/2}$ is the half-maximum velocity width.

The critical densities of the two OH $^2\Pi_{3/2}$ J = 5/2–3/2 transitions are very high (Table 5) and their upper level energies are ∼120 K. This makes it difficult to excite these transitions to high-J levels – we can anticipate that most of the OH molecules are in the ground state and well mixed in the low-density gas along the line of sight. This assumption is supported by the fact that we do not detect any obvious signals of another ground transition of OH J = 3/2–2/1 at 79μm, nor the other high lying doublet of OH $^2\Pi_{3/2}$–$^2\Pi_{1/2}$ J = 3/2–2/1 at 84.6μm (see Fig. 11). These transitions were detected in absorption or emission in nearby local compact (U)LIRGs, e.g. Mrk 231, NGC 4418, and Arp 220, where multiple transitions of OH have been detected with absorption depths comparable to their 119μm OH features (e.g. Sturm et al. 2011; González-Alfonso et al. 2012; Spoon et al. 2013).

We follow the method in González-Alfonso et al. (2014) to calculate the theoretical ratios of the equivalent width between OH 119,

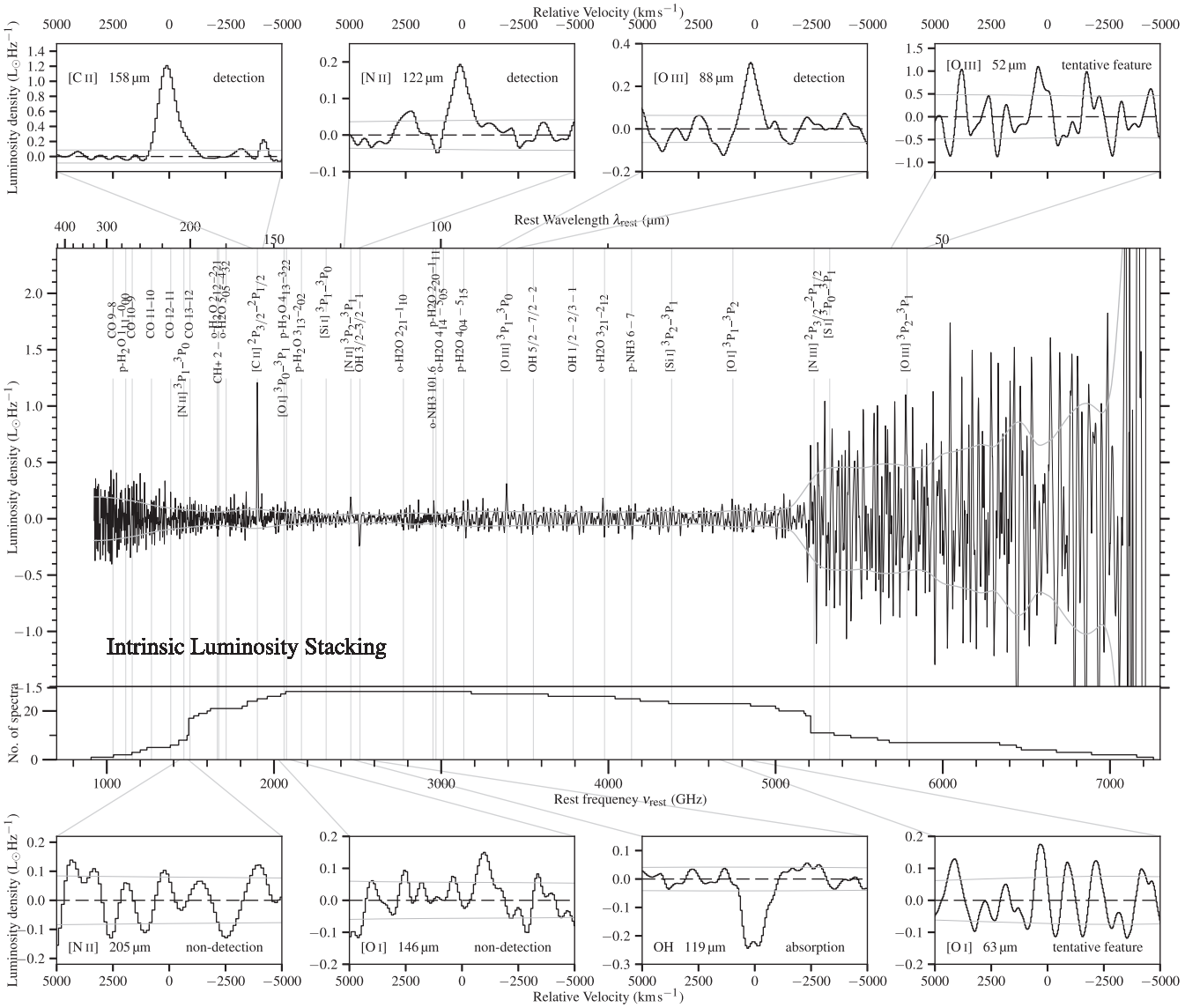

Figure 7. *Upper centre*: Rest-frame intrinsic (de-lensed) luminosity stack of all spectra where secure redshifts are in hand. Markers denote the positions of the primary spectral features expected. *Lower centre*: The number of spectra contributing to the stacked spectrum. *Upper and lower*: $\pm 5000\,\mathrm{km\,s^{-1}}$ cuts around the positions of the primary atomic and ionic spectral lines analysed elsewhere in this work, plus the OH 119 μm doublet.

OH 84, and OH 79μm. For optically thin absorption and ignoring any possible emission components and assuming a uniform filling factor of unity (i.e. recovering all of the continuum emission in the line of sight), the equivalent width of the absorption lines is given by

$$W_{\rm eq} = \lambda^3 g_{\rm u} A_{\rm ul} \frac{N^{\rm l}_{\rm OH}}{8\pi g_{\rm l}}, \qquad (3)$$

where λ is the wavelength, $A_{\rm ul}$ is the Einstein coefficient for spontaneous emission, $g_{\rm u}$ and $g_{\rm l}$ are the statistical weighting factors of the upper and lower levels, and $N^{\rm l}_{\rm OH}$ is the OH column density in the lower transition, which is $^2\Pi_{3/2}$ J = 3/2 for OH 119μm.

In the optically thin limit, the OH119-to-OH84 equivalent width ratio is ~ 0.84. Although the OH 84μm absorption line is often seen in local (U)LIRGs at similar equivalent width as the 119μm line (González-Alfonso et al. 2015, 2017), we have only a non-detection for the OH 84μm line in our stacked spectra. This indicates that the OH population at the $^2\Pi_{3/2}$ J = 5/2 energy level is much less than that on the ground level, $^2\Pi_{3/2}$ J = 3/2. This means that the average excitation of OH in our lensed DSFGs is low, with most OH molecules in the ground energy level, and there are much fewer OH molecules in the J = 5/2 level than the J = 3/2 level, compared to what has been found in local ULIRGs.

On the other hand, the OH119-to-OH79 equivalent width ratio is ∼39.3, which is consistent with the non-detection of the OH 79μm absorption line in our stacked spectrum, supporting the relatively optically thin assumptions. However, in local (U)LIRGs, both lines are often detected at similar equivalent widths, which show optically thick conditions (e.g. González-Alfonso et al. 2017).

Unfortunately, our spectral resolution (around $\sim 400\,\mathrm{km\,s^{-1}}$ at 119μm) hinders attempts to identify any P-Cygni profiles, or to set constraints on the maximum velocity of the OH lines, given the signal-to-noise ratio of our stacked spectrum, even without apodization applied. For nearby local ULIRGs and QSOs, Veilleux et al.

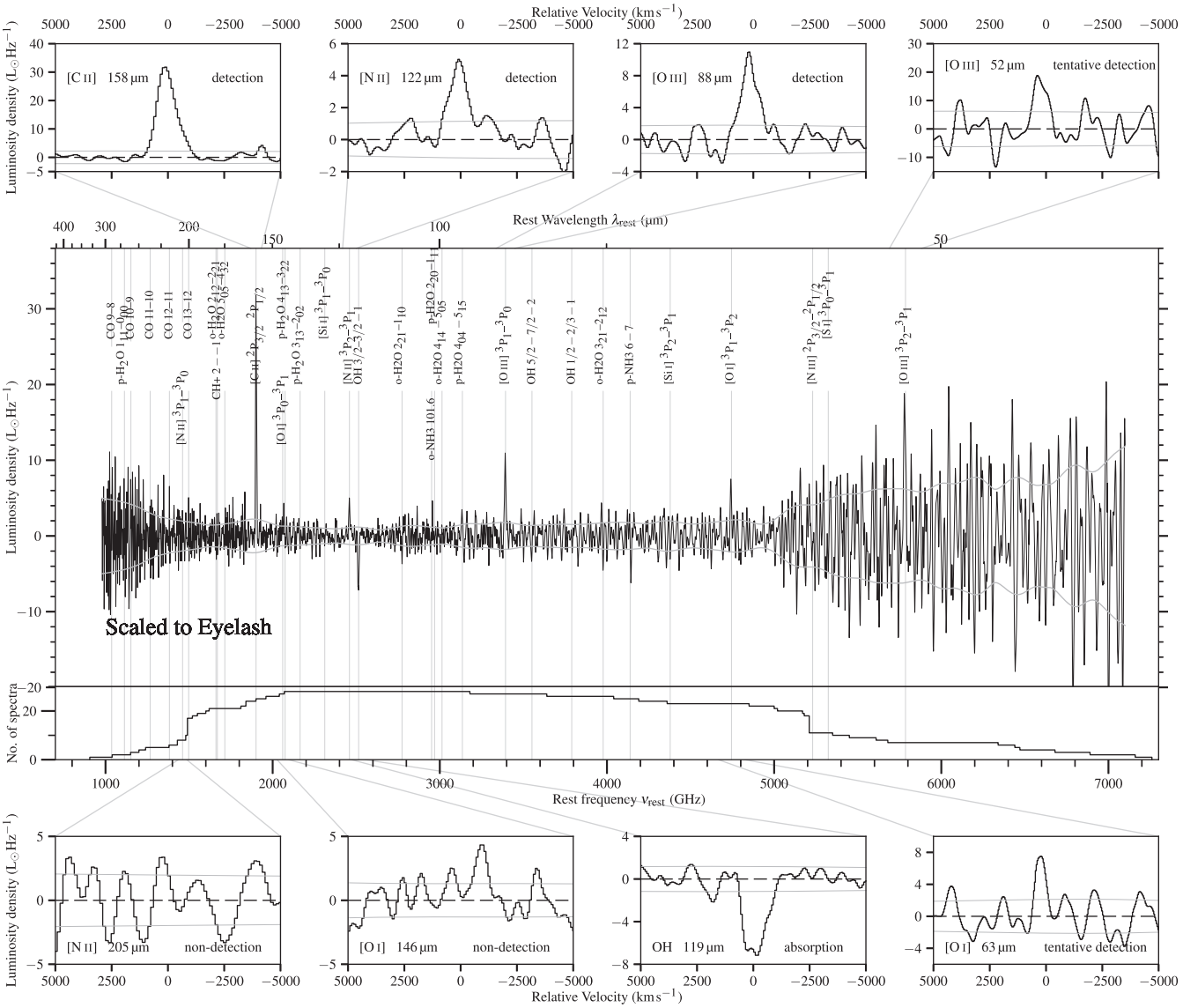

Figure 8. *Upper centre*: Scaling stacked spectrum, with all spectra scaled to the 500 μm flux of SMM J2135−0102. Markers denote the positions of the primary expected spectral features. *Lower centre*: The number of spectra contributing to this stacked spectrum. *Upper and lower*: ±5000 km s^{-1} cuts around the positions of the primary atomic and ionic spectral lines analysed elsewhere in this work, plus the OH 119 μm doublet.

(2013) found a median outflow velocity of around −200 km s^{-1}. Such a velocity for the DSFGs would not be resolved by our data. We fit identical Gaussian profiles to both transitions of the OH absorption doublet and find their line centres to be consistent with their rest frequencies.

Following George et al. (2014), we can estimate an upper limit for the OH column density assuming optically thin OH absorption. To derive the optical depth of the absorption lines, we assume that the filling factor of the continuum source and the foreground molecular gas is unity. The line optical depth, $\tau(v)$, is given by

$$\tau(v) = -\ln\left(\frac{I(v) - I_{\rm cont}}{I_{\rm cont}}\right), \tag{4}$$

where $I(z)$ is the depth of the absorption relative to the continuum level as a function of velocity z and $I_{\rm sat}$ is the continuum intensity. The equivalent width of the OH 119μm absorption features is estimated to be ∼1050 km s^{-1}. We calculate the total OH column density following Mangum & Shirley (2015) and George et al. (2014):

$$N^{\rm OH}_{\rm total} = \frac{4\pi}{h\nu}\, Q(T_{\rm ex}) \frac{1}{B_{\rm ul} g_{\rm u}} \frac{\exp\left(\frac{E_{\rm u}}{k_{\rm B} T_{\rm ex}}\right)}{\exp(-h\nu/k_{\rm B}T_{\rm ex}) - 1} \int \tau {\rm d}V, \tag{5}$$

where we assume optically thin lines and a filling factor of unity. $E_{\rm u}$ is the upper level energy of this transition, $Q(T_{\rm ex})$ is the partition function (where we adopt the Q values given by the JPL data base[7]), $g_{\rm u} = 2J + 1$ (where J is the rotational quantum number), $k_{\rm B}$ is the Boltzmann constant, and h is the Planck constant. $B_{\rm ul} = A_{\rm ul}/(2h\nu^3/c^2)$, where $A_{\rm ul} = \frac{64\pi^4\nu^3}{3hc^3}|\mu|^2$ is the Einstein coefficient for

[7] http://spec.jpl.nasa.gov/ftp/pub/catalog/doc/d017001.cat

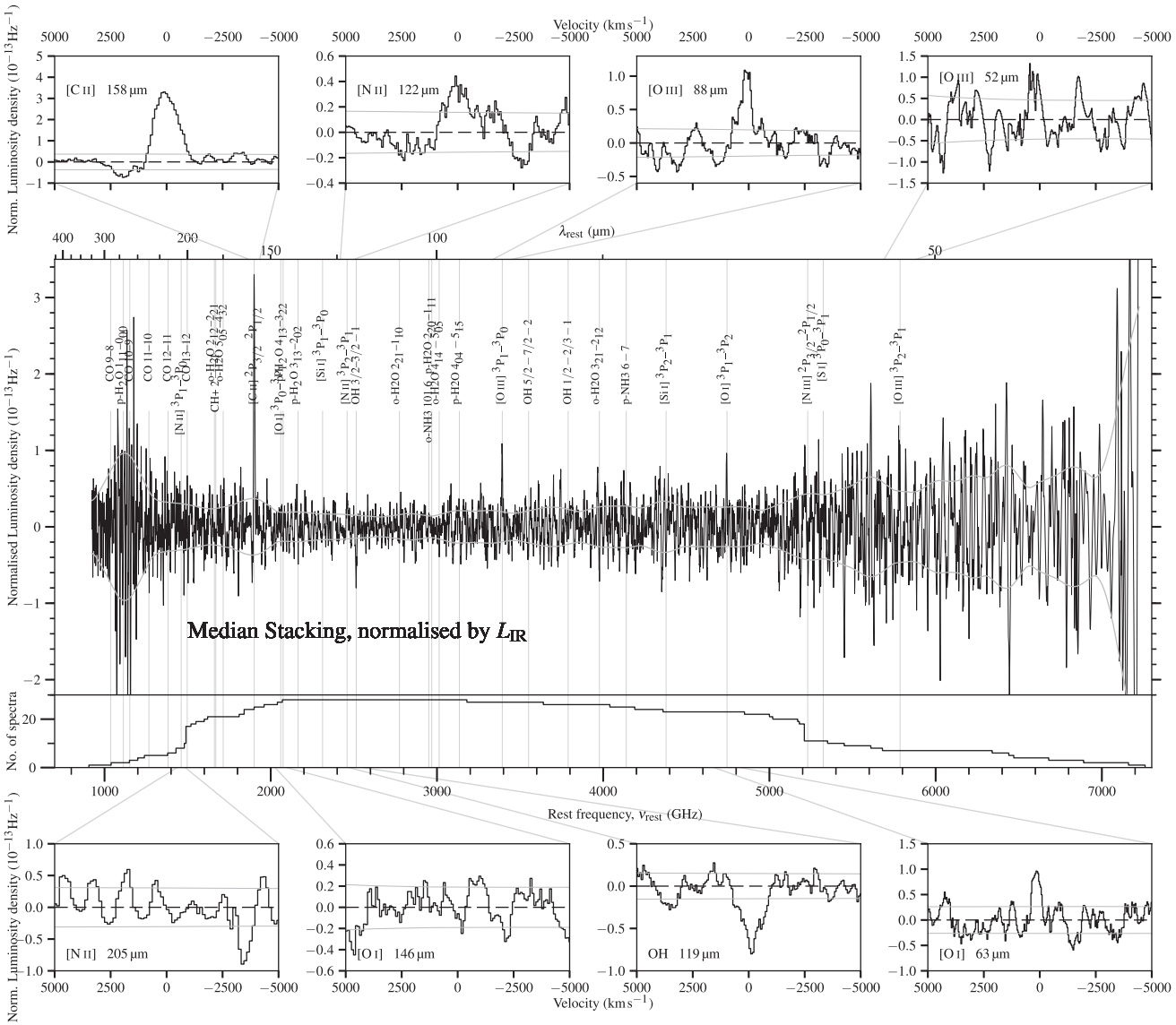

Figure 9. *Upper centre*: Median stacked spectrum, with all spectra normalized to their own $L_{\rm IR}$. Markers denote the positions of the primary expected spectral features. *Lower centre*: The number of spectra contributing to this stacked spectrum. *Upper and lower*: $\pm 5000\,{\rm km\,s^{-1}}$ cuts around the positions of the primary atomic and ionic spectral lines analysed elsewhere in this work, plus the OH 119 μm doublet.

spontaneous emission, μ is the electric dipole moment, and ν is the rest frequency of the line.

As shown in aforementioned discussion, the non-detection of 84 and 79μm lines indicates that the OH excitation is low. We therefore adopt a low excitation temperature of 9 K (comparable to the cosmic microwave background temperature, $T_{\rm cmb}$, at $z = 2.5$) and derive an estimate of the OH column density: $\sim 2 \times 10^{15}\,{\rm cm^{-2}}$. Assuming the OH abundance is the same as the Galactic value, $X_{\rm OH} = 5 \times 10^{-6}$ (e.g. Goicoechea & Cernicharo 2002), the average H_2 column density is $\sim 4 \times 10^{20}\,{\rm cm^{-2}}$, which is considerably lower than the typical H_2 column densities found in SMGs (e.g. Simpson et al. 2017), which indicates that either the OH abundance in DSFGs is much lower than that found in local galaxies or, more likely, that the observed OH is associated with out-flowing gas and does not trace the total column of H_2.

7 ATOMIC AND IONIZED LINES

The [C II] 158 μm and [O I] 63 μm lines often dominate the cooling of neutral gas in starburst galaxies: and ionic fine-structure lines like [N II] and [O III] normally dominate the FIR cooling of the ionized gas, which is mostly in H II regions (e.g. De Looze et al. 2014; Hughes et al. 2015). The [O III], [N II], and [O II] lines at optical wavelengths have the strongest cooling in H II regions (e.g. Osterbrock & Ferland 2006), but most of the optical cooling lines are absorbed by dust gains in the dusty starburst galaxies. Dust grains re-emit most of the incident FUV and optical radiation in the FIR and as a result the luminosity ratio, [O I]/FIR, [O III]/FIR, and [C II]/FIR, typically ∼0.01–0.1 per cent in high-redshift DSFGs (see Fig. 6) provides an estimate of the efficiency of gas heating. This value is, however, affected by the non-negligible fraction of [C II] 158 μm produced in H II regions, the strong dependence of the

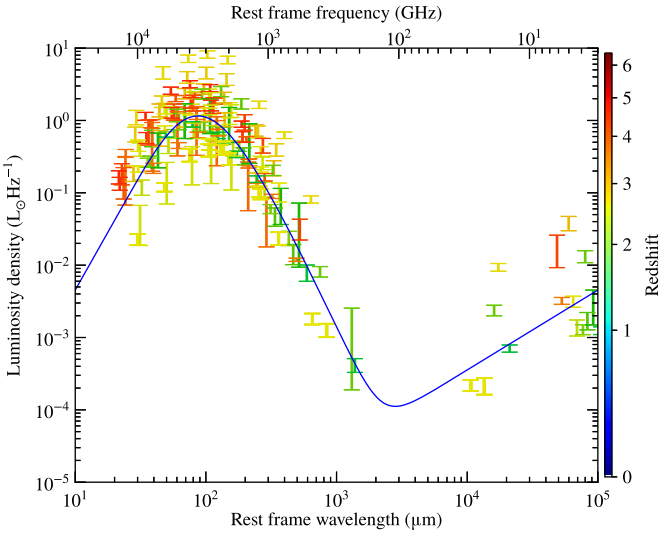

Figure 10. The rest-frame stacked SED (blue line) derived from fitting the power-law dust temperature distribution model (i.e. Kovács et al. 2010) to all demagnified photometric points (colourful dots) of the members of the sample for which lensing model and spectroscopic redshift are available. Colours show the different redshifts of the sources.

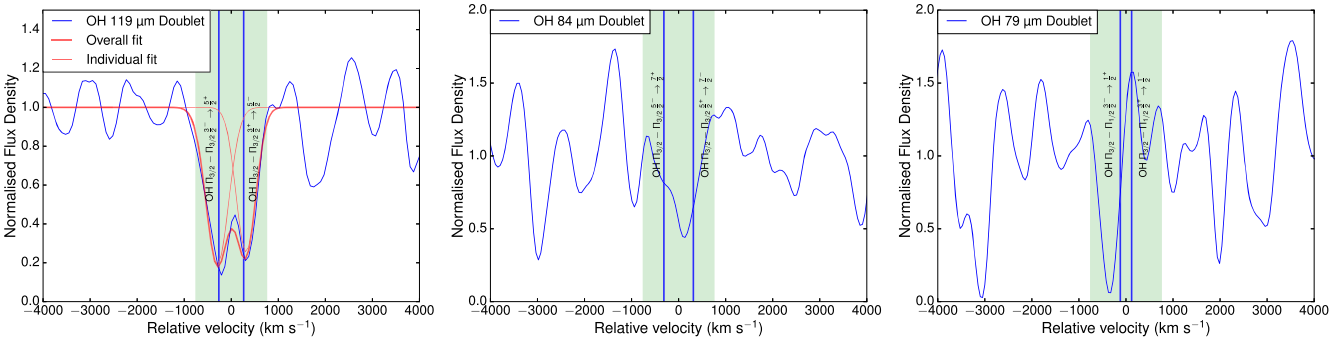

Figure 11. Normalized OH line profile of the stacked spectrum, using their intrinsic luminosity and continuum contribution interpolated from SED fitting. *Left:* Stacked OH 119 μm spectrum. The absorption feature is fitted with two Gaussian components, centred at the rest frequencies of the OH doublet transitions, $\nu_{\rm rest}$ =2514.31 GHz for OH $\Pi_{3/2}$–$\Pi_{3/2}\,\frac{5}{2}^{-}$–$\frac{3}{2}^{+}$ and $\nu_{\rm rest}$ = 2509.95 GHz for OH $\Pi_{3/2}$–$\Pi_{3/2}\,\frac{5}{2}^{+}$–$\frac{3}{2}^{-}$. *Middle:* Stacked OH 84 μm spectrum. *Right:* Stacked OH 79 μm spectrum.

Table 5. Physical properties of the observed lines. LAMBDA data base: http://home.strw.leidenuniv.nl/~moldata/. The critical densities are calculated with a kinetic temperature of 10 000 K for collisions with electrons, and a kinetic temperature of 100 K for collisions with H_2 molecules.

Transition	Rest wavelength μm	Rest frequency GHz	Ionization energy eV (low-up)	Critical density cm^{-3} (H_2)	Critical density cm^{-3} (e)	$E_{\rm up}$ K	Ref.
[OIII]$^3P_2$–$^3P_1$	51.81	5786	35.12–54.94		3.6×10^3	441	Draine (2011)
[NIII]$^2P_{3/2}$–$^2P_{1/2}$	57.32	5229	29.60–47.45		3.0×10^3	251	Malhotra et al. (2001)
[OI]$^3P_1$–$^3P_2$	63.18	4744.8	0–13.6	$4 \times 10^5 (T/100)^{-0.34}$		227.7	Draine (2011)
[OIII]$^3P_1$–$^3P_0$	88.36	3393	35.12–54.94		5.1×10^2	163	Draine (2011)
OH $\Pi_{3/2}$–$\Pi_{3/2}\,\frac{5}{2}^{-}$–$\frac{3}{2}^{+}$	119.23	2514.32	0–4.4	$\sim 1 \times 10^8$		120.7	LAMBDA
OH $\Pi_{3/2}$–$\Pi_{3/2}\,\frac{5}{2}^{+}$–$\frac{3}{2}^{-}$	119.44	2509.95	0–4.4	$\sim 1 \times 10^8$		120.5	LAMBDA
[NII]$^3P_2$–$^3P_1$	121.90	2459.4	14.53–29.6		3.1×10^2	188.1	Draine (2011)
[OI]$^3P_0$–$^3P_1$	145.53	2060.1	0–13.6	$8 \times 10^4 (T/100)^{-0.34}$		326.6	Draine (2011)
[CII]$^2P_{3/2}$–$^2P_{1/2}$	157.74	1900.4	11.26–24.4	3×10^3	50	91.2	Malhotra et al. (2001)
[NII]$^3P_1$–$^3P_0$	205.18	1461.1	14.53–29.6		44	70.1	Draine (2011)

carbon ionization front upon metallicity (e.g. Croxall et al. 2017) and the optical depths of the lines, in particular $\tau_{[\mathrm{O\,I}]\,63\,\mu\mathrm{m}} \sim 1$–3 (e.g. Liseau, Justtanont & Tielens 2006; Hughes et al. 2015). The [O III] and [N II] lines come only from the ionized gas phase – the [N II] lines originate from both diffuse and dense H II gas phases – offering an excellent estimate of the total mass of ionized gas (e.g. Liseau et al. 2006; Zhao et al. 2016a; Zhao, Yan & Tsai 2016b). With similar critical densities, but different ionization potentials, the ratio [OIII] 88 μm/[N II] 122 μm provides a good tracer of the stellar effective temperature of the ionizing source.

7.1 Ionized gas mass

The extreme starburst conditions in the SMG sample supplies enormous amount of heating power to ionize neutral gas, mostly due to the feedback of star formation through UV radiation, X-rays, outflows, and shocks, etc. It has been claimed that some high-redshift starburst galaxies have very high mass ratios between ionized gas and molecular gas, $M(\mathrm{H^+})/M(\mathrm{H_2}) \gtrsim 10$–20 per cent, in SMMJ02399 and Cloverleaf (Ferkinhoff et al. 2011), by calculating the minimum ionized gas mass, $M^{\mathrm{min}}_{\mathrm{H^+}}$, traced by the [N II] and [O III] lines. Following the method used in Ferkinhoff et al. (2010, 2011), we assume that nitrogen in H II regions is singly ionized and the [NII] emission could represent all the diffuse low-density ionized gas, neglecting other energy levels (e.g. [NIII] or [O II], [O V] and higher). The minimum ionized gas mass can be estimated from

$$M^{\mathrm{min}}_{\mathrm{H^+}} = F_{\mathrm{line}} \cdot \frac{4\pi \cdot D_{\mathrm{L}}^2 \cdot m_{\mathrm{H}}}{g_{\mathrm{upper}}/g_{\mathrm{tot}} A_{\mathrm{ul}} h \nu_{\mathrm{line}} X_{\mathrm{line}}}, \quad (6)$$

where F_{line} is the line flux in Jy km s^{-1}, D_{L} is the luminosity distance in Mpc, m_{H} is the mass of a hydrogen atom, A_{ul} is the Einstein spontaneous A coefficient, g_{upper} is the statistic weighting of the upper energy level (=3 for [N II] 122 μm and [O III] 88 μm lines), $g_{\mathrm{tot}} (= \Sigma g_i \exp(-\Delta E_i/kT))$ is the partition function, h is the Planck constant, ν_{line} is the rest frequency of the emission line and X_{line} is the relative abundance of the studied ionized atoms (N or O) relative to ionized hydrogen ($\mathrm{H^+}$). For the minimum mass estimate, we assume that $X_{\mathrm{N_{II}}} = \mathrm{N/H}$, $X_{\mathrm{O_{III}}} = \mathrm{O/H}$, and we adopt the relative abundances (comparing to H) of N and O to be 9.3×10^{-5} and 5.9×10^{-4} (i.e. the H II region abundances in Savage & Sembach 1996).

We calculate $M^{\mathrm{min}}_{\mathrm{H^+}}$ using the [N II] 122 μm, [OIII] 88 μm, and [OIII] 52 μm lines for both kinds of stacked spectrum and list them in Table 6. We find that $M^{\mathrm{min}}_{\mathrm{H^+}}$ derived using only the [O III] 88 μm lines are about 12–13 per cent of those derived using the [N II] lines, likely because the [O III] 88 μm lines trace highly ionized gas and the [NII] lines probe almost all phases of $\mathrm{H^+}$, including the diffuse phase as well as gas ionized by less energetic UV photons. Similarly the $M^{\mathrm{min}}_{\mathrm{H^+}}$ derived using [O III] 52 μm lines are 20–30per cent of that derived using [OIII] 88 μm, likely due to the much higher critical density of [O III] 52 μm, which is almost solely contributed by the dense gas phase ($n_{\mathrm{e}} > 10^3$ cm^{-3}).

We derive a $M^{\mathrm{min}}_{\mathrm{H^+}}$ of $\sim 7.4 \pm 1.5 \times 10^8\,\mathrm{M}_\odot$ for the intrinsic stacked spectrum and $180 \pm 25/\mu \times 10^8\,\mathrm{M}_\odot$ for the scaled spectral stack. The relative ratio between the [O III]-derived $M^{\mathrm{min}}_{\mathrm{H^+}}$ and the [N II]-derived $M^{\mathrm{min}}_{\mathrm{H^+}}$ are similar for the two different stacked spectra. We list their $M^{\mathrm{min}}_{\mathrm{H^+}}$ values in Table 6.

7.2 [N II] lines

The two lines of [N II] are particular interesting since they are excited solely in ionized gas (HII) given their ionization potential of 14.53 eV, i.e. a value just above the ionization energy of hydrogen, 13.6 eV, which indicates that they are potentially related to star-forming activity. Both lines have relatively low critical densities (44 cm^{-3} for [N II] 205 μm and 300 cm^{-3} for [N II] 122 μm, see Table 5), meaning they are easily excited in the diffuse ionized ISM. Both lines are normally optically thin at FIR wavelengths, even for high column densities and extreme conditions (e.g. Goldsmith et al. 2015). Given their long wavelengths, they are much less affected by dust extinction compared to their optical/NIR transitions. As such, these lines are independent extinction-free indicators of the current SFR (e.g. Zhao et al. 2013).

Both [N II] lines lie at high frequencies that are inaccessible from ground-based telescopes. Only FIR space telescope missions (e.g. *ISO* and *Herschel*) could detect the line in the Milky Way and some local galaxies (e.g. Wright et al. 1991; Goldsmith et al. 2015; Herrera-Camus et al. 2016; Zhao et al. 2016a; Croxall et al. 2017). The [N II] lines, especially the [N II] 205 μm line, are found to be usually 10–50× weaker than the [CII] 158 μm line, making it difficult to detect from redshifted galaxies. After some early searches in the distant Universe (e.g. Ivison & Harrison 1996), ALMA has begun to observe these lines in high-redshift galaxies (e.g. Ferkinhoff et al. 2015; Pavesi et al. 2016). Self-absorption may also play a role in the [N II] line ratio, which will be discussed in Section 8.3.

In Fig. 12, we plot the theoretical line ratio between the [N II] 122 μm and [N II] 205 μm lines ($R_{122/205}$) following Rubin (1985) and (Draine 2011). We find that the minimum value of $R_{122/205}$ is around unity at relatively low electron densities ($\sim$1–10 cm^{-3}); at high electron densities ($\gtrsim 10^{4-5}$ cm^{-3}), $R_{122/205}$ saturates at around 10. We present $R_{122/205}$ models for three electron temperatures (T_{e} = 5000, 10 000, and 30 000 K) in Fig. 12, showing $R_{122/205}$ as a monotonically increasing function of electron density for each temperature. $R_{122/205}$ is not sensitive to T_{e}, but is very sensitive to n_{e}. Clearly, this makes the $R_{122/205}$ ratio an excellent tracer of n_{e}, with little degeneracy in T_{e}. Furthermore, the ratio of $R_{122/205}$ seems sensitive across a wide range of n_{e} between 10 and 10^4 cm^{-3}.

We overplot a few representative data points measured from the same far-IR [N II] pair from the literature, trying to compare different n_{e} results obtained using the same tracer. In our Milky Way, an average n_{e} of 22 cm^{-3} was found using observations made by the *Cosmic Background Explorer* (Wright et al. 1991; Bennett et al. 1994). Using *Herschel*, Goldsmith et al. (2015) observed [N II] lines along roughly 100 sightlines across the Galactic disc, mostly close to the inner parts of our Galaxy (±50° of Galactic longitude), and they found most to have n_{e} between 10 and 100 cm^{-3}(see their fig. 19). In Fig. 12, the average conditions of the warm ionized medium (WIM) are plotted as a grey box in the bottom-left corner. The electron density of the WIM is quite uncertain, and is often taken to be $\sim$0.01–0.1 cm^{-3} (e.g. Taylor & Cordes 1993; Persson et al. 2014; Goldsmith et al. 2015). Heiles, Reach & Koo (1996) found a low volume filling factor and a relatively high n_{e} of 5 cm^{-3}, using 1.4 GHz radio recombination lines in the Galactic plane. In our plot we set this value as the highest plausible n_{e} value for the WIM, and use an arrow showing that it might also be much lower than the grey box.

We also plot the n_{e} range measured in NGC 891 (Hughes et al. 2015), as the representative value found for nearby quiescent spirals and in the Milky Way (Goldsmith et al. 2015). A similar n_{e} range has been found in the starburst region, 30 Doradus, in the Large Magellanic Cloud (LMC; Chevance et al. 2016). For local normal galaxies (e.g. Herrera-Camus et al. 2016) and LIRGs (e.g. Zhao

Table 6. Measured line properties in the stacked spectra. $M_{\rm H^+}^{\rm min}$ is the estimated minimum ionized gas mass calculated from [NII] 122 μm and [O III] 88 μm lines, following the method used in Ferkinhoff et al. (2010). μ is the stacked amplification factor for each line, which ranges about 15–30, depending on the specific line and weighting adopted (see Section 6.1).

Transitions	$L^{\rm intrin}$	$M_{\rm H^+}^{\rm min}$	$L^{\rm scale}$	$\mu M_{\rm H^+}^{\rm min}$
Unit	10^9 L$_\odot$	10^8 M$_\odot$	10^9 L$_\odot$	10^8 M$_\odot$
[O III] 52 μm	14 ± 2	0.36 ± 0.1	200 ± 25	5 ± 1.4
[O I] 63 μm	1.7 ± 0.3		79 ± 8	
[O III] 88 μm	3.3 ± 0.3	0.9 ± 0.1	87 ± 5	24 ± 1.4
OH 119 μm[a]	-2.9 ± 0.6		-66 ± 8	
[N II] 122 μm	1.5 ± 0.3	7.4 ± 1.5	36 ± 5	180 ± 25
[C II] 158 μm	7.6 ± 0.2		216 ± 4	
[N II] 205 μm	<0.9		<18	

[a] The OH flux is combined from two velocity components.

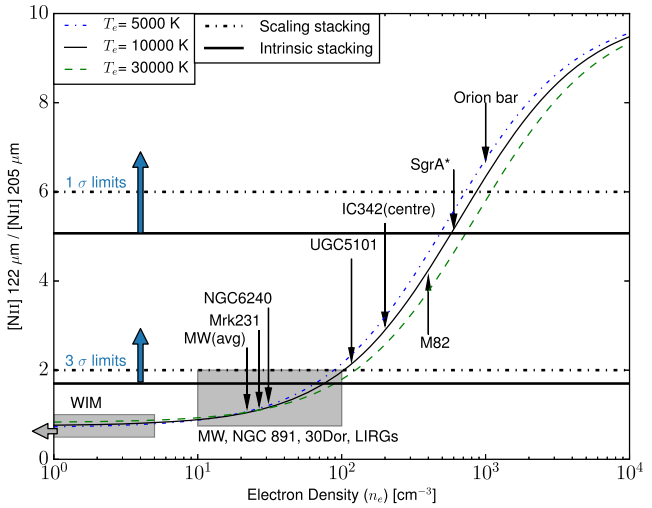

Figure 12. Theoretical line luminosity (in L$_\odot$) ratio between the [N II] 122 μm and [N II] 205 μm lines ($R_{122/205}$) as a function of electron density ($n_{\rm e}$), following Rubin (1985) and (Draine 2011). We present $R_{122/205}$ models for electron temperatures $T_{\rm e} = 5\,000$ K (blue dotted), 10 000 K (black solid), and 30 000 K (green dashed). The thick solid and dash–dotted lines show the 1σ and 3σ lower limits of the observed line ratios of $R_{122/205}$, derived from intrinsic stacking and scaling stacking, respectively. We also overplot typical ranges of $n_{\rm e}$ measured with the same $R_{122/205}$, in the discs of nearby galaxies, in the central regions of galaxies, in the Galactic Centre, and for a few Galactic HII regions.

et al. 2016a; Díaz-Santos et al. 2017) most $n_{\rm e}$ values range between 10 and 100 cm^{-3}, too. For most local ULIRGs, although higher SFR densities are expected, they lie in the same region as spiral galaxies with the maximum, $n_{\rm e} \sim 120$ cm^{-3} found in UGC 05101 (Spinoglio et al. 2015) via [N II] lines. Higher $n_{\rm e}$ values have also been found in a few spatially resolved regions in our Galaxy and in some nearby starburst regions. In the central regions of IC 342 (Rigopoulou et al. 2013) and M 82 (Petuchowski et al. 1994), $n_{\rm e}$ values are much higher than the average for the discs. Interestingly, the $n_{\rm e}$ measured in Sgr A* (Goicoechea et al. 2013) and the ionizing peak of the Orion bar (Bernard-Salas et al. 2012) show the highest values, indicating high-density H II regions compared to the lower densities found to represent the average conditions in galaxies.

Unfortunately, our stacked spectra only give an upper limit for the [N II] 205 μm line flux, so we can provide only a lower limit for $R_{122/205}(>2$, for a 3σ limit), which corresponds to an $n_{\rm e}$ of >100 cm^{-3}, i.e. considerably higher than the global average conditions of most local star-forming galaxies. In Section 6.2, we find an average intrinsic IR colour of $S_{70}/S_{100} \sim 0.8$, which corresponds to $\sim$1.15 in $\nu\, S_{70}/\nu\, S_{100}$. Our $n_{\rm e}$ limit is roughly consistent with the correlation found between $\nu\, S_{70}/\nu\, S_{100}$ and $n_{\rm e}$ by Herrera-Camus et al. (2016). Derived from equation (6) in Herrera-Camus et al. (2016), $n_{\rm e}$ is $\sim$90 cm^{-3}, which lies at the high end of their galaxy sample, and has a wide dynamical range of $n_{\rm e}$ and $R_{122/205}$ for comparison. Most local star-forming galaxies, active star-forming regions in the LMC (e.g. 30 Dor), normal spirals (e.g. NGC 891), LIRGs and ULIRGs (e.g. Mrk 231 and NGC 6240), have a global average $n_{\rm e}$ between 10 cm^{-3} and 100 cm^{-3}, and show no obvious relations with the global SFR, or $L_{\rm IR}$. The high $n_{\rm e}$ found for our stacked DSFG spectrum indicates higher pressure conditions for the ionized gas in their star formation regions, more like M 82, SgrA*, IC 342 centre, and that found in the Orion bar. On the other hand, the electron temperature is not expected to change dramatically (see also Section 7.5), so higher $n_{\rm e}$ values indicate higher pressures of the ionized gas phase.

In our Milky Way, younger H II regions (hyper-compact H II and ultra-compact H II, UCH II) are found to have higher $n_{\rm e}$ (e.g. Churchwell 2002), however the high $n_{\rm e}$ likely cannot be attributed to the age of the H II regions because the typical lifetime of an UCH II region is only $\sim 10^5$ yr, too brief to play an important role here. Moreover, the extremely high SFRs found in DSFGs produces a prodigious flux of cosmic rays, $\sim$100–1000$\times$ the Galactic value, which efficiently heats up the dense cores that are protected by the dust from UV photons, thereby increasing the Jeans mass of the dense cores (e.g. Papadopoulos 2010). The most massive dense cores can maintain their pressure via self-gravity, helping to confine H II to relatively small regions, such that the average $n_{\rm e}$ is systematically higher.

7.3 [O III] lines

The [O III] 88 and 52μm lines are important coolants of the ionized phase of ISM in DSFGs because of the high abundance of oxygen. The ionization potential of [OIII] is 35.12 eV, which corresponds to very energetic physical conditions, e.g. the UV radiation from very hot massive stars (O and B stars), X-rays or shocks (e.g. Stasińska et al. 2015). As with the [N II] lines, [O III] line ratios are not sensitive to the electron temperature. The critical densities of the [O III] 88 and 52μm transitions are $\sim$500 and 3600 cm^{-3}, respectively, making them a sensitive probe of $n_{\rm e}$ in relatively dense H II regions.

In Fig. 13, we plot the theoretical line ratio of the [O III] 52 and 88μm ($R_{52/88}$) lines, following Rubin (1985). The range where these lines are relatively sensitive to electron density is between 10^2 and 10^5 cm^{-3}, corresponding to line ratios, $R_{52/88}$, of $\sim$0.7 and $\sim$10,

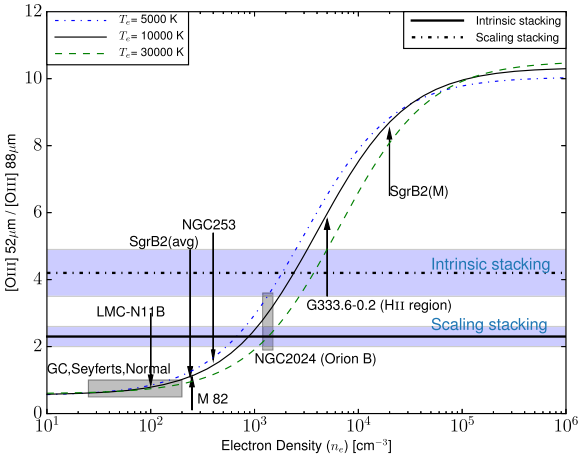

Figure 13. Theoretical line luminosity (in $L_\odot$) ratio between the [O III] 52 μm and [O III] 88 μm lines ($R_{52/88}$), as a function of n_e, following Rubin (1985). We present $R_{52/88}$ models for electron temperatures, T_e = 5 000 K (blue dotted line), 10 000 K (black solid line), and 30 000 K (green dashed line). The thick solid line and dash–dotted line show the observed $R_{52/88}$ ratios derived from intrinsic stacking and scaling stacking, respectively. The blue shadow regions show the 1σ error bar of the observed ratios. We also overplot typical ranges of n_e found in the discs of nearby normal galaxies, the LMC, the central regions of our Galaxy, and a few Galactic HII regions.

respectively. Similar to Fig. 12, we plot $R_{52/88}$ with n_e of 5000, 10 000, and 30 000 K, which shows that $R_{52/88}$ is not sensitive to T_e.

The [O III] 52 and 88 μm transitions have been observed from both Galactic targets and external galaxies. The grey box in the bottom left corner of Fig. 13 shows the n_e range measured with the same [O III] pair in the central region of the Milky Way (i.e. Rodríguez-Fernández & Martín-Pintado 2005), nearby Seyfert galaxies (e.g. Spinoglio et al. 2015) and normal galaxies (e.g. Negishi et al. 2001). These values are consistent with the n_e range measured from the [N II] lines, though [O III] lines are not very sensitive to n_e below a few hundred cm^{-3}. We also label the measured $R_{52/88}$ in the centres of a few typical nearby star-forming galaxies (e.g. M 82, NGC 253; see Duffy et al. 1987; Carral et al. 1994) and the average $R_{52/88}$ measured in Sgr B2 (Goicoechea, Rodríguez-Fernández & Cernicharo 2004), which are somewhat higher than the average value measured in galaxies as a whole. This indicates a higher average n_e in the centre of galaxies, consistent with the trend found in M 51 and NGC 4449 using optical observations (e.g. Gutiérrez & Beckman 2010).

We also overplot the $R_{52/88}$ values found in Galactic sources, including the range found in the H II regions of NGC 2024 (Orion B Giannini et al. 2000), G333.6−0.2 (Colgan et al. 1993), and Sgr B2(M) (Goicoechea et al. 2004). These targets show the highest n_e, especially Sgr B2(M) where several ultra-compact H II regions reside in a very small volume.

In Section 7.2, we estimated n_e using [N II] 122 μm and the upper limit from [N II] 205 μm, finding that the n_e found in our DSFGs is higher than 100 cm^{-3}. From the $M_{H^+}^{min}$ and n_e derived from [O III] lines, at least 10 per cent of the ionized gas has a very high n_e, ∼10^3–10^4 cm^{-3}. The n_e derived from [N II] and [O III] are both higher than the densities found in local star-forming galaxies (e.g. 30 cm^{-3}Herrera-Camus et al. 2016, see also Figs 12 and 13), where the derived n_e values are consistent with measurements using optical lines (e.g. Zaritsky, Kennicutt & Huchra 1994).

More recent evidence from optical and near-IR studies suggest that n_e in star-forming galaxies at $z \sim 2$ seem to be systematically higher than in local star-forming galaxies, by up to two orders of magnitude (e.g. Bian et al. 2016; Sanders et al. 2016). These studies find a median n_e of ∼250 cm^{-3}, consistent with our lower limit for n_e from the [N II] lines, indicating an increase of n_e with redshift for both normal star-forming galaxies and DSFGs.

As revealed in resolved studies of nearby galaxies, n_e tends to be higher in the centres of galaxies, likely due to the strength of the radiation field and the density of the local ISM (e.g. Herrera-Camus et al. 2016). High-redshift DSFGs may have both a higher radiation field, revealed by the [O III] to [N II] ratio, and a denser ISM, which confines the expansion of H II regions and keeps n_e relatively high. However, optical measurements in both galaxy populations from the Sloan Digital Sky Survey (SDSS) and local analogues of high-redshift star-forming galaxies find that those with higher SFR surface densities (Σ_{SFR}) tend to have lower n_e (Bian et al. 2016); this is not consistent with far-IR [N II] results, which show a tight correlation between Σ_{SFR} and n_e (Herrera-Camus et al. 2016).

7.4 [C II] emission from ionized gas

To trace the origins of the [C II] 158 μm emission, it is important to separate between the [C II] luminosity fraction contributed by the neutral gas and that contributed by the ionized gas. The fraction from ionized gas is normally small ∼20–40 per cent (Croxall et al. 2017), but is not negligible, especially given the uncertainty in the C/N abundance ratios. The [C II]/[N II] line ratio is sensitive to the ionized gas fraction that contributes the [CII] emission, because [N II] lines come only from the ionized gas, and should pick up the majority of it, given their low critical densities.

In the ionized gas phase, both the [N II] and [C II] lines are excited by collisions with electrons, and neither line is sensitive to electron temperature. Using the line ratio between [N II] lines and [C II] 158 μm, one can probe the contribution to the observed [C II] intensity from the ionized gas phase with little dependence on n_e and T_e (e.g. Oberst et al. 2006, 2011; Hughes et al. 2015; Pavesi et al. 2016).

Although the [N II] 122 μm line has a higher critical density (∼300 cm^{-3}) than that of the [C II] line, the ratio dependence on the electron density can be well modelled. We can use the upper limit of n_e derived from the two [N II] lines to set a further constraint. In Fig. 14, we plot the theoretical line ratio between [C II] 158 μm and [N II] 122 μm in the ionized gas phase. The observed [C II]/[N II] ratios include [C II] emission with contribution from neutral gas phase, so the ratio is always above the theoretical curves (for the ionized gas phase only). The line ratio of [C II] 158 μm to [N II] 122 μm does depend on n_e. However, if the electron density is higher than a few hundred cm^{-3} (well above the critical densities of both lines), both the [N II] 122 μm and the [C II] 158 μm lines will be excited efficiently. For the abundances of N/H and C/H, we adopt 7.76 × 10^{-5} and 3.98 × 10^{-4}, respectively – typical H II region values(Savage & Sembach 1996). Because the [C II]/[N II] ratio is sensitive to abundances, we overplot the ratio using typical Galactic abundances found in diffuse clouds (7.94 × 10^{-5} for N; 1.38 × 10^{-4} for C – Savage & Sembach 1996) for comparison, and to present the uncertainty. More detailed discussion on the abundances will be presented in Section 8.4.

We plot the [C II] 158 μm/[N II] 122 μm line ratio curves at T_e= 5000, 10 000, and 30 000 K, which are consistent with each other, showing that these ratios are not sensitive to the electron temperature. The [CII] 158 μm/[N II] 122 μm ratio has a stronger dependence on the electron density, which can be constrained from the line ratio of the two [NII] lines. All line ratios decrease monoton-

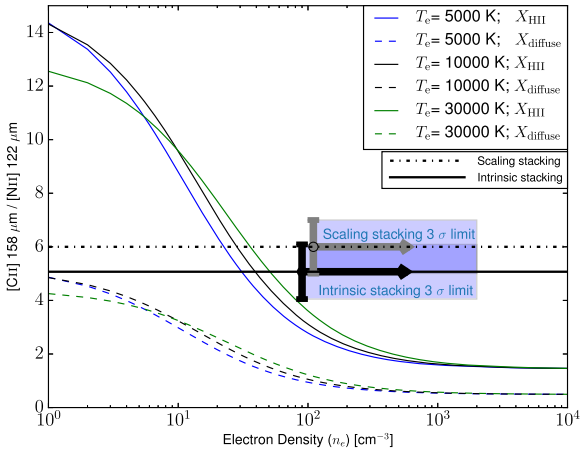

Figure 14. Theoretical line luminosity (in $L_\odot$) ratio of [C II] 158 μm and [N II] 122 μm as a function of electron density. This calculation considers the [C II] 158 μm emission that is excited by collisions with electrons only. We plot the [C II] 158 μm/[N II] 122 μm line ratios for 5000 K (blue), 10 000 K (black), and 30 000 K (green). Solid curves show the ratio using the carbon and nitrogen abundances measured in Galactic HII regions; dashed curves show the ratio with abundances in diffuse gas (e.g. Savage & Sembach 1996). The observed ratios between [C II] 158 μm and [N II] 122 μm in our stacked DSFG spectrum are plotted as thick black line and dash–dotted line, for intrinsic stacking and scaling stacking, respectively. The blue shadow regions show the 1σ error bar of the observed [CII] 158 μm/[NII] 122 μm ratios. The two arrows in the x-axis show the lower 3σ limits of electron density derived from $R_{122/205}$ ratios derived from the two stacking methods. The maximum allowed electron density is 2000 cm^{-3}, which is the n_e derived from [O III] lines.

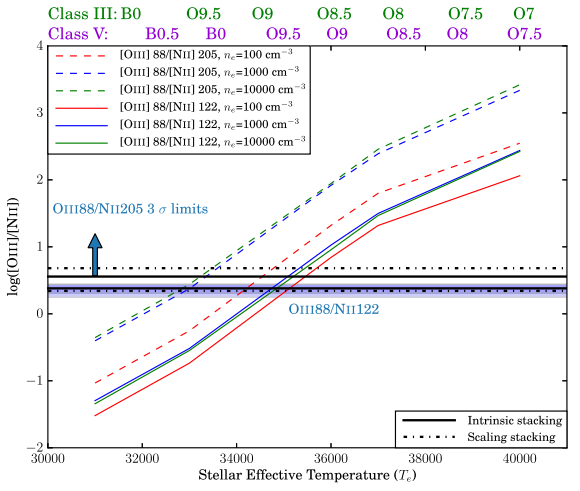

Figure 15. Theoretical line luminosity (in $L_\odot$) ratio of [O III] 88 μm and the [N II] lines as a function of the effective stellar temperature, derived from the Rubin (1985) H II models. We plot the observed [O III] 88 μm to [N II] 122 μm ratios and the upper limits of the observed [O III] 88 μm to [N II] 205 μm ratios, derived from for intrinsic stacking (black thick line) and scaling stacking (dash–dotted line), respectively. The upper axis labels show stellar types of OB stars of corresponding electron temperature for luminosity class III (Green) and luminosity class V (Purple) stars, according to the classification of Vacca et al. (1996).

ically with electron density, and saturate at the high-density end ($\geq$1000 cm^{-3}), where n_e is much higher than the critical densities of both lines.

The observed ratio of [C II] 158 μm and [N II] 122 μm in our stacked DSFG spectrum is 5.1 ± 1.0, which is plotted as the shadowed area. We find a lower limit for the electron density of 100 cm^{-3}, derived from the 3σ limit for the [N II] line ratios; the upper limit for n_e is 2000 cm^{-3}, derived using the [O III] lines, which are from the more energetic and denser H II regions. If we use the Galactic diffuse gas abundances (Savage & Sembach 1996), the contribution from ionized gas to the [CII] line is ∼10–15 per cent. However, if H II region abundances are adopted (Savage & Sembach 1996), the ionized gas could contribute up to 60 per cent of our [CII] emission. The ratios derived from the diffuse gas abundances is about 3 × less than those derived from abundances in H II regions. If an electron density of 100 cm^{-3} and an electron temperature of 10 000 K are assumed; this contribution drops to 30–40 per cent for an n_e of 1000 cm^{-3}.

7.5 Radiation field

The [N II] 122 μm and [O III] 88 μm lines have similar critical densities ∼300–500 cm^{-3}, but their ionization potentials differ by ×2 from 14.5 to 35 eV. Both lines are normally optically thin, and are insensitive to the electron temperature. Their ratio is sensitive only to the abundance and radiation field, which is mainly controlled by the relative fraction of UV photons at different energies (e.g. Ferkinhoff et al. 2011).

Following Ferkinhoff et al. (2011), we can probe the stellar effective temperature using the ratio between the [N II] 122 μm and [O III] 88 μm lines in our stacked DSFG spectrum. We adopt the H II region models calculated by Rubin (1985), who derived the theoretical intensities of the ionized lines with different metal abundances, electron densities and stellar effective temperatures. Model 'K' in Rubin (1985) has elemental abundances close to the values in Galactic H II regions (e.g. Savage & Sembach 1996). The line intensity is proportional to abundance for optically thin lines, so we correct the line ratio map with the Galactic H II region abundances (Savage & Sembach 1996, see also Section 7.4), to provide a more consistent and realistic comparison. With the H II region abundances, the [O III]/[N II] ratio is about 1.15 × higher than those in Rubin (1985) – this does not influence our conclusions. The ratios between [O III] 88 μm and [N II] 122 μm from both our stacking methods are ∼2.2 ± 0.5 (intrinsic stacking) and 2.4 ± 0.3 (scaling stacking), fully consistent with each other. These values correspond to a stellar effective temperature of ∼35 000 K, which corresponds to O8–O9 stars, according to Vacca, Garmany & Shull (1996). These values are less than that obtained from the resolved compact starburst centre in a local ULIRG, Arp299, but are more consistent with the resolved results in most local LIRGs and AGN hosts on (sub-)kpc scales(Herrera-Camus et al. 2018a,b).

However, the global ratio of [N II]/[O III] is not just affected by abundances and the hardness of the radiation fields, but also sensitive to variation in the filling factors of the observing beam. The lower ionization potential of [NII] makes it expected to be more extended than the [O III] 88 μm line. Only O stars can emit powerful UV photons to excite this line. This means that our [N II] emission is contributed from both O stars and B stars. On the other hand, [N II] lines have a very low critical densities, so its collisional excitation saturates in H II regions well before [O III] lines. If we zoom into smaller [O III] emitting regions, the [O III]/[N II] ratio would be higher than that obtained from global average. The combination

of the two leads to [N II] dominating the extended, diffuse, ionized gas. So, our derived stellar effective temperature is actually a lower limit for that in the dense H II regions with [O III] emission.

To generate the observed [N II] 122-μm emission, $\sim 3 \times 10^7$ or $\sim 5 \times 10^7$ O8 or O9 stars are needed, respectively, assuming an n_e of 1000 cm^{-3} in the Rubin (1985) model. From the same models we can also derive the ionized gas mass from the [NII]122μm emission. We find that different values of n_e give similar ionized gas masses (intrinsic), ranging between 1 and 2×10^9 M$_\odot$, consistent with the $M_{H^+}^{min}$ derived in the previous section. This is about 10 × less than that estimated for SMM J2135−0102 by Ferkinhoff et al. (2011). However, for the galaxies with CO detections, the H_2 gas mass ranges from 1×10^{11} to 5×10^{11} M$_\odot$. The ionized gas mass fraction is estimated to be less than 2 per cent of the molecular gas mass, assuming an α_{CO} conversion factor of 0.8 (typical value for ULIRGs Bolatto, Wolfire & Leroy 2013). This is consistent with the ionized gas fraction found in local galaxies (e.g. Brauher, Dale & Helou 2008; Ferkinhoff et al. 2011), but much less than the fractions found in two high-redshift DSFGs (35 per cent for Cloverleaf quasar and 16 per cent for SMM J2135−0102; Ferkinhoff et al. 2011). On the other hand, active galactic nuclei (AGNs) can increase the UV radiation and bias the hardness of the radiation field (e.g. Groves, Dopita & Sutherland 2004), which shows that a high [O III]/[N II] ratio can be easily achieved in the high-pressure narrow-line region of AGNs.

Using the [Si II] 34 μm and [S III] 33 μm lines in the stacked PACS spectra for a similar sample of high-redshift lensed starbursts, Wardlow et al. (2017) found that SMGs on average contain AGNs, followed the method proposed by Dale et al. (2006, 2009). However, statistical studies based on X-rays and MIR spectroscopy studies find that the fraction of DSFGs harbouring powerful AGN is small, thus they are unlikely to dominate the gas heating (e.g. Alexander et al. 2005; Coppin et al. 2010; Wang et al. 2013b). On the other hand, in the stacked PACS spectrum Wardlow et al. (2017) found non-detection for [O IV], which is expected to arise from AGNs due to the high ionization potential. Thus, we conclude that the AGN contamination to the far-IR lines should be negligible for our stacked results.

7.6 [O I] lines

We detect [O I] 63 μm emission in our stacked spectrum, with an upper limit for the [O I] 145 μm transition. These two lines have identical energy potentials for further ionization, but they have different upper level energies, $\Delta E/k$, of 228 and 327 K above the ground state. The critical densities of the 145 and 63μm transitions are $\sim 10^4$ and $\sim 10^5$ cm^{-3}, respectively, so both lines are sensitive to dense and warm neutral gas. Their line ratio is a powerful diagnostic of the density and temperature of the emitting regions, under the optically thin assumption (e.g. Tielens & Hollenbach 1985; Liseau et al. 2006). The heating of [OI] lines could be powered by radiative shocks (e.g. Hollenbach & McKee 1989; Draine & McKee 1993) or FUV photons from massive stars, given the high SFRs of these galaxies.

Given the non-detection of the [O I] 145 μm transition, we can get an upper limit for the ratio of [O I] 63/145 > 6 (1σ) or >1.3 (3σ). These exclude a cold (<50 K) and optically thick scenario (see e.g. fig. 4 of Liseau et al. 2006). If [O I] 63 μm is indeed optically thin, then the [O I] 145 μm emission is expected to be even further below our detection limit.

If the [O I] 63 μm emission is dominated by dissociative shocks, its intensity is proportional to the mass-loss rate, which is caused by the dominance of the cooling via [O I] 63 μm (Hollenbach & McKee 1989; Draine & McKee 1993). However, the excitation from PDRs is another strong power source for [O I] lines. The [C II]158 μm/[O I]63 μm luminosity ratio provides a way to discriminate between PDRs and shocks: this ratio is generally ≤10 in PDRs and ≥10 in shock-dominated regions (Hollenbach & McKee 1989). Our stacked DSFG spectrum shows [O I]63 μm/[C II]158 μm ∼4, on the high end of the resolved local starburst regions or AGN centres, and much higher than the values measured in normal galactic discs (Herrera-Camus et al. 2018a). Our global average ratios indicate that the [O I] emission must have some contribution from shocks. but shock is also not dominant. Moreover, the [O I] 63 μm emission often suffers from self-absorption effects (see Section 8.3), which has been seen both in the Milky Way molecular clouds (e.g. Ossenkopf et al. 2015), and in local starbursts (Luhman et al. 2003; Rosenberg et al. 2015). If the [O I] self-absorption also plays a role, the intrinsic ratio of [O I]63 μm/[C II]158 μm should be even higher.

8 CAVEATS

8.1 Statistics in the line ratios

In this paper, we have stacked *Herschel* SPIRE FTS spectra and derived the average physical conditions of the fine-structure lines using their relative ratios. We have to note that the average of ratios (e.g. <[NII] 205 μm/[NII] 122 μm>) are not necessarily the same as the ratio of the averages <[NII] 205 μm>/<[NII] 122 μm>, which introduces an extra uncertainty in the statistics (e.g. Brown 2011).

For most lines, we do not have individual detections of the lines in the SPIRE spectra, so it is not possible to directly measure individual line ratio and get the average. Although a ratio of line flux averages (observational constraint) might be similar to an average of ratios (physical condition), the expectation – the average of the ratio – would always be larger than the ratio of the averages. Thus, our line ratios from stacked spectra are underestimated (Brown 2011). The derived n_e and radiation hardness are likely more extreme than those we derived. Furthermore, this speculation is especially true when the undetected lines are upweighted when adopting average weighted by noise levels.

8.2 Biases in stacking

We have stacked a sample of ∼40 galaxies at a redshift range between 1.5 and 3.6. The *Herschel* SPIRE FTS has a fixed observing frequency range so the final line coverage is not uniform. Thus, the stacked averaged lines are actually from different galaxies, which makes another potential bias to the final line ratios. This effect is obvious at both the low- and high-frequency ends, especially for the [O III] 52 μm and [O I] 63 μm lines, which are more contributed by galaxies at higher redshifts. Moreover, the spectra are noisier in the band edges, which makes the S/N even lower for these lines.

Our first two stacking methods (intrinsic luminosity and scaling to Eyelash) both adopt weights of $1/\sigma^2$, which preferentially weight galaxies with better S/N levels (Eyelash) and smaller redshifts. The intrinsic luminosity weighting is relatively more biased to higher S/N targets, whilst the scaling method is more biased to higher luminosity targets. Although a straight (equally weighted) stacking could avoid weighting biases, such stacking will be highly dominated by non-Gaussian noises, especially the edges of both bands that cover across the whole frequency range. A median stacking of the L_{IR} normalized spectra is less biased by galaxy properties,

and it can test if some weak features are common for the sample, e.g. the OH 119μm absorption line. However, the median stacked spectrum is noisier and seems still contaminated by the noisy edges of individual band. This method also does not allow to calculate median of the dust continuum or $L_{\rm IR}$ using the same weighting from spectral line stacking.

8.3 Absorptions to the fine-structure lines

During our analysis, we accounted for the integrated line luminosities and neglected self-absorptions. This might be severe for the [O I] lines, which have been found in various Galactic and extragalactic conditions (Fischer et al. 1999; Liseau et al. 2006; González-Alfonso et al. 2012; Fischer et al. 2014). The [C II] 158 μm line also often shows self-absorption features in Galactic studies (e.g. Gerin et al. 2015; Graf et al. 2012), and it might also affect extragalactic studies as well (Malhotra et al. 1997), which is very difficult to identify with limited angular resolution (Ibar et al. 2015).

We also examine the possibility of the differential self-absorption to the [N II] line pair, due to the relatively lower excitation energy of the 205 μm line compared to the 122 μm line. Following equation (3), the equivalent width ratio between the two lines are $W_{\rm eq}(205)/W_{\rm eq}(122) \sim 1.026$, indicating that their theoretical absorption depths are similar. Only a high optical depth can produce biased self-absorption to eliminate the observed [N II] 205 μm line flux. However, due to the small abundance of nitrogen, it is unlikely that the [N II] 205 μm line can be optically thick (Langer, Goldsmith & Pineda 2016). Furthermore, self-absorption has not been found in local galaxies in our Milky Way galaxy, where [C II] and [O I] have been found to have self-absorption in some cases (Gerin et al. 2015). We conclude that our high $R_{122/205}$ is unlikely to be caused by self-absorption, but more detailed observations are needed to further support this conclusion.

Another, possible contamination that may bias the line measurement is an absorption against strong background continuum emission. This has been seen in [C II] absorption in high-redshift galaxies (e.g. Nesvadba et al. 2016) against strong continuum sources powered by intense star formation or AGNs. Although this may not be a dominant bias for the fine-structure lines, such an effect could contribute very high level of 'line-deficit' (Nesvadba et al. 2016).

On the other hand, the upper energy levels of the [N II] lines are 70 and 188 K for the $^3P_1$–$^3P_0$ (205 μm) and $^3P_2$–$^3P_1$ (122 μm) lines, respectively. Therefore, the WIM component of them can be easily absorbed against background sources with high brightness temperatures. Using high-spectral-resolution observations from the HIFI instrument onboard *Herschel*, Persson et al. (2014) detected absorption features of the [N II] 205 μm lines towards a few massive Galactic star-forming regions. They found that [NII] emission from ionized gas in the dense and hot HII regions is likely absorbed by widespread low-density and relatively low-temperature WIM gas in the foreground.

Because the upper level temperature of [N II] 205 μm is relatively lower than that of [N II] 122 μm, the former is easily to get absorbed. The $R_{122/205}$ ratio obtained from global volume average observations can be biased by the differential absorptions, and may further bias the final derived $n_{\rm e}$ to lower values (suggestive of more diffuse gas) and this has possibly already influenced observational results in local galaxies (e.g. Herrera-Camus et al. 2016; Zhao et al. 2016a). Observations at high-angular and high-spatial resolution of the [N II] lines are needed to avoid the confusion from the absorption of the [N II] line in low-density gas and any WIM contribution.

We have neglected the optical depth of dust throughout this study. Dust can have non-negligible optical depths at mid- to far-IR wavelengths, especially for the compact starbursts, e.g. Arp220 has an optical depth of ∼1 even at the 3 mm band (Scoville et al. 2017), i.e. it is optically thick at far-IR. Lutz et al. (2016) found that local ULIRGs generally have compact sizes and their optical depths in the FIR can be close to optically thick on average. It is difficult to estimate the accurate dust attenuation of the lines, but this effect may contribute to the line deficit over the sample (Fischer et al. 2014).

8.4 Elementary abundances

Our study adopted line ratios between different elements to derive physical conditions, e.g. [C II]/[N II] for the contribution of ionized gas, and [OIII]/[N II] for the hardness of the radiation field. These are based on the assumption of the elementary abundances, which are actually fairly uncertain, due to unclear nucleosynthesis and galactic chemical evolution processes (e.g. Matteucci 2001).

The C/N abundance ratio is still largely under debate. Based on Galactic stellar determinations for the variations with metallicity (Nieva & Przybilla 2012), Croxall et al. (2017) find a decreasing C/N abundance ratio with increasing metallicity traced by [O/H]. This is partially consistent with the results found in dwarf galaxies, which show a C/N–[O/H] curve similar to a negative parabola shape (Garnett et al. 1995). Furthermore, recent work by Peña-Guerrero et al. (2017) shows that the C/N abundance ratio linearly increases with [O/H] in starburst galaxies with top-heavy IMFs, contradictory to the findings of Croxall et al. (2017). This indicates that the primary element channel for the N production is not negligible in metal poor conditions, and this effect is more sever for the top-heavy IMF conditions, which have more massive stars to supply the primary N yields (Coziol et al. 1999; Peña-Guerrero et al. 2017). It seems that it is likely not appropriate to adopt the Galactic chemical evolution and Galactic chemical abundances to starburst galaxies, which have systematically different evolution tracks and IMFs (Zhang et al. 2018).

On the other hand, the O/N abundance ratio that adopted in the [O III]/[N II] line ratios also have large uncertainties. Using Galactic H II regions, Carigi et al. (2005) find a solo increasing trend of N/O ratio with [O/H], which is consistent with the results found using optical spectra measured from Galactic B-stars Nieva & Przybilla (2012). However, local starburst galaxies have systematically biased N/O ratios from the trend found in the Milky Way (Coziol et al. 1999). More confusingly, Contini (2017) shows that the N/O abundance ratios in gamma-ray and supernova host galaxies at $z < 4$ cannot be explained by stellar chemical evolution models calculated for starburst galaxies, nor for the Milky Way, which suggests that different evolutionary tracks need to be applied for various galaxy types and redshifts.

9 SUMMARY AND CONCLUDING REMARKS

We present *Herschel* SPIRE FTS spectroscopy and PACS photometry of a sample of 45 gravitationally lensed DSFGs at $z = 1.0$–3.6, targeting the [C II] 158μm, [NII] 205 and 122μm, [O III] 88 and 52μm, [O I] 63 and 145μm, and OH 119 μm lines. We obtained 17 individual detections of [C II] 158 μm, five detections of [O III] 88 μm, three detections of [O I] 63 μm, and three detections of OH 119 μm in absorption.

We find that the [C II]/$L_{\rm IR}$–$L_{\rm IR}$ ratio shows a deficit at high FIR luminosities, high star formation efficiency ($L_{\rm IR}/M_{\rm H_2}$) and higher

surface densities of SFRs, consistent with the trends found in local star-forming galaxies, ULIRGs, SPT sources, and high-redshift starburst galaxies found in the literature.

To determine the average conditions of the ionized gas in our high-redshift DSFG sample, we stack the SPIRE spectra using three different methods, each with a different bias. We derive physical properties of the ionized gas from the stacked spectra using unlensed intrinsic luminosity, and from the spectra scaled to a common redshift. In the stacked spectrum we detected emission lines of [CII] 158 μm, [N II] 122 μm, [O III] 88 μm, [O III] 52 μm, [O I] 63 μm, and OH in absorption at 119 μm. Median stacking has lower S/N but provides further piece of evidence for the weak line detections.

Using the [N II] 122 μm detection and the upper limit for [N II] 205 μm, we derive a lower limit for the electron density of $>100\,\mathrm{cm}^{-3}$, which is higher than the average conditions found in local star-forming galaxies and ULIRGs using the same [N II] line pair. From the [O III] 63 and 145μm detections, the electron density is found to be 10^3–$10^4\,\mathrm{cm}^{-3}$, which is one-two orders of magnitude higher than that found in local star-forming galaxies using the same [O III] lines. We also use [N II] 122 μm to derive the ionized gas contribution to [CII] 158 μm and find the fraction of ionized gas to be 10–15 per cent. If we adopt the N and C abundances found in Galactic HII regions, this fraction can be as high as 60 per cent. The [O I]/[C II] ratio indicates that the [C II] emission is likely dominated by PDRs rather than by large-scale shocks. Finally, we derived the OH column density from the OH 119 μm absorption feature, which we find likely traces outflows driven by the star formation.

The physical conditions derived for the sample seem to be systematically more extreme than for local star-forming galaxies and ULIRGs, i.e. in SFRs, in electron densities derived from both total ionized gas and dense ionized gas. We use the[NII]/[O III] ratio to derive an average radiation hardness of the sample, which indicates that the star formation is dominated by massive stars with masses higher than O8.5, modulo the potential biases from diffuse ionized gas and uncertainties in the N/O abundance ratio.

ACKNOWLEDGEMENTS

The authors are grateful to the referee for the constructive suggestions and comments. ZYZ thanks J. D. Smith, Justin Spilker for sharing data. We thank Drew Brisbin for providing machine readable forms of the H II models presented in Rubin (1985). ZYZ thanks Donatella Romano for very helpful discussion. ZYZ, RJI, LD, SM, IO, RDG, and AJRL acknowledge support from the European Research Council (ERC) in the form of Advanced Grant, 321302, COSMICISM. RDG also acknowledges an STFC studentship. YZ is supported by the National Key Research and Development Program of China (no. 2017YFA0402704), and by the National Natural Science Foundation of China (nos. 11673057 and 11420101002). CY was supported by an ESO Fellowship. IRS acknowledges support from the ERC Advanced Investigator programme DUSTYGAL 321334 and STFC (ST/P000541/1). D.R. acknowledges support from the National Science Foundation under grant number AST-1614213. LD and SM also acknowledge support from the European Research Council (ERC) in the form of Consolidator Grant, 647939, COSMICDUST. US participants in *H*-ATLAS acknowledge support from NASA through a contract from JPL. *Herschel* was an ESA space observatory with science instruments provided by European-led Principal Investigator consortia and with important participation from NASA. PACS has been developed by a consortium of institutes led by MPE (Germany) and including UVIE (Austria); KU Leuven, CSL, IMEC (Belgium); CEA, LAM (France); MPIA (Germany); INAF-IFSI/OAA/OAP/OAT, LENS, SISSA (Italy); IAC (Spain). This development has been supported by the funding agencies BMVIT (Austria), ESA-PRODEX (Belgium), CEA/CNES (France), DLR (Germany), ASI/INAF (Italy), and CICYT/MCYT (Spain). SPIRE has been developed by a consortium of institutes led by Cardiff University (UK) and including University of Lethbridge (Canada); NAOC (China); CEA, LAM (France); IFSI, University of Padua (Italy); IAC (Spain); Stockholm Observatory (Sweden); Imperial College London, RAL, UCL-MSSL, UKATC, Univ. Sussex (UK); and Caltech, JPL, NHSC, University of Colorado (USA). This development has been supported by national funding agencies: CSA (Canada); NAOC (China); CEA, CNES, CNRS (France); ASI (Italy); MCINN (Spain); SNSB (Sweden); STFC, UKSA (UK); and NASA (USA). This publication is based on data acquired with the Atacama Pathfinder Experiment (APEX). APEX is a collaboration between the Max-Planck-Institut fur Radioastronomie, the European Southern Observatory, and the Onsala Space Observatory.

REFERENCES

Abel N. P., 2006, MNRAS, 368, 1949
Abel N. P., Dudley C., Fischer J., Satyapal S., van Hoof P. A. M., 2009, ApJ, 701, 1147
Alexander D. M., Bauer F. E., Chapman S. C., Smail I., Blain A. W., Brandt W. N., Ivison R. J., 2005, ApJ, 632, 736
ALMA Partnership et al., 2015, ApJ, 808, L4
Amblard A. et al., 2010, A&A, 518, L9
Aravena M. et al., 2013, MNRAS, 433, 498
Asboth V. et al., 2016, MNRAS, 462, 1989
Bakx T. J. L. C. et al., 2018, MNRAS, 473, 1751
Becker R. H., White R. L., Helfand D. J., 1995, ApJ, 450, 559
Belitsky V. et al., 2018, A&A, 612, A23
Bendo G. J. et al., 2013, MNRAS, 433, 3062
Bennett C. L. et al., 1994, ApJ, 434, 587
Bernard-Salas J. et al., 2012, A&A, 538, A37
Bian F., Kewley L. J., Dopita M. A., Juneau S., 2016, ApJ, 822, 62
Blain A. W., Smail I., Ivison R. J., Kneib J. P., Frayer D. T., 2002, Phys. Rep., 369, 111
Bolatto A. D., Wolfire M., Leroy A. K., 2013, ARA&A, 51, 207
Borys C. et al., 2006, ApJ, 636, 134
Bothwell M. S. et al., 2013, MNRAS, 429, 3047
Brauher J. R., Dale D. A., Helou G., 2008, ApJS, 178, 280
Brown S., 2011, World Applied Programming, 1, 288
Bussmann R. S. et al., 2012, ApJ, 756, 134
Bussmann R. S. et al., 2013, ApJ, 779, 25
Bussmann R. S. et al., 2015, ApJ, 812, 43
Calanog J. A. et al., 2014, ApJ, 797, 138
Carigi L., Peimbert M., Esteban C., García-Rojas J., 2005, ApJ, 623, 213
Carlstrom J. E. et al., 2011, PASP, 123, 568
Carniani S. et al., 2013, A&A, 559, A29
Carral P., Hollenbach D. J., Lord S. D., Colgan S. W. J., Haas M. R., Rubin R. H., Erickson E. F., 1994, ApJ, 423, 223
Chapman S. C., Blain A. W., Smail I., Ivison R. J., 2005, ApJ, 622, 772
Chevance M. et al., 2016, A&A, 590, A36
Churchwell E., 2002, ARA&A, 40, 27
Colgan S. W. J., Haas M. R., Erickson E. F., Rubin R. H., Simpson J. P., Russell R. W., 1993, ApJ, 413, 237
Contini M., 2017, MNRAS, 469, 3125
Coppin K. et al., 2010, ApJ, 713, 503
Côté P. et al., 2007, ApJ, 671, 1456
Cox P. et al., 2011, ApJ, 740, 63
Coziol R., Reyes R. E. C., Considère S., Davoust E., Contini T., 1999, A&A, 345, 733
Croxall K. V. et al., 2012, ApJ, 747, 81
Croxall K. V. et al., 2017, ApJ, 845, 96
Daddi E. et al., 2007, ApJ, 670, 156

Dale D. A. et al., 2006, ApJ, 646, 161
Dale D. A. et al., 2009, ApJ, 693, 1821
Danielson A. L. R. et al., 2013, MNRAS, 436, 2793
Danielson A. L. R. et al., 2017, ApJ, 840, 78
De Breuck C. et al., 2014, A&A, 565, A59
De Looze I., Baes M., Bendo G. J., Cortese L., Fritz J., 2011, MNRAS, 416, 2712
De Looze I. et al., 2014, A&A, 568, A62
Decarli R. et al., 2014, ApJ, 782, L17
Delhaize J. et al., 2017, A&A, 602, A4
Díaz-Santos T. et al., 2013, ApJ, 774, 68
Díaz-Santos T. et al., 2014, ApJ, 788, L17
Díaz-Santos T. et al., 2016, ApJ, 816, L6
Díaz-Santos T. et al., 2017, ApJ, 846, 32
Draine B. T., 2011, Physics of the Interstellar and Intergalactic Medium. Princeton Univ. Press, Princeton, NJ
Draine B. T., McKee C. F., 1993, ARA&A, 31, 373
Duffy P. B., Erickson E. F., Haas M. R., Houck J. R., 1987, ApJ, 315, 68
Dunne L., Eales S., Edmunds M., Ivison R., Alexander P., Clements D. L., 2000, MNRAS, 315, 115
Dye S. et al., 2014, MNRAS, 440, 2013
Dye S. et al., 2015, MNRAS, 452, 2258
Eales S. et al., 2010, PASP, 122, 499
Engel H. et al., 2010, ApJ, 724, 233
Farrah D. et al., 2013, ApJ, 776, 38
Ferkinhoff C., Hailey-Dunsheath S., Nikola T., Parshley S. C., Stacey G. J., Benford D. J., Staguhn J. G., 2010, ApJ, 714, L147
Ferkinhoff C. et al., 2011, ApJ, 740, L29
Ferkinhoff C. et al., 2014, ApJ, 780, 142
Ferkinhoff C., Brisbin D., Nikola T., Stacey G. J., Sheth K., Hailey-Dunsheath S., Falgarone E., 2015, ApJ, 806, 260
Fischer J. et al., 1999, Ap&SS, 266, 91
Fischer J., Abel N. P., González-Alfonso E., Dudley C. C., Satyapal S., van Hoof P. A. M., 2014, ApJ, 795, 117
Frayer D. T., Ivison R. J., Scoville N. Z., Yun M., Evans A. S., Smail I., Blain A. W., Kneib J. P., 1998, ApJ, 506, L7
Frayer D. T. et al., 2011, ApJ, 726, L22
Fu H. et al., 2012, ApJ, 753, 134
Fu H. et al., 2013, Nature, 498, 338
Fulton T. R. et al., 2010, in Oschmann J. M., Jr., Clampin M. C., MacEwen H. A., eds, Proc. SPIE Conf. Ser. Vol. 7731, Space Telescopes and Instrumentation 2010: Optical, Infrared, and Millimeter Wave. SPIE, Bellingham, p. 773134
Fulton T. et al., 2014, Exp. Astron., 37, 381
Fulton T. et al., 2016, MNRAS, 458, 1977
Garnett D. R., Skillman E. D., Dufour R. J., Peimbert M., Torres-Peimbert S., Terlevich R., Terlevich E., Shields G. A., 1995, ApJ, 443, 64
George R. D. et al., 2013, MNRAS, 436, L99
George R. D. et al., 2014, MNRAS, 442, 1877
Gerin M. et al., 2015, A&A, 573, A30
Giannini T. et al., 2000, A&A, 358, 310
Goicoechea J. R., Cernicharo J., 2002, ApJ, 576, L77
Goicoechea J. R., Rodríguez-Fernández N. J., Cernicharo J., 2004, ApJ, 600, 214
Goicoechea J. R. et al., 2013, ApJ, 769, L13
Goldsmith P. F., Yıldız U. A., Langer W. D., Pineda J. L., 2015, ApJ, 814, 133
González-Alfonso E. et al., 2012, A&A, 541, A4
González-Alfonso E. et al., 2014, A&A, 561, A27
González-Alfonso E. et al., 2015, ApJ, 800, 69
González-Alfonso E. et al., 2017, ApJ, 836, 11
González-Nuevo J. et al., 2012, ApJ, 749, 65
Graciá-Carpio J. et al., 2011, ApJ, 728, L7
Graf U. U. et al., 2012, A&A, 542, L16
Griffin M. J. et al., 2010, A&A, 518, L3
Groves B. A., Dopita M. A., Sutherland R. S., 2004, ApJS, 153, 75
Gullberg B. et al., 2015, MNRAS, 449, 2883
Gutiérrez L., Beckman J. E., 2010, ApJ, 710, L44
Hailey-Dunsheath S., Nikola T., Stacey G. J., Oberst T. E., Parshley S. C., Benford D. J., Staguhn J. G., Tucker C. E., 2010, ApJ, 714, L162
Harris A. I. et al., 2012, ApJ, 752, 152
Heiles C., Reach W. T., Koo B.-C., 1996, ApJ, 466, 191
Herrera-Camus R. et al., 2015, ApJ, 800
Herrera-Camus R. et al., 2016, ApJ, 826, 175
Herrera-Camus R. et al., 2018a, ApJ, 861, 94
Herrera-Camus R. et al., 2018b, ApJ, 861, 95
Hezaveh Y. D., Marrone D. P., Holder G. P., 2012, ApJ, 761, 20
Hodge J. A., Carilli C. L., Walter F., de Blok W. J. G., Riechers D., Daddi E., Lentati L., 2012, ApJ, 760, 11
Hodge J. A. et al., 2016, ApJ, 833, 103
Holland W. S. et al., 2013, MNRAS, 430, 2513
Hollenbach D., McKee C. F., 1989, ApJ, 342, 306
Hopkins A. M., Beacom J. F., 2006, ApJ, 651, 142
Hopkins P. F., Younger J. D., Hayward C. C., Narayanan D., Hernquist L., 2010, MNRAS, 402, 1693
Hopwood R. et al., 2014, Exp. Astron., 37, 195
Hopwood R. et al., 2015, MNRAS, 449, 2274
Hughes T. M. et al., 2015, A&A, 575, A17
Ibar E., Ivison R. J., Best P. N., Coppin K., Pope A., Smail I., Dunlop J. S., 2010a, MNRAS, 401, L53
Ibar E. et al., 2010b, MNRAS, 409, 38
Ibar E. et al., 2015, MNRAS, 449, 2498
Ikarashi S. et al., 2011, MNRAS, 415, 3081
Iono D. et al., 2006, PASJ, 58, 957
Iono D. et al., 2012, PASJ, 64, L2
Ivison R. J., Harrison A. P., 1996, A&A, 309, 416
Ivison R. J. et al., 2007, MNRAS, 380, 199
Ivison R. J. et al., 2010a, MNRAS, 402, 245
Ivison R. J. et al., 2010b, A&A, 518, L31
Ivison R. J. et al., 2010c, A&A, 518, L35
Ivison R. J., Papadopoulos P. P., Smail I., Greve T. R., Thomson A. P., Xilouris E. M., Chapman S. C., 2011, MNRAS, 412, 1913
Ivison R. J. et al., 2013, ApJ, 772, 137
Ivison R. J. et al., 2016, ApJ, 832, 78
Kennicutt R. C., Evans N. J., 2012, ARA&A, 50, 531
Knapp G. R., Sandell G., Robson E. I., 1993, ApJS, 88, 173
Kormendy J., Ho L. C., 2013, ARA&A, 51, 511
Kovács A. et al., 2010, ApJ, 717, 29
Kroupa P., Weidner C., 2003, ApJ, 598, 1076
Langer W. D., Goldsmith P. F., Pineda J. L., 2016, A&A, 590, A43
Lapham R. C., Young L. M., Crocker A., 2017, ApJ, 840, 51
Liseau R., Justtanont K., Tielens A. G. G. M., 2006, A&A, 446, 561
Lord S. D., Hollenbach D. J., Haas M. R., Rubin R. H., Colgan S. W. J., Erickson E. F., 1996, ApJ, 465, 703
Luhman M. L., Satyapal S., Fischer J., Wolfire M. G., Sturm E., Dudley C. C., Lutz D., Genzel R., 2003, ApJ, 594, 758
Lupu R. E. et al., 2012, ApJ, 757, 135
Lutz D. et al., 2016, A&A, 591, A136
Ma B. et al., 2015, ApJ, 814, 17
Madau P., Dickinson M., 2014, ARA&A, 52, 415
Magdis G. E. et al., 2014, ApJ, 796, 63
Makiwa G., Naylor D. A., Ferlet M., Salji C., Swinyard B., Polehampton E., van der Wiel M. H. D., 2013, Appl. Opt., 52, 3864
Makiwa G., Naylor D. A., van der Wiel M. H. D., Ward-Thompson D., Kirk J. M., Eyres S., Abergel A., Köhler M., 2016, MNRAS, 458, 2150
Malhotra S. et al., 1997, ApJ, 491, L27
Malhotra S. et al., 2001, ApJ, 561, 766
Mangum J. G., Shirley Y. L., 2015, PASP, 127, 266
Matteucci F., ed., 2001, Astrophysics and Space Science Library, Vol. 253, The Chemical Evolution of the Galaxy. Kluwer, Dordrecht
Mennella V., Brucato J. R., Colangeli L., Palumbo P., Rotundi A., Bussoletti E., 1998, ApJ, 496, 1058
Messias H. et al., 2014, A&A, 568, A92
Mocanu L. M. et al., 2013, ApJ, 779, 61
Murphy E. J. et al., 2011, ApJ, 737, 67

Naab T., Johansson P. H., Ostriker J. P., 2009, ApJ, 699, L178
Naylor D. A., Tahic M. K., 2007, J. Opt. Soc. Am. A, 24, 3644
Nayyeri H. et al., 2016, ApJ, 823, 17
Negishi T., Onaka T., Chan K.-W., Roellig T. L., 2001, A&A, 375, 566
Negrello M., Perrotta F., González-Nuevo J., Silva L., de Zotti G., Granato G. L., Baccigalupi C., Danese L., 2007, MNRAS, 377, 1557
Negrello M. et al., 2010, Science, 330, 800
Negrello M. et al., 2014, MNRAS, 440, 1999
Negrello M. et al., 2017, MNRAS, 465, 3558
Neri R., Downes D., Cox P., Walter F., 2014, A&A, 562, A35
Nesvadba N. et al., 2016, A&A, 593, L2
Nieva M.-F., Przybilla N., 2012, A&A, 539, A143
Oberst T. E. et al., 2006, ApJ, 652, L125
Oberst T. E., Parshley S. C., Nikola T., Stacey G. J., Löhr A., Lane A. P., Stark A. A., Kamenetzky J., 2011, ApJ, 739, 100
Oliver S. J. et al., 2012, MNRAS, 424, 1614
Ossenkopf V., Koumpia E., Okada Y., Mookerjea B., van der Tak F. F. S., Simon R., Pütz P., Güsten R., 2015, A&A, 580, A83
Osterbrock D. E., Ferland G. J., 2006, Astrophysics of Gaseous Nebulae and Active Galactic Nuclei. 2nd edn., University Science Books, Sausalito, CA
Oteo I. et al., 2016, ApJ, 827, 34
Oteo I. et al., 2017, ApJ, 850, 170
Ott S., 2010, in Mizumoto Y., Morita K.-I., Ohishi M., eds, ASP Conf. Ser. Vol. 434, Astronomical Data Analysis Software and Systems XIX. Astron. Soc. Pac., San Francisco, p. 139
Papadopoulos P. P., 2010, ApJ, 720, 226
Pavesi R. et al., 2016, ApJ, 832, 151
Peña-Guerrero M. A., Leitherer C., de Mink S., Wofford A., Kewley L., 2017, ApJ, 847, 107
Persson C. M. et al., 2014, A&A, 568, A37
Petuchowski S. J., Bennett C. L., Haas M. R., Erickson E. F., Lord S. D., Rubin R. H., Colgan S. W. J., Hollenbach D. J., 1994, ApJ, 427, L17
Pilbratt G. L. et al., 2010, A&A, 518, L1
Popesso P. et al., 2012, preprint (arXiv:1211.4257)
Rawle T. D. et al., 2014, ApJ, 783, 59
Riechers D. A. et al., 2013, Nature, 496, 329
Riechers D. A. et al., 2014, ApJ, 796, 84
Rigopoulou D. et al., 2013, MNRAS, 434, 2051
Rodríguez-Fernández N. J., Martín-Pintado J., 2005, A&A, 429, 923
Rosenberg M. J. F. et al., 2015, ApJ, 801, 72
Rubin R. H., 1985, ApJS, 57, 349
Sanders R. L. et al., 2016, ApJ, 816, 23
Sargsyan L., Samsonyan A., Lebouteiller V., Weedman D., Barry D., Bernard-Salas J., Houck J., Spoon H., 2014, ApJ, 790, 15
Savage B. D., Sembach K. R., 1996, ARA&A, 34, 279
Scoville N. et al., 2017, ApJ, 836, 66
Serjeant S., 2012, MNRAS, 424, 2429
Simpson J. M. et al., 2014, ApJ, 788, 125
Simpson J. M. et al., 2017, ApJ, 839, 58
Smail I., Ivison R. J., Blain A. W., 1997, ApJ, 490, L5
Smith M. W. L. et al., 2017a, ApJS, 233, 26
Smith J. D. T. et al., 2017b, ApJ, 834, 5
Sparre M. et al., 2015, MNRAS, 447, 3548
Spilker J. S. et al., 2014, ApJ, 785, 149
Spilker J. S. et al., 2016, ApJ, 826, 112
Spinoglio L., Pereira-Santaella M., Dasyra K. M., Calzoletti L., Malkan M. A., Tommasin S., Busquet G., 2015, ApJ, 799, 21
Spoon H. W. W. et al., 2013, ApJ, 775, 127
Stacey G. J., Geis N., Genzel R., Lugten J. B., Poglitsch A., Sternberg A., Townes C. H., 1991, ApJ, 373, 423
Stacey G. J., Hailey-Dunsheath S., Ferkinhoff C., Nikola T., Parshley S. C., Benford D. J., Staguhn J. G., Fiolet N., 2010, ApJ, 724, 957
Stasińska G., Izotov Y., Morisset C., Guseva N., 2015, A&A, 576, A83
Sturm E. et al., 2010, A&A, 518, L36
Sturm E. et al., 2011, ApJ, 733, L16
Swinbank A. M., Chapman S. C., Smail I., Lindner C., Borys C., Blain A. W., Ivison R. J., Lewis G. F., 2006, MNRAS, 371, 465
Swinbank A. M. et al., 2010, Nature, 464, 733
Swinbank A. M. et al., 2011, ApJ, 742, 11
Swinbank A. M. et al., 2012, MNRAS, 427, 1066
Swinbank A. M. et al., 2014, MNRAS, 438, 1267
Swinyard B. M. et al., 2010, A&A, 518, L4
Swinyard B. M. et al., 2014, MNRAS, 440, 3658
Taylor J. H., Cordes J. M., 1993, ApJ, 411, 674
Tielens A. G. G. M., Hollenbach D., 1985, ApJ, 291, 722
Vacca W. D., Garmany C. D., Shull J. M., 1996, ApJ, 460, 914
Valtchanov I. et al., 2011, MNRAS, 415, 3473
Valtchanov I. et al., 2018, MNRAS, 475, 321
Veilleux S. et al., 2013, ApJ, 776, 27
Vieira J. D. et al., 2010, ApJ, 719, 763
Wagg J. et al., 2012, ApJ, 752, L30
Walter F., Riechers D., Cox P., Neri R., Carilli C., Bertoldi F., Weiss A., Maiolino R., 2009a, Nature, 457, 699
Walter F., Weiß A., Riechers D. A., Carilli C. L., Bertoldi F., Cox P., Menten K. M., 2009b, ApJ, 691, L1
Wang R. et al., 2013a, ApJ, 773, 44
Wang S. X. et al., 2013b, ApJ, 778, 179
Wardlow J. L. et al., 2013, ApJ, 762, 59
Wardlow J. L. et al., 2017, ApJ, 837, 12
Wilson D. et al., 2017, ApJ, 848, 30
Wright E. L. et al., 1991, ApJ, 381, 200
Yang C. et al., 2016, A&A, 595, A80
Yang C. et al., 2017, A&A, 608, A144
Yuan F., Buat V., Burgarella D., Ciesla L., Heinis S., Shen S., Shao Z., Hou J., 2015, A&A, 582, A90
Yun M. S. et al., 2015, MNRAS, 454, 3485
Zaritsky D., Kennicutt R. C., Jr, Huchra J. P., 1994, ApJ, 420, 87
Zhang Z.-Y., Romano D., Ivison R. J., Papadopoulos P. P., Matteucci F., 2018, Nature, 558, 260
Zhao Y. et al., 2013, ApJ, 765, L13
Zhao Y. et al., 2016a, ApJ, 819, 69
Zhao Y., Yan L., Tsai C.-W., 2016b, ApJ, 824, 146

APPENDIX A: OBSERVING DATES

Table A1. Basic information of the *Herschel* observations.

Source	Instrument	Time (s)	Date	Proj.	Notes
SDP.9	SPIRE	13 320	2011-11-07	OT1	
	PACS	90	2011-12-02	OT1	
	PACS	90	2011-12-02	OT1	
SDP.11	SPIRE	13 320	2012-11-18	OT1	
	PACS	90	2011-10-18	OT1	
	PACS	90	2011-10-18	OT1	
SDP.17	SPIRE	13 320	2012-11-18	OT2	
	PACS	90	2011-12-02	OT1	
	PACS	90	2011-12-02	OT1	
SDP.81	SPIRE	13 320	2010-06-01	GT1	Valtchanov et al. (2011)
	PACS	90	2010-06-03	GT1	70 and 160 μm maps
	PACS	90	2010-06-03	GT1	70 and 160 μm maps
SDP.130	SPIRE	13 320	2010-06-01	GT1	Valtchanov et al. (2011)
	PACS	90	2010-06-03	GT1	70 and 160 μm maps
	PACS	90	2010-06-03	GT1	70 and 160 μm maps
G09-v1.40	SPIRE	13 320	2011-11-06	OT1	
	PACS	90	2012-04-24	OT1	
	PACS	90	2012-04-24	OT1	
G09-v1.97	SPIRE	13 320	2011-11-08	OT1	
	PACS	90	2011-11-10	OT1	
	PACS	90	2011-11-10	OT1	
G09-v1.124	SPIRE	13 320	2012-11-18	OT2	
	PACS	90	2012-04-13	OT1	
	PACS	90	2012-04-13	OT1	
G09-v1.326	SPIRE	13 320	2011-11-07	OT1	
	PACS	90	2011-11-28	OT1	
	PACS	90	2011-11-28	OT1	
G12-v2.30	SPIRE	13 320	2012-07-07	OT1	
	PACS	90	2011-11-27	OT1	
	PACS	90	2011-11-27	OT1	
G12-v2.43	SPIRE	13 320	2012-07-07	OT1	
	PACS	90	2011-07-14	OT1	
	PACS	90	2011-07-14	OT1	
G12-v2.257	SPIRE	13 320	2012-07-07	OT1	
	PACS	90	2011-07-14	OT1	
	PACS	90	2011-07-14	OT1	
G15-v2.19	SPIRE	13 320	2012-02-04	OT1	
	PACS	90	2011-07-09	OT1	
	PACS	90	2011-07-09	OT1	
G15-v2.235	SPIRE	13 320	2012-02-04	OT1	
	PACS	90	2012-01-12	OT1	
	PACS	90	2012-01-12	OT1	
NA.v1.56	SPIRE	13 320	2012-07-22	OT1	
	PACS	90	2011-11-27	OT1	
	PACS	90	2011-11-27	OT1	
NA.v1.144	SPIRE	13 320	2012-08-03	OT1	
	PACS	90	2011-12-03	OT1	
	PACS	90	2011-12-03	OT1	
NA.v1.177	SPIRE	13 320	2012-08-03	OT1	
	PACS	90	2011-11-27	OT1	
	PACS	90	2011-11-27	OT1	
NA.v1.186	SPIRE	13 320	2012-06-18	OT1	
	PACS	90	2011-07-11	OT1	
	PACS	90	2011-07-11	OT1	
NB43	SPIRE	13 320	2012-08-02	OT1	George et al. (2013)
	PACS	90	2011-11-27	OT1	
	PACS	90	2011-11-27	OT1	
NB.v1.78	SPIRE	13 320	2012-08-02	OT1	
	PACS	90	2011-12-03	OT1	
	PACS	90	2011-12-03	OT1	
NC.v1.143	SPIRE	13 320	2012-07-21	OT1	
	PACS	90	2011-07-11	OT1	
	PACS	90	2011-07-11	OT1	
SA.v1.44	SPIRE	13 320	2012-12-03	OT2	
	PACS	90	2012-11-27	OT2	
	PACS	90	2012-11-27	OT2	

Table A1 *– continued*

Source	Instrument	Time (s)	Date	Proj.	Notes
SA.v1.53	SPIRE	13 320	2012-12-02	OT2	
	PACS	90	2012-11-27	OT2	
	PACS	90	2011-11-27	OT2	
SB.v1.143	SPIRE	13 320	2012-12-29	OT2	
	PACS	90	2012-12-12	OT2	
	PACS	90	2012-12-12	OT2	
SB.v1.202	SPIRE	13 320	2012-12-03	OT2	
	PACS	90	2012-12-12	OT2	
	PACS	90	2012-12-12	OT2	
SC.v1.128	SPIRE	13 320	2012-12-03	OT2	
	PACS	90	2012-12-12	OT2	
	PACS	90	2012-12-12	OT2	
SD.v1.70	SPIRE	13 320	2012-12-28	OT2	
	PACS	90	2012-12-25	OT2	
	PACS	90	2012-12-25	OT2	
SD.v1.133	SPIRE	13 320	2012-12-28	OT2	
	PACS	90	2012-12-11	OT2	
	PACS	90	2012-12-11	OT2	
SD.v1.328	SPIRE	13 320	2012-12-29	OT2	
	PACS	90	2012-12-11	OT2	
	PACS	90	2012-12-11	OT2	
SE.v1.165	SPIRE	13 320	2012-12-29	OT2	
	PACS	90	2012-12-25	OT2	
	PACS	90	2012-12-25	OT2	
SF.v1.88	SPIRE	13 320	2012-07-08	OT2	
	PACS	90	2012-07-15	OT2	
	PACS	90	2012-07-15	OT2	
SF.v1.100	SPIRE	13 320	2012-07-08	OT2	
	PACS	90	2012-07-15	OT2	
	PACS	90	2012-07-15	OT2	
SG.v1.77	SPIRE	13 320	2012-07-17	OT2	
	PACS	90	2012-06-25	OT2	
	PACS	90	2012-06-25	OT2	
HeLMS05	PACS	90	2013-01-06	OT2	
	PACS	90	2013-01-06	OT2	
HeLMS06	PACS	90	2013-01-06	OT2	
	PACS	90	2013-01-06	OT2	
HeLMS09	PACS	90	2013-01-11	OT2	
	PACS	90	2013-01-11	OT2	
HeLMS44	SPIRE	13 320	2013-01-08	OT2	
	PACS	90	2013-01-01	OT2	
	PACS	90	2013-01-01	OT2	
HeLMS45	SPIRE	13 320	2012-12-29	OT2	
	PACS	90	2013-01-01	OT2	
	PACS	90	2013-01-01	OT2	
HeLMS49	PACS	90	2013-01-06	OT2	
	PACS	90	2013-01-06	OT2	
HeLMS51	PACS	90	2013-01-06	OT2	
	PACS	90	2013-01-06	OT2	
HeLMS61	PACS	90	2013-01-01	OT2	
	PACS	90	2013-01-01	OT2	
HeLMS62	PACS	90	2012-12-26	OT2	
	PACS	90	2012-12-26	OT2	
HBoötes03	SPIRE	13 320	2012-02-05	OT1	
	PACS	90	2011-11-27	OT1	
	PACS	90	2011-11-27	OT1	
HXMM02	SPIRE	13 320	2012-02-05	OT1	
	PACS	90	2012-02-14	OT1	
	PACS	90	2012-02-14	OT1	
Eyelash	SPIRE	13 320	2011-04-24	OT1	George et al. (2014)
	SPIRE	13 320	2012-11-17	OT2	As above
	SPIRE	13 320	2012-11-24	OT2	As above
	SPIRE	13 320	2012-11-24	OT2	As above
	SPIRE	13 320	2012-12-01	OT2	As above
	SPIRE	13 320	2012-12-02	OT2	As above
	PACS	90	2011-11-17	OT1	
	PACS	90	2011-11-17	OT1	

Herschel observations of the sample of strongly lensed DSFGs. SPIRE spectrometer observations consist of 100 forward and 100 reverse scans of the SMEC mirror. The two PACS photometer observations of each source consist of 10 × 3 arcmin scan legs oriented at 70° and 110°, respectively, and combined during processing into a single mini scan map.

APPENDIX B: PACS IMAGING

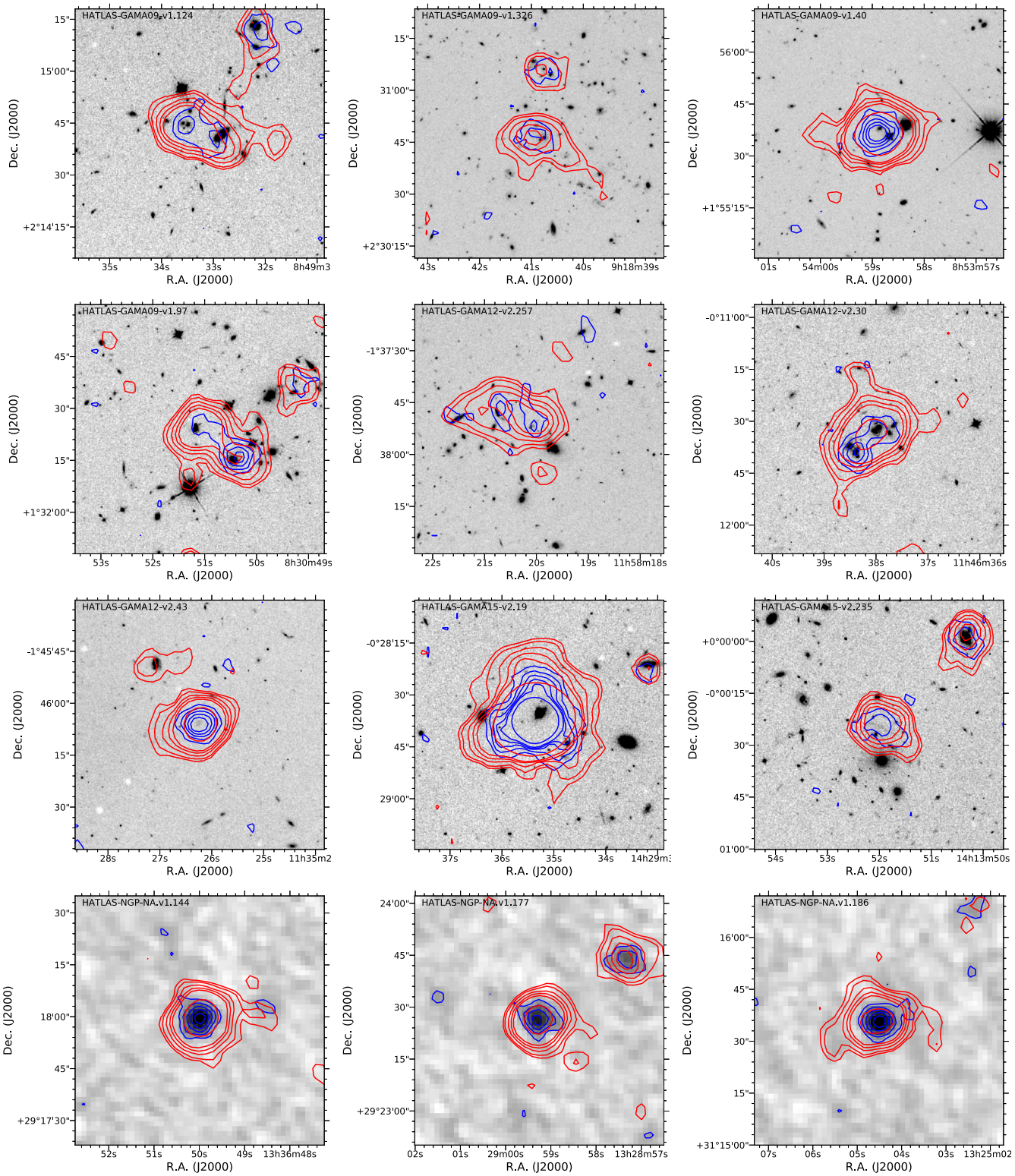

Figure B1. *Herschel* PACS images of the sample. The high-resolution background images are *HST F*110*W* archival data. The low-resolution background images are PACS 100 μm data. Red contours are PACS 160 μm data, with levels of 0.3,0.4, 0.6, 0.8, 1, and 2 mJy pixel^{-1}. Blue contours are PACS 100 μm data, with levels of 0.2, 0.4, 0.6, 0.8, 1, and 2 mJy pixel^{-1}.

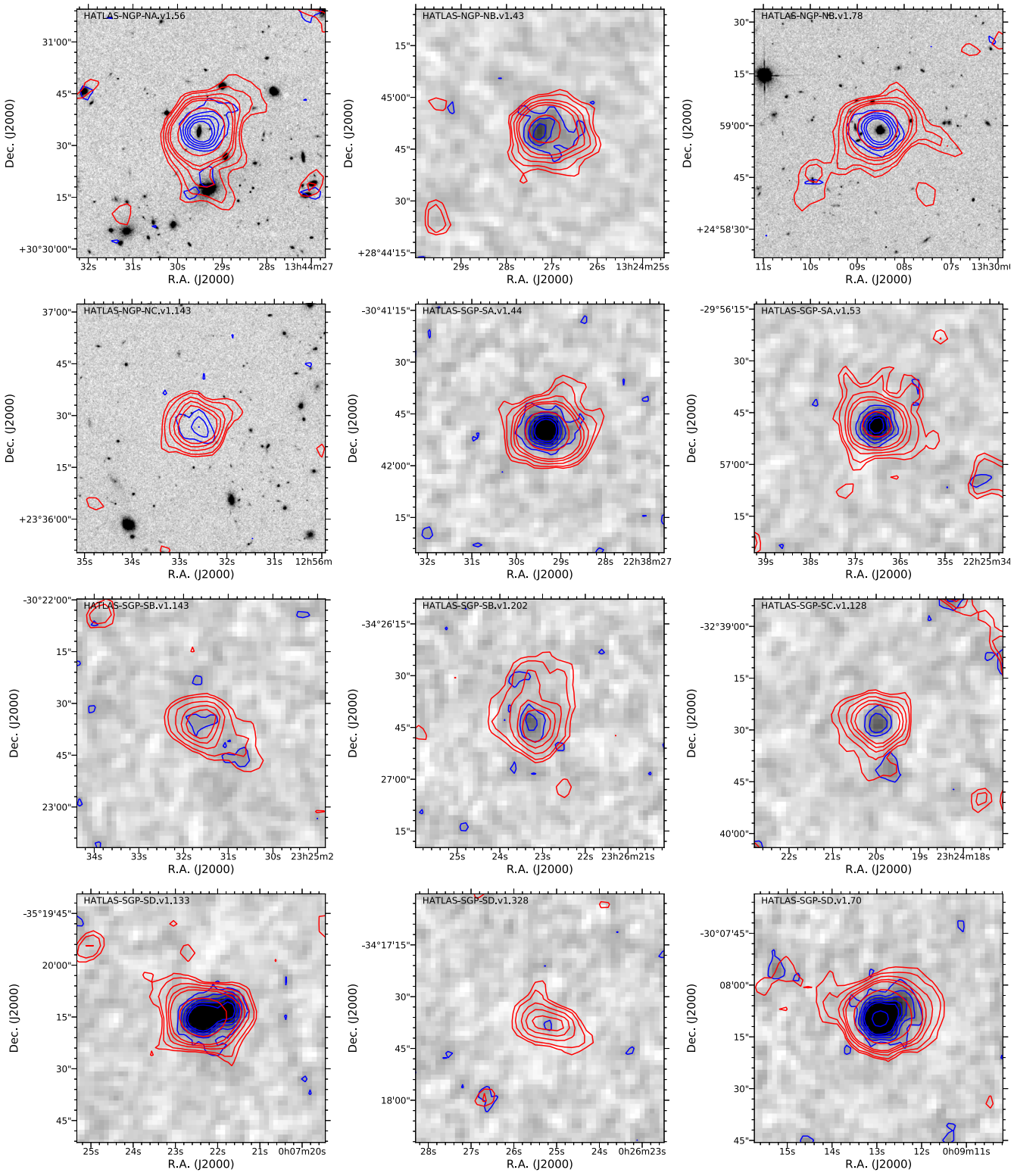

Figure B1. *–continued.*

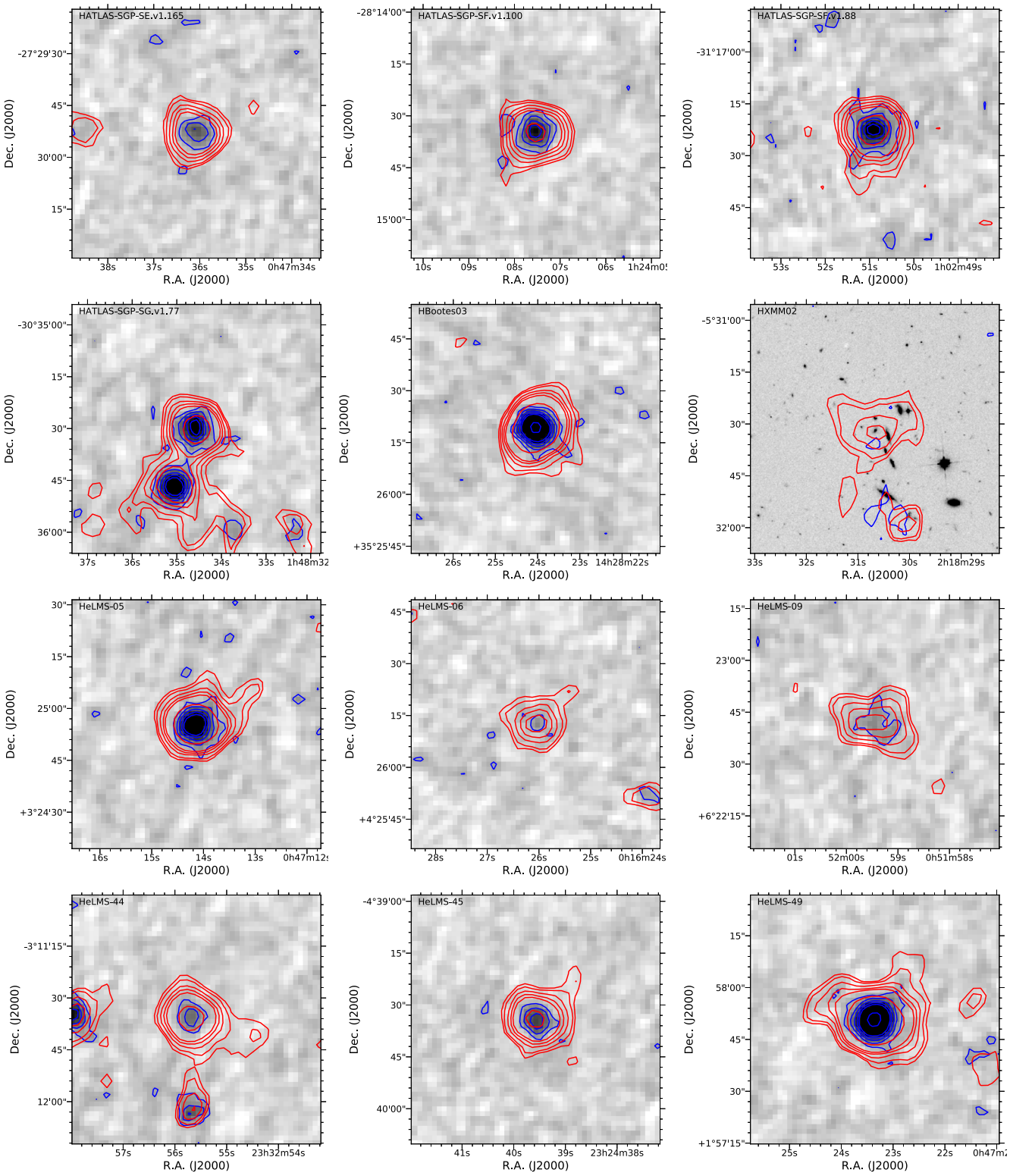

Figure B1. *–continued.*

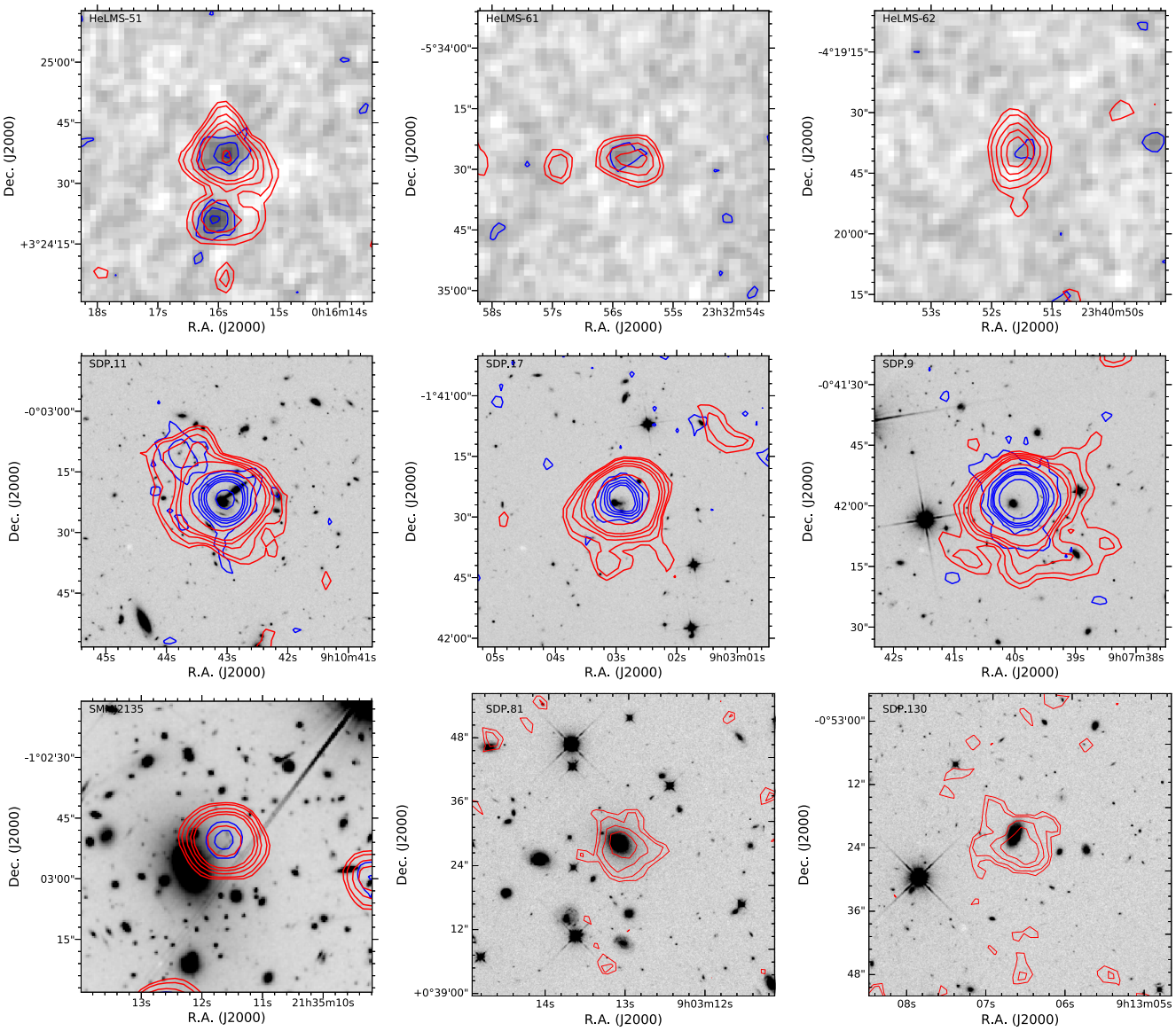

Figure B1. *–continued.*

APPENDIX C: BASELINE SUBTRACTION AND SIGNAL RECOVERY

In this section, we compare different background subtraction methods in the data reduction of *Herschel* SPIRE/FTS data. To remove the overall baseline profile, and especially the low-frequency ripple features produced by the imperfect calibration, we perform a convolved baseline fitting. To do so we first mask the frequency ranges of a few strong lines ([C II] ,, [O III] 88 μm, OH), each with a 2 GHz width, to avoid contaminations from the lines. Then we convolve the masked spectra with a Gaussian profile with 15 GHz (FWHM), which ensures a local baseline feature but without fitting the relatively narrower line features. We then subtract the baseline profiles from the original spectra to get the final output spectra for each target.

Fig. C1 presents an example of the baseline subtraction method. The thin lines show the pipeline produced spectra in the two central pixels of the *Herschel* FTS, SLW03 and SSW04. Thick lines show the baselines produced by convolving the masked spectra (the line free part) and Gaussian profile with 15 GHz in FWMH. The blue shadowed regions show the frequency ranges of the masked line features, which may potentially bias the baseline fitting. The red line shows an artificial Sinc function response with a peak of 0.3 Jy and an FWHM width of 1.2 GHz convolved with a 500 km s^{-1} Gaussian FWHM.

To fully verify the robustness of this method, we make a sanity test by randomly insetting artificial spectral signals to the raw data, subtract the baseline, and test if we can recover the line flux. We perform the test by randomly insert artificial signals in the spectra. We find that, if the signal is higher than 0.5 Jy (peak) and if the line width is less than 2000 km s^{-1}, the line flux can be recovered on very high confidential with an average error level of less than 20 per cent of the real fluxes. Fig. C2 presents a histogram of measured fluxes for 10 000 times random test. The distribution shows a very well centralized flux corresponding to the inserted artificial noise, with relatively small span. This indicates

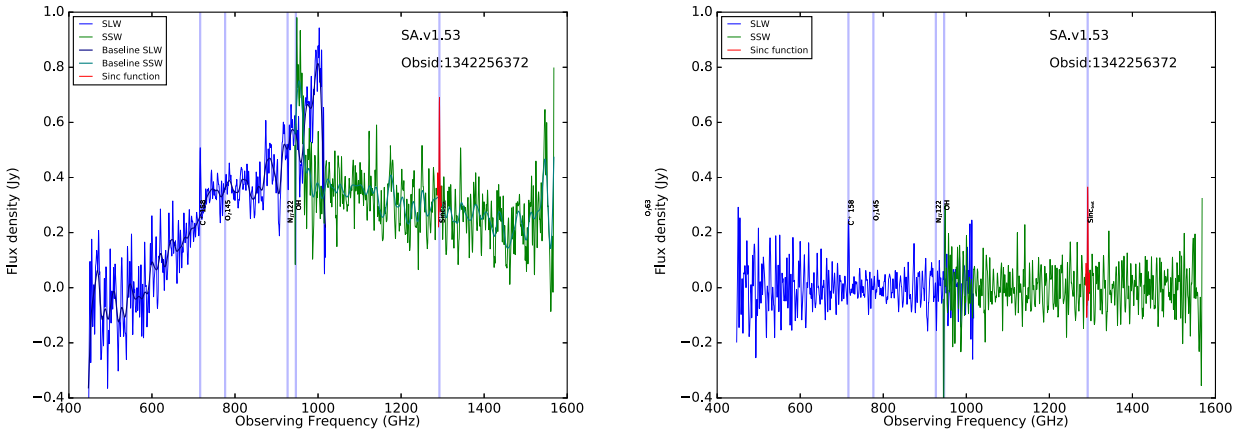

Figure C1. An example of our baseline subtraction method. *Left*: The observed *Herschel* FTS spectra of SA.v1.53, after standard calibrations. The thin blue line shows the spectrum obtained in the SLW03 receiver, and the thin green line shows the spectrum obtained in the SSW04 receiver. The thick lines show the baselines fitted using a 15 GHz Gaussian width, after masking the frequency ranges of potential line features. The blue shadowed regions show the masked frequency ranges potentially dominated by line emission or absorption features. Red line shows an artificial Sinc function response, which has a peak flux density of 0.3 Jy, an FWHM width of 1.2 GHz, and is further convolved with a Gaussian profile with a 500 km s^{-1} FWHM. *Right*: The FTS spectra after baseline subtraction. The line features (the [C II] line and the testing Sinc function) are still robust.

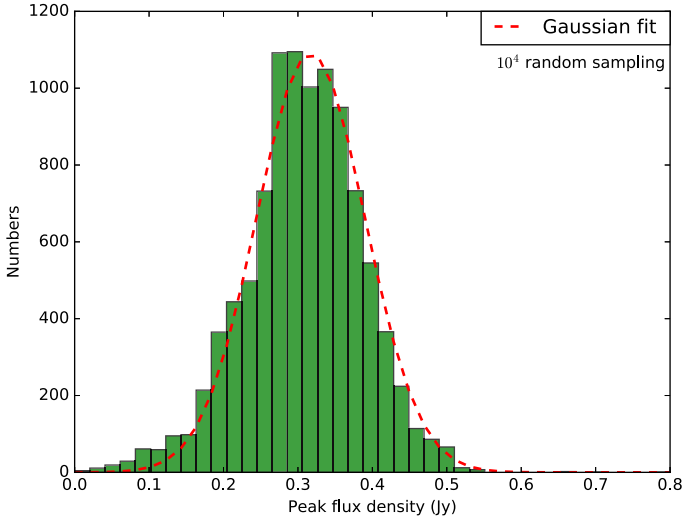

Figure C2. Distribution of the measured line fluxes, for a 10 000 times randomly sampled signal of 0.3 Jy Sinc function after baseline subtraction.

that the baseline subtraction method does not alter the general flux measurement, and the ripple baseline feature likely not influence much on the high-frequency (in Fourier domain) scales.

We fit a Gaussian to the histogram distribution, and find the σ to be $\sim$0.05 Jy. However, we also find that the distribution does not follow a Gaussian profile very well, especially for both the high and the low ends. We also examine how much does the recovered flux distribution deviate from normal distribution, and find that both K–S test and P-test gives $\sim 10^{-8}$, which mean that the histogram is not well following a normal distribution. This is likely because the noise is not uniform across the whole spectral range that may bias the noise distribution. Another reason could be that the noise between channels is correlated, and is not a white noise. It seems that the noise of the spectra is spiky that enlarges the histogram distribution at both ends with some extreme values. Overall, the test indicates a robust flux measurement can be recovered after the baseline subtraction.

APPENDIX D: SPIRE FTS SPECTRA OF ALL TARGETS

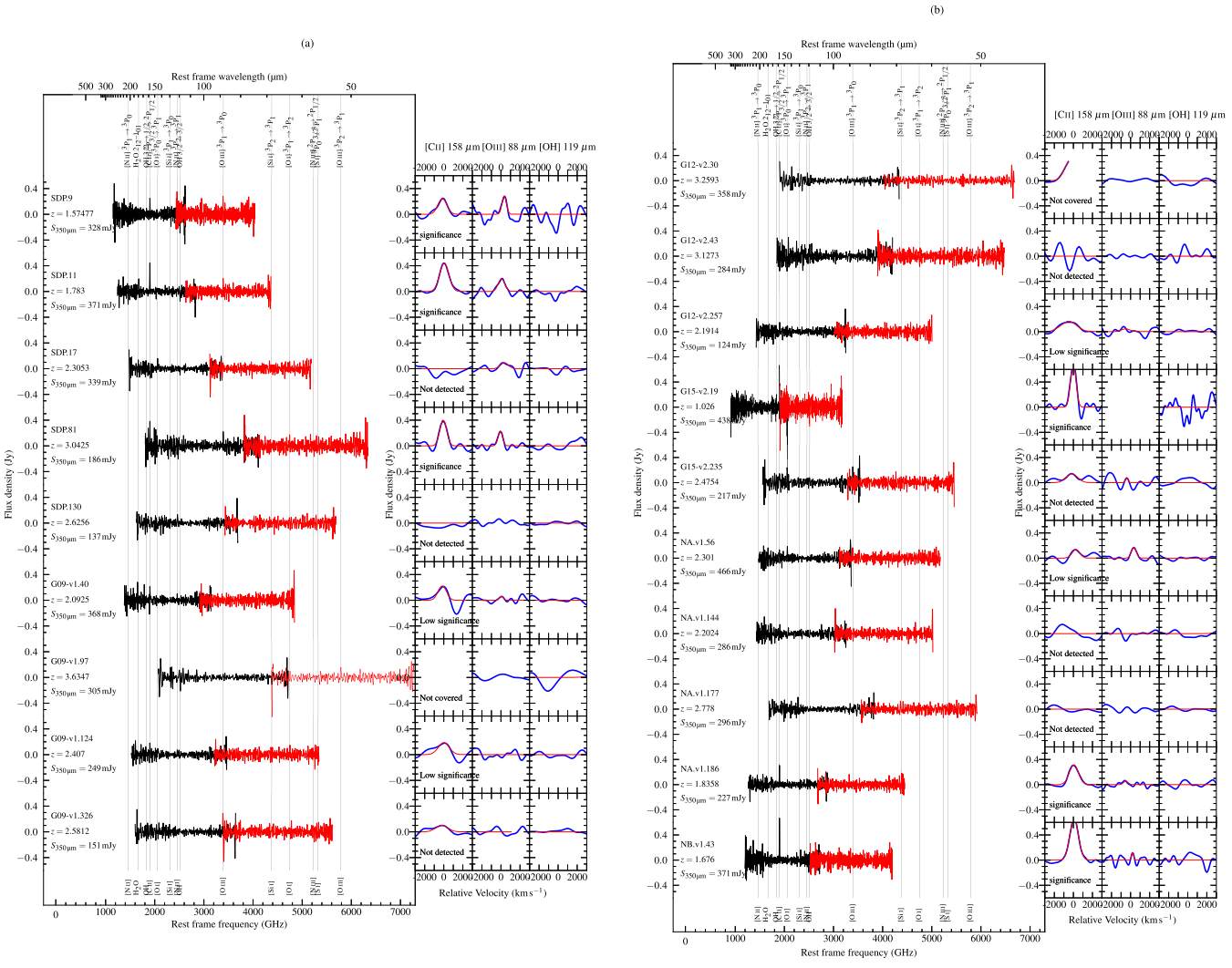

Figure D1. Spectra obtained using *Herschel* SPIRE/FTS, after subtracting the baselines.

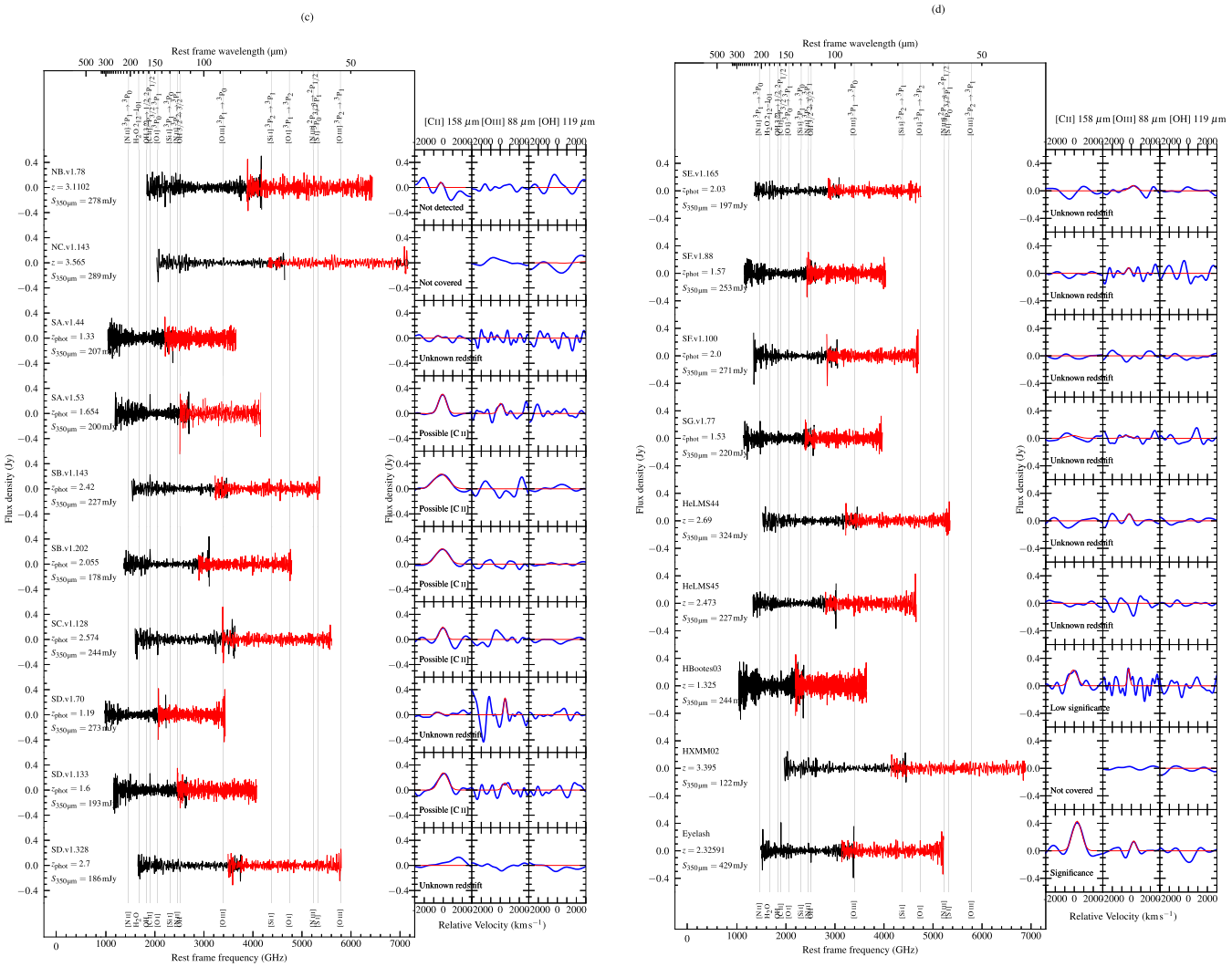

Figure D1. *–continued.*

APPENDIX E: COMMENTS ON INDIVIDUAL OBJECTS

SDP.9 (J090740.0−004200): This is the lowest redshift and brightest of the original five strongly lensed DSFGs found in *H*-ATLAS (Negrello et al. 2010). NIR imaging suggests a nearly complete Einstein ring (Negrello et al. 2014), however the dust emission is dominated by the SE region (Bussmann et al. 2013). Despite calculating almost identical dust emission luminosities, the SFR we derive using our chosen calibration: that presented in Murphy et al. (2011) and recommended by the review of Kennicutt & Evans (2012); is a factor of 3 higher than value reported by Negrello et al. (2014). We find a relatively low $L_{[\mathrm{C\,II}]\,158\,\mu\mathrm{m}}$-to-$L_{\mathrm{FIR}}$ ratio of $2.5 \pm 0.9 \times 10^{-4}$.

SDP.11 (J091043.0−000322): NIR imaging shows this object as a full yet elongated Einstein ring. Dust emission does not exhibit the same brightness distribution, with the northern and southern regions dominant. A $7.5 \pm 2.3 \times 10^{-18}$ W m^{-2} [O I] 63 μm line has been observed with PACS (Verma et al. in preparation). We find the [C II] 158 μm line to have a flux $9.7 \pm 0.9 \times 10^{-18}$ W m^{-2}. Fifty per cent higher than a recent measurement from ZEUS-2 on APEX (Ferkinhoff et al. 2014).

SDP.17 (J090302.9−014127): With a complex NIR light profile, this system is difficult to separate into clear foreground and background components. The lensed image is not resolved into multiple components by the SMA in even the most extended configuration, suggesting a relatively low amplification factor and hence high intrinsic luminosity. Despite this, the large emission area suggested by Bussmann et al. (2013) would indicate a comparatively modest SFR surface density, making our [C II] 158 μm non-detection interesting should that parameter be a key driver of the line-to-FIR continuum deficit.

SDP.81 (J090311.6+003906): This galaxy is lensed into two arcs, exquisitely revealed by recent long-baseline ALMA imaging (ALMA Partnership et al. 2015). These data have been used to produce a detailed reconstruction of the source-plane emission (Dye et al. 2015), which exhibits 200 pc-scale clumps. We use the amplification derived for the dust emission from this modelling effort: 15.9 ± 0.7: which is higher than an estimate from lower resolution SMA data (11.1 ± 1.1; Bussmann et al. 2013), and also higher than the amplification estimated for the optical emission: 10.2 ± 0.5; which appears not to be co-spatial with the rest-frame FIR emission (Dye et al. 2015), as is common for starbursts (e.g. the Antennae Galaxies). An estimate of the source-plane emission radius from those data: 0.5 ± 0.2 kpc; is also used in our SED fitting. The SPIRE FTS spectrum is presented in Valtchanov et al. (2011) (programme GT1_IVALTCHA_1), but for consistency

we reprocess the data here. Due to the different method of background subtraction (off-axis versus dark sky) we find a substantially lower [CII] 158 μm flux. However, as the off-axis method produced reduced noise over the data set as a whole, and is used in the reduction of SPIRE spectra of other similarly faint targets (e.g. Magdis et al. 2014; Gullberg et al. 2015), we use our measurement throughout this work. Despite the lower line flux, this object still appears to possess the highest $\mu L_{[\mathrm{C\,II}]\,158\,\mu\mathrm{m}}$ and $L_{[\mathrm{C\,II}]\,158\,\mu\mathrm{m}}/L_{\mathrm{FIR}}$ values of our sample.

SDP.130 (J091305.0−005343): With a modest ∼2 × amplification this galaxy has significantly lower flux densities than the target threshold, and Valtchanov et al. (2011) found no lines in the FTS spectrum. Using newer calibration data, we find possible H II region emission, however the non-detection of [C II] 158 μm indicates these are likely noise.

G09-v1.40 (J085358.9+015537): This galaxy is visible in K_s band imaging as an almost-complete Einstein ring, consequently experiencing a high magnification factor of ∼15. The source-plane object may be highly elongated (Calanog et al. 2014). We detect [C II] 158 μm.

G09-v1.97 (J083051.0+013224): This source is lensed by two foreground galaxies at different redshift. While it possesses one of the largest μL_{IR} values of the sample, the high redshift means [C II] 158 μm is not covered by the FTS.

G09-v1.124 (J084933.4+021443): Uniquely within our sample this object is known to be essentially unlensed, its broad CO lines suggesting a very high intrinsic luminosity, confirmed by a range of follow-up observations which showed a system of four separate DSFGs, two of which are individually over the HyLIRG limit (Ivison et al. 2013). These two brightest are detected as separate point sources in our PACS imaging, but together only provide a low significance [C II] 158μm feature. Recent NIR spectroscopy has revealed a broad-line AGN in this system (Oteo et al. in preparation), which will be responsible for some fraction of its FIR flux.

G09-v1.326 (J091840.8+023047): Available SMA imaging is consistent with a point source and no counterpart is found in *HST* or Keck imaging. Should this be an unlensed DSFG it would possess an SFR of $\sim$5000 $\mathrm{M_\odot\,yr^{-1}}$, higher than any component of the known HyLIRG G09-v1.124, so we instead assume the amplification estimate of 5 ± 1 from Harris et al. (2012) derived from its CO luminosity and FWHM. No FIR cooling lines are observed in the FTS spectrum, however the flux densities lie below the target threshold.

G12-v2.30 (J114638.0−001132): A detailed study of this galaxy is presented in Fu et al. (2012), indicating a complex system in which the existing stellar population is quadruply lensed by a net factor of over 2× that of the offset starburst, which provides some of the highest 500 and 880μm flux densities in our sample. This redshift represents the limit of the FTS coverage of the [C II] 158 μm line, which therefore lies in the noisiest region of the spectrum and is not detected.

G12-v2.43 (J113526.3−014606): Multiple lensed images are not resolved in the 880μm SMA data, however a faint source visible in *HST* *F*110*W* and Keck/NIRC2 K_s imaging is likely a foreground lensing galaxy. With an apparent $\mu L_{\mathrm{IR}} > 10^{14.1}\,\mathrm{L_\odot}$, among the highest of our sources, we assume the large amplification estimate of Harris et al. (2012): 17 ± 11. As with G12-v2.30, the [C II] 158 μm line lies within the high-noise end region of the spectrum, and no FIR lines are observed.

G12-v2.257 (J115820.1−013753): Two nearby spiral galaxies visible at 100μm will be unresolved within the SPIRE beam but likely contribute very little to the measured flux densities at the longer wavelengths. No lensing model is available, though this object has one of the lowest 350 μm flux densities within our sample indicating a low μL_{IR} and likely $\mu \lesssim 5$. We however take the published amplification estimate of 13 ± 7 from Harris et al. (2012). As with the other low flux density sources, we do not find any emission line features.

G15-v2.19 (J142935.3−002836): This object is the brightest (and lowest redshift) within our sample. A detailed study is presented in Messias et al. (2014) indicating a gas-rich (25 per cent of baryonic mass) merger of two source-plane components lensed into an almost-complete Einstein ring. The redshift is too low for the spectrum to cover [OI] 63 μm and [O III] 88 μm, but a strong [C II] 158 μm feature is found. Additionally, we detect 119 μm OH $^2\Pi_{3/2}$ J = $\frac{3}{2} \rightarrow \frac{5}{2}$ absorption.

With no strong evidence of an AGN (Messias et al. 2014) we, as with a similar detection within SMM J2135 (George et al. 2014), attribute this to an SNe-driven outflow of molecular gas.

G15-v2.235 (J141351.9−000026): This galaxy is weakly lensed by a cluster with only a single elongated image visible, suggesting a high intrinsic luminosity. We find [CII] 158 μm and the second highest $L_{[\mathrm{C\,II}]\,158\text{-}\mu\mathrm{m}}/L_{\mathrm{FIR}}$ ratio of the sample.

NA.v1.56 (J134429.4+303036): This source has the highest 350 and 500 μm flux densities in our sample, visible as two well-defined arcs in SMA imaging. We detect [C II] 158 μm emission.

NA.v1.144 (J133649.9+291801): Available optical–NIR imaging is insufficiently deep to detect a lensing galaxy, however the 880 μm morphology indicates that this object is likely lensed with a small Einstein radius. A second tentative source at $z = 2.3078$ was suggested by a blind CO line search (Harris et al. 2012). We do not detect any spectral lines.

NA.v1.177 (J132859.3+292317): This source is resolved into a single elongated image in SMA data, and likely also responsible for a faint arc in Keck/NIRC2 K_s imaging. No lens models has been produced so far, and we do not detect any lines.

NA.v1.186 (J132504.4+311537): A feature suggestive of [C II] 158 μm at $z = 1.836$ found in our FTS spectrum was followed up with CARMA, extending the 3 mm spectrum below the nominal 85 GHz tuning range to detect CO J = 2 → 1. A redshift of 1.8358 was confirmed, negating the previous estimate of $z = 2.635$. With no published deep NIR or interferometric FIR–mm imaging, a lens model has not been produced.

NB.v1.43 (J132427.0+284452): NIR images of this galaxy display an ≈10 arcsec long arc with little curvature: much more spatially extended than is visible in submillimetre data which arises from a small area towards the centre. Our FTS spectrum along with its detection of strong [CII] 158 μm emission was presented in George et al. (2013), however since publication of those data, a lensing model has been published. Lensing bodies are likely either two galaxies or a nearby cluster (see Bussmann et al. 2013, for a discussion), with a (relatively uncertain) lensing amplification factor of 2.8 ± 0.4 derived for the dust emission. Calculations in this work utilize that value.

NB.v1.78 (J133008.4+245900): With > 200 mJy flux densities in all SPIRE bands, and at 160 μm despite a redshift above 3, this galaxy has the highest μL_{IR} of the sample and a warm dust temperature caused by its small radius and hence high SFR surface density. Coupled with the position of the [C II] 158 μm line within the spectrum, our non-detection of that transition is therefore perhaps unsurprising.

NC.v1.143 (J125632.7+233625): The lens has a redshift low enough for it to be visible in SDSS imaging and similarly to NB.v1.78, the background galaxy has a high μL_{IR} and an even higher dust temperature and SFR surface density, however the high redshift of this source means that [C II] 158 μm is not covered by the FTS spectrum.

H-ATLAS SGP sources: Without definite redshifts, it is difficult to glean much from these sources. Several have low significance SPIRE spectral features potentially corresponding to [C II] 158 μm, with the corresponding redshift listed in Table 2.

HeLMS sources: Only two of these galaxies were observed with the FTS, none of them exhibits [C II] 158 μm emission. Further follow-up of these objects needs to be done, rendering any conclusive determinations of their properties or lensing amplification difficult.

HBoötes03 (J142824.0+352619): This is a well-studied high-redshift DSFG (also known as MIPS J142824.0+352619) discovered before the wide area *Herschel* and SPT surveys (Borys et al. 2006; Swinbank et al. 2006). *Herschel* PACS detections of [O III] 52 μm ($3.7 \pm 0.8 \times 10^{-18}$ W m^{-2}) and [O I] 63 μm ($7.8 \pm 1.9 \times 10^{-18}$ W m^{-2}) are presented in Sturm et al. (2010), and a $19.8 \pm 3.0 \times 10^{-18}$ W m^{-2} [C II] 158 μm detection with CSO/ZEUS in Hailey-Dunsheath et al. (2010). This latter value is particularly significant, being a factor of 5 higher than our measurement. We are unsure as to the reason for the magnitude of this discrepancy.

HXMM02 (J021830.5−053124): This object (also known as Orochi or SXDF1100.001) was included due to its previous in-depth study (Ikarashi et al. 2011; Iono et al. 2012). The small lens Einstein radius and amplification however give it the lowest 250 and 350 μm flux densities in our sample, which when coupled with its high redshift (such that the FTS spectrum does not cover [C II] 158 μm), mean no FIR lines are found. The dust mass temperature index of 7.2, used to fit all other galaxies is insufficient to account for the high PACS flux densities, with the best-fitting value being 5.7. This suggested additional mass of hot dust, coupled with the low FIRRC value (assuming a synchrotron spectral index of −0.75) indicates the presence of an AGN.

SMM J2135 (J213511.6−010252): The Cosmic Eyelash is one of the most well-studied high-redshift DSFGs, its 37.5 ± 4.5 amplification factor enabling the spatial and spectral resolution of 3–4 massive star-forming clumps (e.g. Ivison et al. 2010c; Swinbank et al. 2010, 2011; Danielson et al. 2013). After a tentative detection of OH 119 μm absorption in the OT1 observation of this source, we included five repeat observations of that object in OT2. A detailed examination of that data is presented in George et al. (2014), however for consistency we reprocess that data again here. [C II] 158 μm appears at a higher velocity in the original spectrum than the repeats, however while individual spectra may exhibit slight noise-related velocity differences, the fit to the combined spectrum of all SMM J2135 observations should be more reliable.

This paper has been typeset from a TEX/LATEX file prepared by the author.